Montanuniversität Leoben – University of Leoben
Department Metallurgie – Department of Metallurgy
Nichteisenmetallurgie – Nonferrous Metallurgy

Recycling of refractory metals

A dissertation by

Karin Ratschbacher

Leoben, August 2015

Nichts ist gelber als Gelb selber.

AFFIDAVIT

I declare in lieu of oath, that I wrote this thesis and performed the associated research myself, using only literature cited in this volume.

September 18, 2015, Karin Ratschbacher

Acknowledgements

I would like to thank Priv.-Doz. Luidold Stefan for offering his support and insights throughout this thesis.
At Plansee SE I would like to thank Huber Karl and Kuisle Mario for initiating this project, their motivation for pushing it further and the comfortable collaboration.

Last but definitely not least I would like to thank my friends and family for their undivided support and encouragement.

Abstract

Recycled materials and scrap represent, especially in the case of critical raw materials, a valuable resource to secure supply and provide the processing companies with a higher degree of independence from fluctuations in prices and delivery bottlenecks. The target of this thesis is the replacement of the current practice of selling and down-cycling valuable refractory metal scrap by laying the groundwork for an on-site recycling process which enables the company to leave assets within company property.

To get insights into the conversion-behavior of various refractory-metal alloys under an oxidizing atmosphere over time, kinetic experiments were conducted on a Mo-Ta- as well as a W-Re alloy, which lead to deduction of the corresponding reaction rates.

Pilot experiments enabled the investigation on how well and under which conditions the alloys Mo-Ta, W-Re, Mo-Cu, Mo-W, Mo-Nb and Mo-Ti can be separated into their components through oxidation and sublimation of one of the alloying element's oxide. Very pure products resulted from Mo-Ta, W-Re and Mo-Nb alloys, which were converted in a tube furnace. Furthermore a vacuum technology based approach for the separation of a Mo-Cu alloy into its components is introduced.

A statistical design of experiment lead to empirical equations which estimate the influence of the most important process parameters for the conversion of the Mo-Ta alloy, which are temperature, grain size and oxygen content of the process atmosphere on the conversion time and the purity of the product. This offers the opportunity to optimize process parameters in order to achieve minimal conversion time with the highest possible degree of conversion feasible under set conditions. This data was used to determine the process parameters for the transformation of the Mo-Ta chips in a laboratory size rotary kiln, investigating the influence of the movement on the conversion behavior. Process parameters were further adjusted for converting Mo-Ta, W-Re and Mo-Ti chips as well as agglomerated Mo-W abrasive slurry in the kiln.

The experiments conducted on an industrial size rotary kiln represent the last scale up. Stable conditions and high purity products as well as an output, which could make this process economically rewarding were achieved.

Kurzfassung

Die Wiederaufbereitung von Materialien und Schrotten, insbesondere im Fall von kritischen Rohstoffen, stellt eine wertvolle Quelle zur Sicherung der Versorgung dar und bietet weiters eine hervorragende Möglichkeit für verarbeitende Betriebe weitgehend unabhängig von Preisschwankungen am internationalen Rohstoffmarkt und Versorgungsengpässen zu operieren. Die vorliegende Arbeit setzt sich zum Ziel, eine Grundlage dafür zu schaffen, die gängige Praxis des Verkaufens und Downcyclens von Refraktärmetallschrott durch einen Recyclingprozess am Standort zu ersetzen, wodurch das Unternehmen die Wertfraktion Schrott im Firmenbesitz halten kann.

Das Oxidations- und Sublimationsverhalten einer Mo-Ta- und einer W-Re-Legierung wurde anhand kinetischer Experimente charakterisiert und die zugehörigen Geschwindigkeitsgesetze bestimmt. Der Einfluss verschiedener Prozessbedingungen auf die Trennbarkeit von Mo-Ta-, W-Re-, Mo-Cu-, Mo-W-, Mo-Nb- und Mo-Ti-Legierungen durch Oxidation und Sublimation des Oxids von einem der Legierungselemente wurde durch erste Tastversuche bestimmt. Dabei konnten Produkte von hohem Reinheitsgrad beim Umsetzen von Mo-Ta-, Mo-Nb- und W-Re-Legierungen erzielt werden. Zusätzlich wird eine auf Vakuumtechnologie basierende Trennmethode für Mo-Cu-Verbunde vorgestellt.

Durch die statistische Auswertung eines Versuchsplanes konnte eine empirische Formel zur Abschätzung des Einflusses der wichtigsten Prozessparameter (Temperatur, Sauerstoffgehalt im Prozessgas und Korngröße des Einsatzmaterial) auf die Oxidationszeit und die Reinheit der entstehenden Produkte abgeleitet werden. Dadurch lassen sich die Prozessparameter hinsichtlich niedriger Oxidationszeit bei gleichzeitig höchstmöglicher Reinheit der Produkte optimieren. Dies wurde bereits bei der Festlegung der Prozessbedingungen für die Oxidation von Mo-Ta-Spänen in einem Labordrehrohrofen, zur Untersuchung des Einflusses der bewegten Schüttung auf das Oxidations- und Sublimationsverhalten, genutzt. Durch kontinuierliche Anpassung der Prozessparameter waren Mo-Ta-, W-Re- und Mo-Ti-Späne wie auch agglomerierter Mo-W-hältiger Schleifschlamm im Labordrehrohrofen umsetzbar.

Den letzten "'upscaling"'-Schritt stellen Versuche in einem Drehrohr im Industriemaßstab dar. Dabei konnte ein stabiler Prozess mit hoher Produktreinheit und einem Materialumsatz, der einen wirtschaftlichen Recyclingprocess möglich macht, betrieben werden.

Contents

1 Introduction

This thesis deals with refractory metals, mainly molybdenum and alloys thereof. Some of the metals investigated in this work are classified as critical by the European Union concerning supply risk and economic importance (figure 1.1). In order to preserve resources and decrease the dependency on imports a process to separate and recycle refractory-metal alloys on company premisses, without having to sell or downcycle scrap, should be developed. Europe's vast dependency on imports in the case of molybdenum is displayed in figure 1.2.

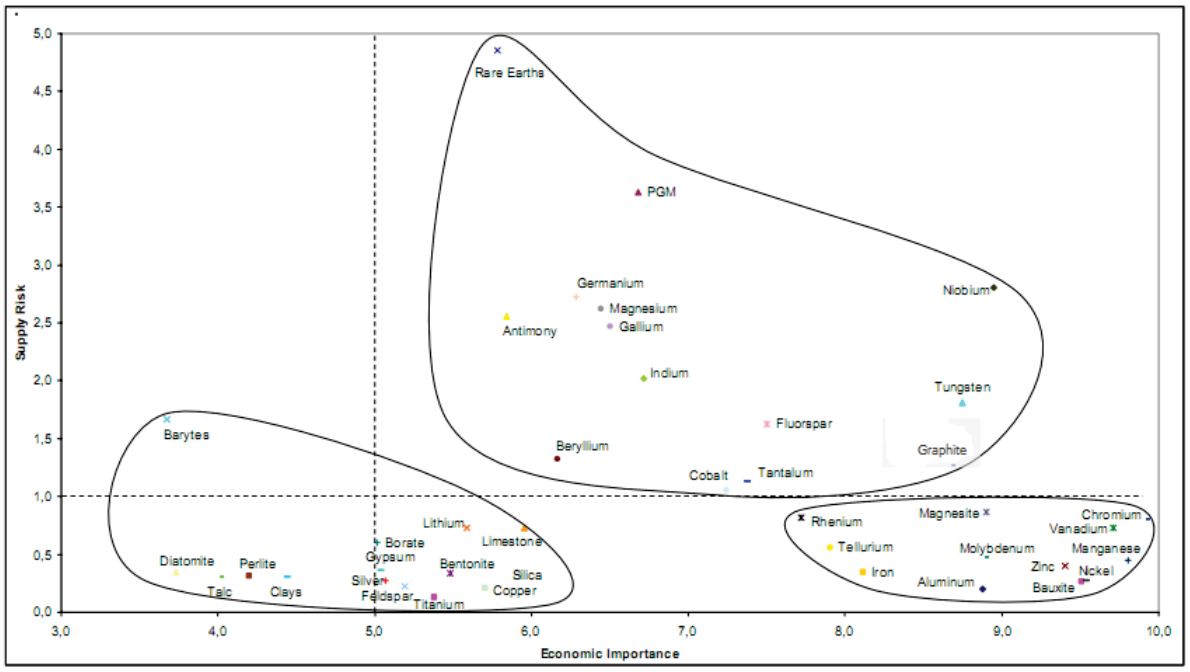

Figure 1.1: Critical metals defined by the EU [1]

The worldwide production of molybdenum constantly increases as displayed in table 1.1.
The main exporting states are in south America, the middle east and the United States of America [2]. Internationally the main trading products are ferromolybdenum, molybdenumoxide, concentrated ores, scrap and molybdenum-powder and -blooms.

Table 1.1: Worldwide production of molybdenum [1–5]

Land	2004	2005	2006	2007	2008	2009 [2]	2010 [1,2]	2011 [2,3]	2012 [2]	2013 [2]
Armenia	2,980	3,030	4,090	4,385	4,472	4,365	4,335	4,817	6,500	6,700
Russia	4,800	4,800	4,800	4,800	4,800	4,562	4,495	4,843	4,800	4,800
Canada	9,519	7,935	7,723	6,819	9,332	8,721	8,648	8,674	9,063	7,618
Mexico	3,731	4,245	2,519	6,491	7,812	10,166	10,849	10,787	11,366	12,100
USA	41,500	58,000	59,800	57,000	61,400	47,800	57,400	63,700	61,500	60,700
Argentinia	-	-	-	-	228	-	-	-	-	-
Chile	41,883	47,885	43,158	66,775	33,639	34,925	37,186	40,889	35,090	38,715
Peru	14,246	17,325	17,209	16,787	16,721	12,297	16,963	19,141	16,790	18,140
China	38,430	30,000	43,900	67,700	81,000	93,500	96,600	103,000	105,000	101,000
Iran	1890	2476	3574	8933	2500	3900	3400	3900	4000	
Kasachstan		400	800	800	-	-	-	-	-	
Kirgistan	250	250	250	250	250	n,a	n,a	n,a	n,a	n,a
Mongolia	1103	1188	1404	1978	1900	2140	2198	1960	1903	1900
Usbekistan	500	575	600	600	600	500	500	557	522	530
Worldproduction [t]	161,000	178,000	189,000	221,000	223,000	227, 018	244,000	264,000	258,000	258,000

Up to date data on the material flow of molybdenum and its ores and products is hard to come by, hence some of the numbers presented here might be outdated. Concentrated ores are mainly exported by the Netherlands, Chile, Peru, Canada and the USA and imported by the Netherlands, Chile, Belgium, Mexico and the USA. The worldwide exports steadily increased throughout the years 1999-2004. In 2008 exports took a deep fall due to the worldwide economic crisis. Up to 2004 a lot of molybdenum ore concentrate passed through the Netherlands, because of the high treatment capacities of Climax Molybdenum. Molymet processes the imported concentrated ores in Chile and Belgium. Up to 2004 molybdenum ore concentrate exports from Chile steadily increased, but afterwards remained constant due to limited production capacities.

Chile, China, the Netherlands, the USA, Mexico and Belgium are the most important exporters of roasted ores or technical molybdenum oxides. Technical MoO_3 is primarily imported by Japan for processing until ready to use within the country, the Netherlands for processing and exporting an intermediate product, Belgium and Great Britain for the production of ferro-molybdenum, USA, South Korea and Germany for non specified uses. A slight decline in the overall exports can be observed since 2005 due to the dropping activities in the Netherlands. Also China's exports dropped and it's imports are rising because of the increasing need for molybdenum within the country itself.

Molybdenum oxide and -hydroxide are directly used for alloying in the steel-industry. Exports from the USA, Chile and the Netherlands as well as imports by Canada, the Netherlands, Belgium, Germany and Japan continue to grow. Belgium, Chile, Great Britain, Italy, Germany,

France, Austria and China are the world's biggest ferromolybdenum exporters. The Netherlands represent once again a transit-country. The main importers include Germany, Italy, Sweden, France, Taiwan and the USA. 55 % of the world's molybdenum and molybdenum-powder is produced in China. Other manufacturing and exporting countries are the USA, Japan, the Netherlands, Italy, Armenia, Taiwan and Austria. Molybdenum is mainly imported by Germany and Japan.

Regarding the international trade of scrap, there is few conclusive data available. About 2 % of the worldwide molybdenum production comes from recycled scrap. In 2008, 9000 t of Mo-scrap were internationally traded. Higher quality scrap was added to Molybdenum-products, whereas the lower graded scrap served as a raw material for the production of ferromolybdenum.

6000 t of Molybdenum could be obtained from recycled catalysts. The international specifications for MoO_3 and ferromolybdenum can be seen in table 1.2. [4]

Table 1.2: International specifications for molybdenum oxide and ferromolybdenum

	MoO_3 [wt- %]	FeMo [wt- %]
Mo	57	65
C	0.1	0.1
Si		1.5
Cu	0.5	0.5
S	0.1	0.1
Pb	0.05	
P	0.05	0.05

Molybdenum is widely used for different industry segments (figure 1.3). In order to meet the market needs with a recycling product, on the one hand the international specifications and on the other hand the primary uses of the product must be assessed. In the case of molybdenum oxide it serves as a raw material for the ferromolybdenum production as well as the manufacturing of stainless steels, full alloy steels, HSLA, carbon steels, high performance alloys and catalysts. [4]

Recycled materials and scrap represent, especially in the case of critical raw materials, a valuable resource to provide the processing company with a higher degree of independence from fluctuations in prices and delivery bottlenecks. Furthermore an onsite recycling process

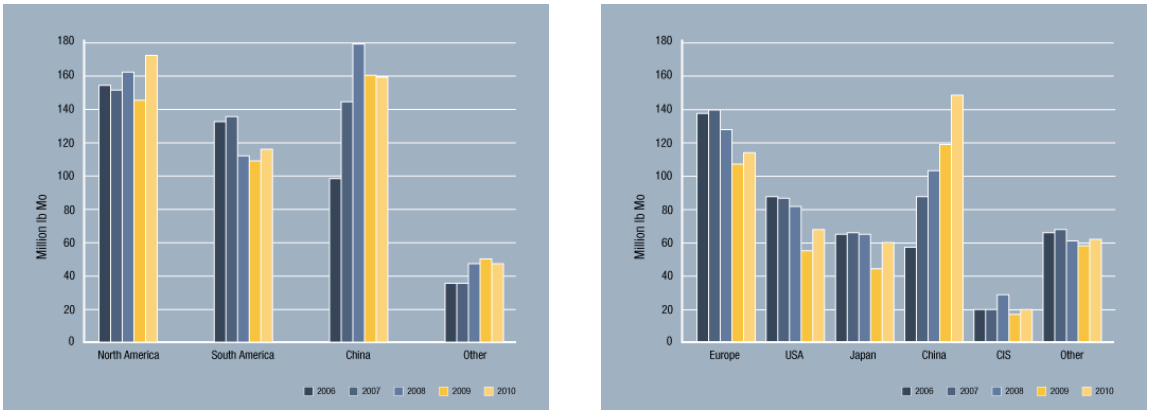

(a) Molybdenum production

(b) Molybdenum usage

Figure 1.2: Worldwide usage and production of molybdenum [3]

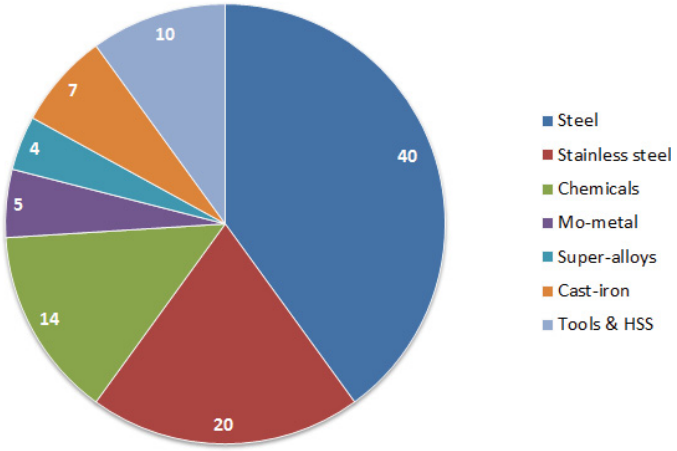

Figure 1.3: Applications of Molybdenum [6]

enables the company to leave assets within company property.

The following chapters present the development and up-scaling of various recycling approaches for refractory metal alloys on the basis of theoretical knowledge, kinetic studies, continuous optimization of the process parameters and detailed analysis of the products.

2 Literature review on oxidation of refractory metals and available recycling technologies

This chapter gives an overview on the oxidation behavior of molybdenum, rhenium and tungsten as well as available methods to study and evaluate their oxidation kinetics. Furthermore an introduction to the rotary kiln and the main factors, influencing the process will be given.

2.1 Oxidation of molybdenum

This section describes the behavior of molybdenum and its oxides under oxygen containing atmospheres. The Molybdenum-oxygen phase diagram is displayed in figure 2.1.

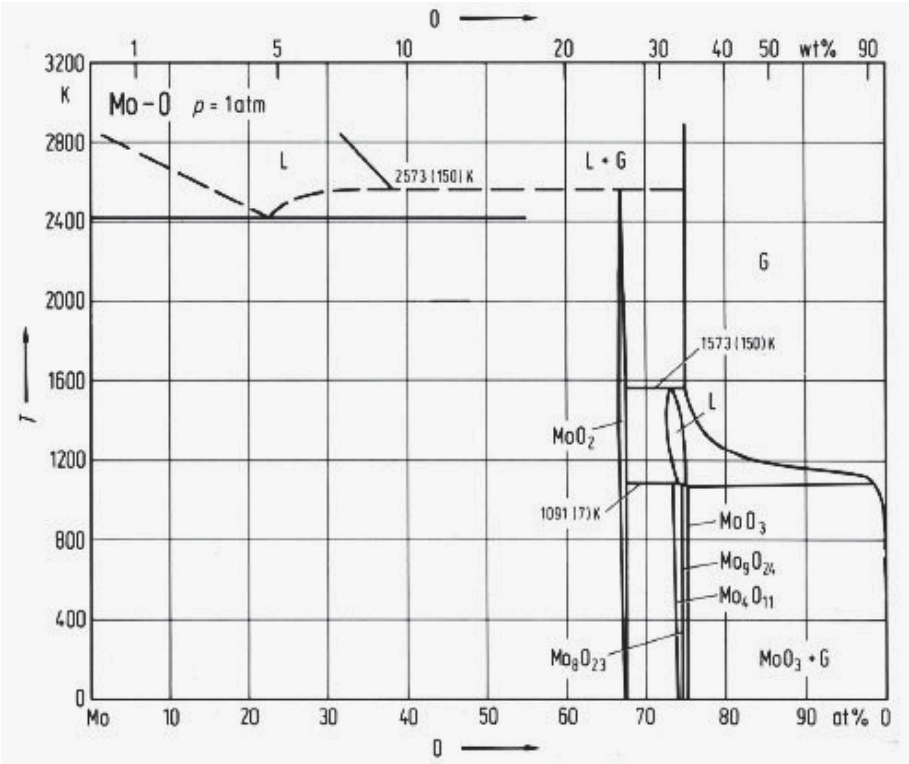

Figure 2.1: Mo-O phase diagram [7]

The oxidation behavior of molybdenum and it's alloys was intensely studied in the course of

developing high temperature alloys [8–10]. Thermodynamically speaking MoO_3 is the most stable oxide. It presents itself with an orthorhombic crystal structure and forms at temperatures exceeding 350 °C. Sublimation sets in at 500 °C, followed by melting at temperatures > 800 °C [8]. When observing the reaction kinetics a parabolic weight gain can be found at temperatures < 650 °C due to limited oxygen supply on the sample surface. The formed MoO_3 acts as an inhibitive layer, leading to a diffusion controlled oxidation process, which can be described through equation 1 [8, 11]. If temperatures exceed 650 °C, a linear weight gain can be found. Due to the increasing sublimation rate a linear weight loss can be observed at temperatures greater than 700 °C. Equation 2 describes the decreasing sample weight within the temperature range 700-800 °C.

$$k_p = 7,93 \cdot 10^{10}\ e^{(-160,6\ kJ/mol\ R\ T)} \left[\frac{mg}{cm^2\ h^{0,5}}\right] \tag{1}$$

$$k_l = -1,84 \cdot 10^{17}\ e^{(-304,6\ kJ/mol\ R\ T)} \left[\frac{mg}{cm^2\ h}\right] \tag{2}$$

The results displayed in figure 2.2 were found through cyclic-isothermal experimental setup. [12]

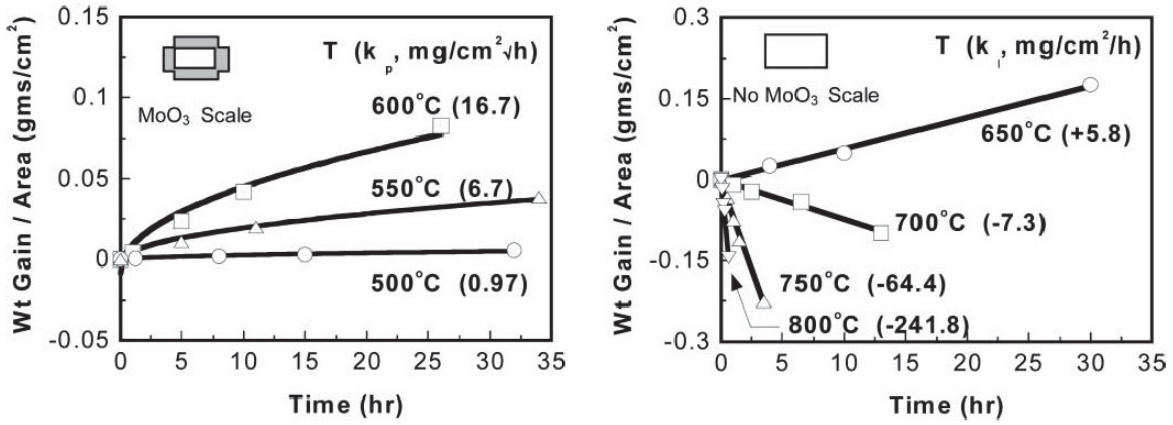

Figure 2.2: Oxidation kinetics of pure molybdenum at different temperatures; left: parabolic weight gain at temperatures < 650 °C, right: linear weight gain at 650 °C; linear weight loss at temperatures exceeding 700 °C [12]

The conversion of of molybdenum by oxygen strongly depends on the present temperature and pressure conditions. After the adsorption process at room temperature, a visible reaction and the formation of a tarnish film starts at about 300 °C [8, 13, 14]. Specialized optical methods using polarized light can detect oxidation products on Mo samples in oxygen starting at 150 °C. Up to 600 °C a dark-blue/black oxide layer is formed. The formation of MoO_3 reaches its

maximum rate at 600°C, whereas the intermediate layer of MoO_2 still remains very thin. If the temperature exceeds 800 °C the oxidation runs according to a linear time-related law, though strongly influenced by the gas velocity of the atmosphere. If there exists no gas velocity, the sample is covered in a cloud of sublimed oxides and accordingly higher partial pressure thereof, which inhibits the oxidation process because newly formed oxides need to diffuse through this atmosphere. Also a reduction of the oxygen content close to the sample can occur if no gas velocity prevails, leading once again to a diffusion process for oxygen molecules towards the sample surface. The activation energy for the oxidation process within various temperature ranges are displayed in table 2.1. The data for the temperature range 450-550 °C includes changes within the crystal structure, as well as wrinkling of the surface, and is therefore not representative for the true activation energy. [8]

Table 2.1: Activation energy for the oxidation of molybdenum within various temperature ranges [15–17]

Temperature [°C]	Activation energy [kJ/mol]
150-300	84 [15]
450-550	193 [16]
500-600	205 [17]

At temperatures exceeding 600 °C the formation of MoO_2 reaches a steady state and an equilibrium with the further oxidation towards MoO_3 at 725 °C. An autocatalytic reaction can increase the oxidation rate at temperatures higher than 725 °C. MoO_3 melts at 795 °C, making it more difficult to characterize the oxidation process due to the formation of molten MoO_3 or a MoO_2-MoO_3 eutectic. This process however still runs through the generation of MoO_2, which then quickly oxides to MoO_3, that thereafter melts and sublimes.

The sublimation of MoO_3 starts at 500 °C. The ratio formation of oxide-layer to sublimation of oxide is complicatedly related to the temperature, whereas the sublimation of MoO_3 alone runs according to a linear reaction rate. The activation energy for the MoO_3 sublimation can be seen in table 2.2. [8]

The surface ablation of a molybdenum sample due to oxidation depends on the partial Mo oxide pressure close to the sample surface which is equivalent to the gas velocity and also strongly depends on whether the gas beam is directly pointed at the sample or not (figure 2.3).

Table 2.2: Activation energy for the sublimation of molybdenum oxide within various temperature ranges [11, 17]

Temperature [°C]	Activation energy [kJ/mol]
580-650	222 [17]
650-750	375 [11]

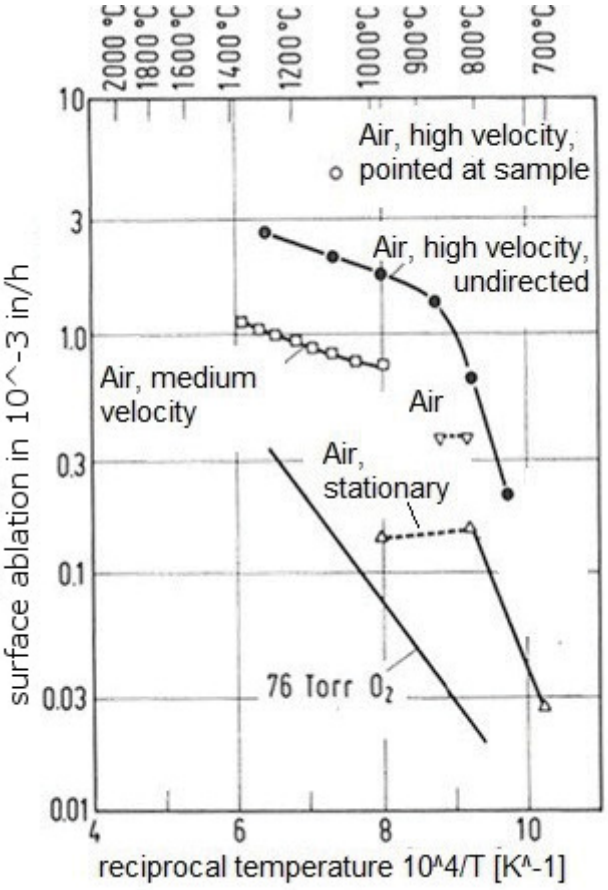

Figure 2.3: Oxidation of molybdenum in air and oxygen at different conditions

Slightly different data has been published by various authors. Gulbransen and Wyson [13] stated an oxidation behavior < 400 °C that can be fitted to a parabolic rate law and an overall activation energy of 151 kJ/mol. The volatilization of molybdenum trioxide was observed at 475 °C in vacuum conditions. The transition from a parabolic to a linear rate law was postulated to occur at 500 °C. Additionally, the evaporation of MoO_3 was observed at 650 °C in 1 atm oxygen atmosphere [17]. When oxidizing Mo in static air, MoO_3 sublimes as fast as it forms at 938 °C [11]. The rate of oxidation was observed to be nearly constant above 795 °C [18].

The diffusion coefficient for O_2 in MoO_3 can be evaluated according to different methods. When using EMF (electromagnetic force) within the range of 410-500 °C at 0.21 and 100 atm O_2 pressure the diffusion coefficient results in $D = 9.1 \cdot 10^{-8} exp^{\frac{-20300}{RT}}$, which gives a diffusion coefficient of $1.13 \cdot 10^{-13}$ cm²/s for 480 °C [19]. Through an isotope tracking method diffusion coefficients of $D = 1.36 \cdot 10^{-18}$ cm²/s at 480 °C and $D = 1.4 \cdot 10^{-16}$ cm²/s at 510 °C were deducted. The activation energy remains constant at 26 kJ/mol from 300-600 °C with irregularities between 480 and 510 °C [20]. The diffusion coefficient of oxygen in MoO_3 between 500 and 600 °C can be described as $D = 1.7 \cdot 10^{-5} exp^{\frac{-24000}{RT}}$ cm²/s [8].

Molybdenum-oxide in oxygen atmoshere

The exchange of oxygen atoms (equation 3) is a diffusion controlled process in fine molybdenum oxide powders. Fast diffusion resulted from the possibility for all the oxygen atoms within the Mo oxide to participate in this process. The exchange process runs according to a first order reaction rate.

$$O_2\ (gas) \Leftrightarrow 2\ O\ \ (in\ MoO_3) \tag{3}$$

The kinetics of the sublimation can be determined by the vapor pressure of the oxides and gravimetric methods. In O_2 or N_2 atmospheres the sublimation rates strongly depend on the gas velocity and temperature. Gravimetrical measurements of technical MoO_3 in air show that the sublimation rate due to rising temperatures increases the most within the first hour at an activation energy of 5 kcal/mol. Thereafter the activation energy for the MoO_3 sublimation is 15 kcal/mol. The table 2.3 compares the weight loss of MoO_3 samples under O_2 atmosphere at different temperatures. In air (40 l/h) sublimation sets in at 650 °C. The sublimation rate increases if graphite is present. Experiments investigating MoO_3 sublimation in rotary kilns postulate an influence of temperature of the carrier gas as well as the furnace and rotation speed. [8]

2.2 Oxidation of tungsten

The phase diagram of tungsten and oxygen can be seen in figure 2.4.

Table 2.3: Sublimation rates according to temperature and gas velocity of 40 l/h O_2

Temperature [°C]	weight loss [wt- %/h]
600	0.1
700	3.4

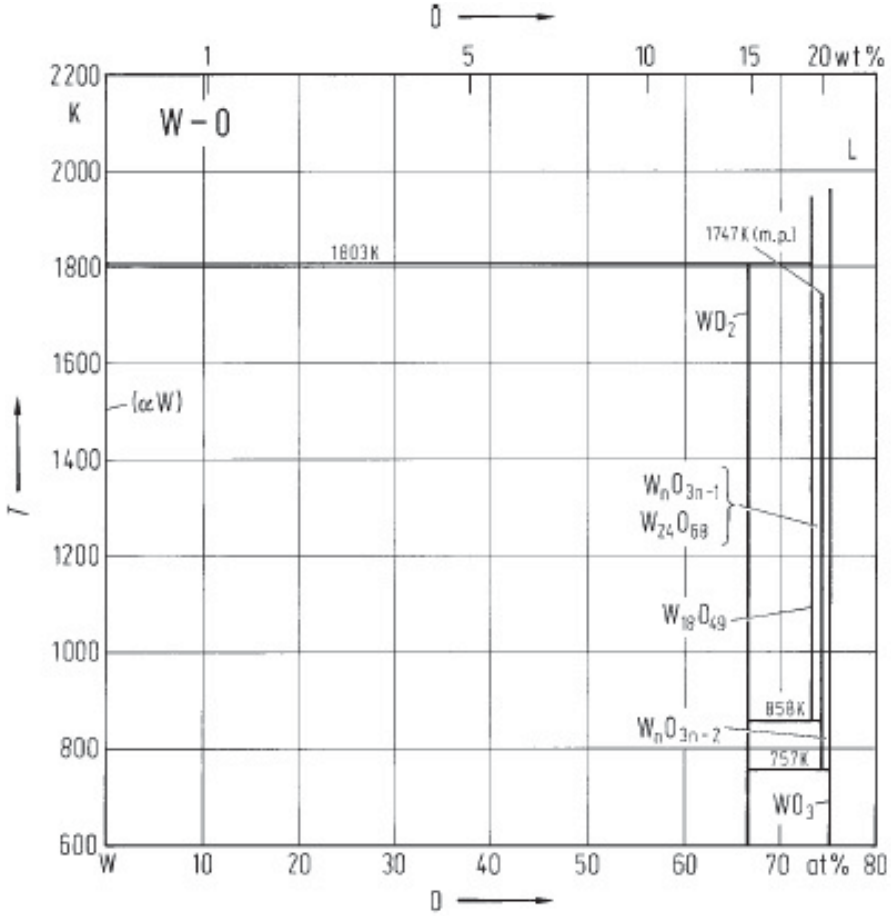

Figure 2.4: W-O phase diagram [21]

Tungsten shows no visible signs of oxidation in oxygen-containing atmospheres until 200 °C. Tungsten powder however oxidizes at room temperature using the humidity in the air as an oxygen source [22]. Compact tungsten forms a thin, dark-blue $WO_{2.75}$ oxide layer at temperatures exceeding 327 °C. The growth of this layer is diffusion controlled and expands according to a parabolic time law. [22, 23]

Starting at 627 °C a porous, yellow WO_3 layer occurs on top of the $WO_{2.75}$ intermediate layer. At temperatures between 777 and 1027 °C oxygen is exclusively used to build up the WO_3 layer. Due to the porosity of the layer further oxidation of the material strongly depends on

the availability of tungsten ions at the WO_3-$WO_{2.75}$ boundary. Higher temperatures lead to an increasing influence of the oxygen pressure on the oxidation rate. WO_3 begins to sublime at 977 °C. At 1277 °C the sublimation of oxide equals its formation, hence the surface remains oxide free. The ablation of the tungsten sample surface proceeds linearly with time at this stage. The material removal increases with rising temperatures and O_2 pressure until 1827 °C. If conditions present low O_2 pressure and high temperatures (< 1827 °C) the amount of vaporized WO_2 is higher than that of WO_3. At temperatures exceeding 1827 °C the mass of formed tungsten oxide is diminished due to thermal desintegration of the oxides. A notable vaporization of metallic tungsten sets in at 2327 °C. [23]

Experiments investigating oxidation mechanisms on a micro scale were able to deliver some deeper insights. As mentioned before, tungsten surfaces remain oxide free in oxygen containing atmosphere for two hours at 327 °C, [24]. However if formed oxides are removed in vacuum at a temperature of 997 °C, small amounts of oxygen can thereafter be detected on the sample surface at room temperature and 0.133 bar O_2. [25]. Investigations on the composition of the formed nano-scale oxide layer (3-4.5 nm) used an argon-ion-beam, targeted at the sample-surface, as well as a mass spectrometer and found that the formed oxides used oxygen that was accumulated on the sample-surface to form W_2O_3, WO_2, WO_3 and W_2O_6 after a certain latency period, that decreases with rising O_2 pressure [26]. Gravimetric experiments also proof the formation of a nanoscale oxide layer on polished tungsten surfaces. The figure 2.5 shows the increasing weight over time at different temperatures at 0.133 bar O_2 pressure. The oxide layer seems to reach it's maximum extent after 20-80 min. This equals a layer thickness of 23-34 nm WO_3. [14, 23]

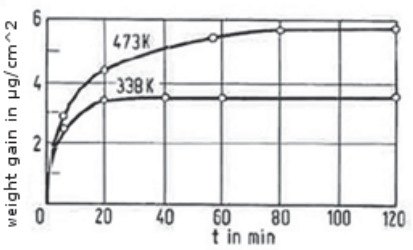

Figure 2.5: Formation of oxide layer on polished tungsten sample at different temperatures and 0.133 bar O_2 [23]

The formation of a thin dark-blue oxide layer begins, as already described at 327 °C. The

extension of this layer increases with rising temperature. The figure 2.6 displays the gain in weight due to the formation of oxide at a pressure of 0.101 bar O_2. After two hours at 500 °C, the oxide layer is 675 nm thick.

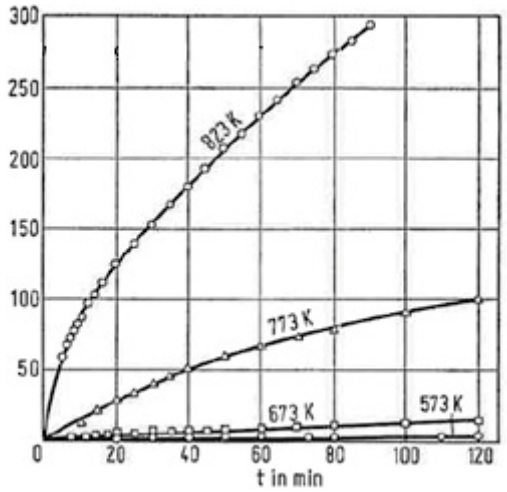

Figure 2.6: Formation of oxide layer on unpolished tungsten sample at different temperatures and 0.101 bar O_2 [23]

At temperatures exceeding 597 °C, the formed oxide layer starts to crack and chip at 625 °C. The chipping facilitates the availability of oxygen on the surface sample which leads to an increase in oxidation rate (figure 2.7) and the formation of a yellow oxide layer on top of the blue one. At 650 °C the sample is completely covered with the yellow WO_3 layer on top of the dark-blue layer, which consists of WO_3 and W_4O_{11}. [23, 27]

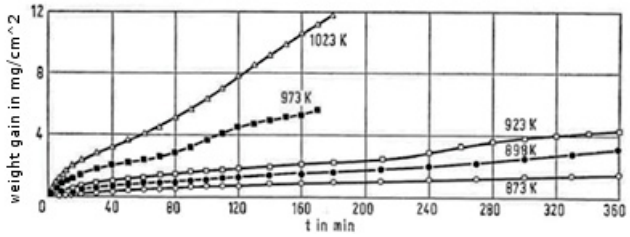

Figure 2.7: Formation of oxide layer on unpolished tungsten sample at different temperatures and 0.101 bar O_2 [23]

Further oxidation under atmospheric pressure leads to a porous structure of the yellow WO_3 at 697 °C [24]. The growth of the porous, yellow oxide layer follows a linear time law, due to the fact, that in order for the oxidation to take place the tungstenions need to be transported to the WO_3-W_4O_{11} boundary. A complete oxidation of a tungsten sample at 800 °C and 1 atm

O_2 proceeds in three stages (figure 2.8a). Within the section 0-A the weight of the sample increases parabolically and in section A-B linearly. The weight increases 60 % within seven hours. Oxidation times exceeding point B lead to a decrease in oxidation rate due to a decline of the ratio unoxidized material to formed oxide. Various literature sources state oxidation rates ranging from 9.9 mg/cm^{2}h at 800 °C to 4.5 mg/cm^2·h at 750 °C within the linear section of the curve. If thin tungsten sheets are grinded and oxidized, the weight development is s-shaped (figure 2.8b). After the linear section A-X the oxidation-rate increases probably due to an increase of surface caused by chipping of the material because of the formation of WO_3 which is more voluminous than tungsten itself. The oxidation time increases significantly for ground tungsten samples (8x8x20 mm). Only one third of the total sample is oxidized after 24 hours in 1 atm air and 900 °C. The table 2.4 shows the weight increase of tungsten samples due to oxidation in air under 1 atm pressure at different temperatures. The intermediate $WO_{2.75}$ layer is very thin (0.00200-0.00135 cm), when oxidizing under 1 atm O_2 at temperatures from 700-1000 °C. [23]

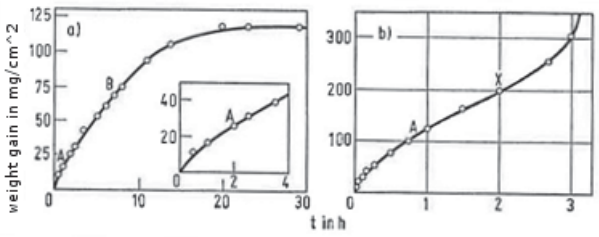

Figure 2.8: Formation of oxide layer on unpolished tungsten sample at different temperatures and 1.013 bar O_2 [23]

Table 2.4: Weight increase [%] of tungsten samples in air at atmospheric pressure

Time [h]	1	5	24	48
Weight increase [%] at 700 °C	0.036	0.111	0.360	0.629
Weight increase [%] at 900 °C	0.274	1.55	8.71	14.8

The oxidation of tungsten under dynamic conditions differs from static states as follows. Polished tungsten samples show an increase in weight of 0.037 g/cm^2 after one hour in an airflow of 2.124 m^3/h at 1 atm and 982 °C. There exists no significant influence of the gas velocity under these conditions. Compared to the oxidation rate of molybdenum (see section 2.1), the observed oxidation rate in tungsten samples is lower. If oxygen (2-5 l/h, 1 atm) and elevated

temperatures (700-1000 °C) are applied to a tungsten sample, the formation of both, the dark-blue $WO_{2.75}$-WO_3 as well as the yellow WO_3 layers can be observed under these dynamic conditions. The dark-blue layer reaches it's maximum extension after 5 min at 700 °C. The formation rate is proportional to the inverted temperature. The top yellow layer still remains very thin after 5 min, however it continues to grow until it's extension comprises 1 mm. The porosity of the yellow oxide layer amounts to 30 %. [23]

Tungsten-oxide in oxygen atmoshere

Tungsten oxide (WO_3) is inert in air at room temperature. However if heated it reduces its oxygen content, which makes a stoichiometrical notation of the oxide difficult and it furthermore releases adsorbed water at 100 °C. Tungsten oxide begins to sublime at 950 °C. The table 2.5 displays the various conditions of WO_3 in inert atmosphere in a Pt-container [28].

Table 2.5: WO_3 conditions under inert atmosphere

Temperature [°C]	color	composition
1150	yellow	WO_3
1200	green	WO_3
1300	grey	WO_3
1400	black	WO_3
1450	blue/black	$WO_{2.95}$

The thermal desintegration of WO_3 can be enhanced by the presence of potassium, aluminum or nickel. [29]

If WO_3 is exposed to an oxygen-containing gas stream (1 atm) and heated to 525 °C it will even after 50 hours still remain it's original yellow color. Tungsten oxide changes it's color to light green after being exposed to an oxidizing gas stream for 40 or 20 hours at 870 or 1150 °C respectively [30]. A monolayer of adsorbed oxygen, which reaches it's maximum extension at 400 °C is formed on tungsten oxide powder with a surface area of 1.3 m^2/g between 100 and 500 °C. The oxygen saturation is achieved after 10 min [31]. Due to the fact, that the grain boundary diffusion rate determines the exchange rate of oxygen atoms, it is constant at first, but declines later on. These results were found within a temperature range of

400 to 750 °C. The recorded temperature shows several kinks due to changes of the specific surface area and hence the oxygen exchange rate. The activation energies for the oxygen exchange process at different temperature ranges are displayed in table 2.6. According to studies, using isotopes, all oxygen atoms within the WO_3 molecule participate in the exchange process. Actual exchange runs faster than theoretically calculated, probably due to lattice vacancies in WO_{3-x} molecules, which also reflects in a higher empirical activation energy [32]. [29]

Table 2.6: Activation energy for oxygen exchange in WO_3 molecules under oxygen containing gas stream

Temperature [°C]	Activation energy [kJ/mol]
385-412	318
423-440	340.6
458-573	69.04
592-651	118.8
665	412.5
704	48.2
721-732	201.7

2.3 Oxidation of rhenium

The binary phase diagram of rhenium and oxygen is not yet known, however selected phases are described in the literature. The table 2.7 shows the oxides described in the literature so far.

Table 2.7: Rhenium-oxide phases stated in the literature [33]

Phase	Structure
ReO_2	monoclin/orthorhombic
Re_7O_{18}	hexagonal
ReO_3	cubic
Re_2O_7	orthorhombic

Rhenium reacts in oxygen containing atmospheres according to equation 4. The generated yellow rhenium oxide sublimes at 363 °C. [34, 35]

$$2\ Re + 3.5\ O_2 = Re_2O_7 \qquad (\Delta H = -1241kJ/mol) \tag{4}$$

The sublimation temperature for Rhenium(VII) (363 °C) turns out quite low, compared to the melting-point of tungsten oxid (ca. 1470 °C) which makes a separation of the two oxides possible, when operating a furnace at a temperature range of 500 to 1000 °C. The oxidation kinetics are inhibited by the formation of a tungsten oxide layer on the surface of tungsten and tungsten-rhenium alloy samples. At temperatures exceeding 800-900 °C, the oxidation rate is larger in tungsten-rhenium alloys than in pure tungsten due to the fact that the subliming rhenium constantly introduces cracks into the tungsten oxide layer. The formation of a laminar boundary layer slows down oxidation rates, which can be counteracted by applying higher gas velocities. This increases the oxidation rate 10-fold compared to a static situation. In order to recycle tungsten-rhenium alloys, there are according to literature two oxidation steps to be taken. First the scrap is oxidized in pure oxygen at 1000 °C. The sublimed rheniumoxide then has to be purified through a second sublimation step at 350-400 °C and processed hydrometallurgically thereafter. [35]

The figure 2.9 displays a furnace to perform the W-Re alloy recycling process described above. The best yield of rhenium oxide could be achieved at 950 °C with pure oxygen (3 l/min) in a tube, 10 cm in diameter and 1.2 m long. The gas stream was cleaned of the remaining rhenium oxide with water and hydrogenperoxide. [36]

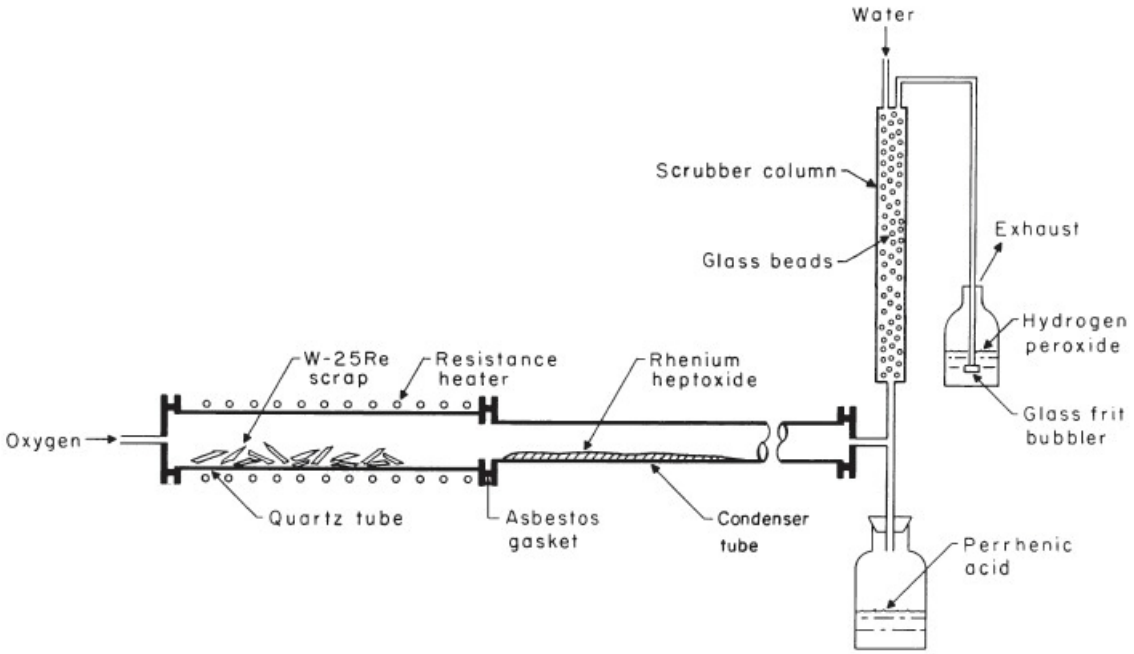

Figure 2.9: Furnace for separation of a W-Re-alloy through oxidation and sublimation [36]

2.4 Oxidic compounds with Mo-Nb, Mo-Ta, Mo-W and W-Re

There is only few information available and no complete ternary phase diagrams on oxygen with Mo-Nb, Mo-Ta, Mo-W or W-Re are stated in the literature so far. However some selected phases are described and displayed in table 2.8 [37].

Table 2.8: Oxidic compounds with Mo-Nb, Mo-Ta, Mo-W and W-Re

Mo-Ta-O	Mo-Nb-O	Mo-W-O	W-Re-O
$Ta_{12}MoO_{33}$	$Nb_{12}MoO_{33}$	$Mo_{11}W_{11}O_{32}$	
Ta_8MoO_{33}	Nb_8MoO_{33}		none
	$Nb_{14}Mo_3O_{44}$		described
	$Nb_2Mo_3O_{14}$		

2.5 Methods to investigate oxidation kinetics

The following section will provide some basic knowledge for the design of a study to investigate oxidation kinetics of refractory metal alloys. Mainly two different approaches are used to

describe the oxidation behavior of metals. The isothermal cyclic oxidation method involves repeated exposure of the sample to a set temperature and gravimetrical measurements between the exposure times. Whereas when using the non-isothermal approach the change in weight is recorded, while the sample passes through a set temperature range.

2.5.1 Non-isothermal oxidation

Non-isothermal oxidation experiments offer insights into the effect of temperature at a set heating rate and the current reaction rate on the activation energy. Solid samples can be analyzed with a thermobalance; powders through DTA-TG (differential thermal analysis - thermogravimetry) analysis. Heating rates will be varied and the effect on the changes in sample weight studied. Non-isothermal methods provide a first indication to what temperatures should be investigated in an isothermal approach. Measuring the change in weight gives data on ongoing oxidation and/or sublimation of the material. [38, 39]

2.5.2 Isothermal cyclic oxidation

Here, samples have to be exposed to the furnace temperature and atmosphere for a set amount of time in each cycle. In between cycles the samples are weighted using a precision scale. The structure and chemical composition of the formed oxide layer is analyzed after the last cycle through [38–42]:

- SEM
- SEM/EDX
- XRD
- ICP

2.5.3 Evaluation of kinetic experiments with regard to the sample's dimensions

The evaluation of isothermal experiments is done according to the equations described in section 2.5. In case the sublimation of the formed oxide runs faster than the formation of the oxide itself and hence no product layer will build up, the rate constant can be calculated as follows when the dimensions of the sample (figure 2.10) are taken into account.

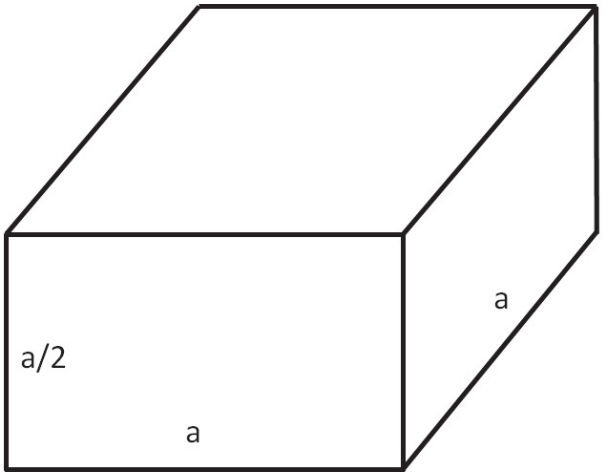

Figure 2.10: Sample dimensions for kinetic experiments

The reduction of sample weight and surface area over time can be described through equations 5, 6 and 7 [43]:

$$-\frac{\delta W}{t} = kAC \tag{5}$$

W ... sample weight, t ... time, k ... rate constant, A ... exposed sample surface area, C ... concentration of reagent [cm^3/mol]

$$A = a^2 + 4\frac{a}{2}a = 3a^2 \qquad W = \frac{a^3}{2}\rho \qquad a = \left(\frac{2W}{\rho}\right)^{\frac{1}{3}} \qquad A = 3\left(\frac{2W}{\rho}\right)^{\frac{2}{3}} \tag{6}$$

a ... lateral length, ρ ... density of the material

$$
\begin{aligned}
-\frac{\delta W}{\delta t} &= 3k\left(\frac{2}{\rho}\right)^{\frac{2}{3}} W^{\frac{2}{3}} C \\
-\int_{W_o}^{W} \frac{1}{W^{\frac{2}{3}}}\delta W &= 3k\left(\frac{2}{\rho}\right)^{\frac{2}{3}} Ct \\
3\left(W_o^{\frac{1}{3}} - W^{\frac{1}{3}}\right) &= 3k\left(\frac{2}{\rho}\right)^{\frac{2}{3}} Ct \\
\left(W_o^{\frac{1}{3}} - W^{\frac{1}{3}}\right) &= k\left(\frac{2}{\rho}\right)^{\frac{2}{3}} Ct
\end{aligned}
\tag{7}
$$

The rate constant will be obtained through plotting $\left(\frac{2}{\rho}\right)^{\frac{2}{3}} Ct$ against $\left(W_o^{\frac{1}{3}} - W^{\frac{1}{3}}\right)$. The dependence of the rate on the temperature (equals the activation energy when the conversion of the sample is due to a single chemical mechanism) can be evaluated through plotting the rate constants against $\frac{1}{T}$ and interpreting the inclination of the data points.

The diffusion of the reagent through the product layer occurs in the case of its formation. The following calculations refer to a_1 as the original dimensions of the sample, whereas a_0 describes the lateral length of the unreacted core of the sample. Equation 8 defines the mass-flow of the reagent in general. [43]

$$
J = -A\mathcal{D}\left(\frac{\delta C}{\delta a}\right) \tag{8}
$$

D . . . diffusion rate of the oxygen through the product layer, A . . . exposed surface area of the sample, δC . . . concentration gradient of the reagent in the product layer, δa . . . thickness of the product layer

The concentration of the reagent at the boundary surface equals $C_i = 0$ for diffusion controlled processes, thus resulting in equation 9.

$$
\begin{aligned}
J &= -3a^2\mathcal{D}\left(\frac{\delta C}{\delta a}\right) \\
\int_{C_i}^{C} \delta C &= -\frac{J}{3\mathcal{D}}\int_{a_0}^{a_1} \frac{\delta a}{a^2} \\
C - C_i &= -\frac{J}{3\mathcal{D}}\left(\frac{a_1 - a_0}{a_0 a_1}\right) \\
J &= -3\mathcal{D}\left(\frac{a_0 a_1}{a_1 - a_0}\right) C
\end{aligned}
\tag{9}
$$

Equations 10 and 11 describe the amount of remaining, unreacted material.

$$\begin{aligned} R &= -\frac{a_1^3 - a_0^3}{a_1^3} \qquad & R &= 1 - \left(\frac{a_0}{a_1}\right)^3 \\ 1 - R &= \left(\frac{a_0}{a_1}\right)^3 \qquad & a_o &= a_1(1-R)^{\frac{1}{3}} \end{aligned} \tag{10}$$

R . . . degree of conversion

The remaining unreacted material at a certain point in time (t) can be derived as follows:

$$\begin{aligned} N &= \frac{a_o^3 \rho}{2M} \\ \frac{\delta N}{\delta t} &= \frac{\delta N}{\delta a_0}\frac{\delta a_0}{\delta t} = \frac{3a_0^2\rho}{2M}\frac{\delta a_0}{\delta t} \end{aligned} \tag{11}$$

N . . . number of unreacted mol material, ρ . . . density of sample material,
M . . . molecular weight

The change in amount of remaining, unreacted material for this diffusion controlled process equals the mass flow of the reactant, when taking the stoichiometry into account (equation 12):

$$\begin{aligned} J = -3\mathcal{D}\left(\frac{a_0 a_1}{a_1 - a_0}\right)C &= \alpha\frac{3\rho}{2M}a_0^2\frac{\delta a_0}{\delta t} \\ \frac{-2\mathcal{D}CM\delta t}{\alpha\rho} &= a_0^2\left(\frac{1}{a_0} - \frac{1}{a_1}\right)\delta a_0 \\ \frac{-2\mathcal{D}CM\delta t}{\alpha\rho} &= \left(a_0 - \frac{a_0^2}{a_1}\right)\delta a_0 \\ \frac{-2\mathcal{D}CMt}{\alpha\rho} &= \int_{a_1}^{a_0}\left(a_0 - \frac{a_0^2}{a_1}\right)\delta a_0 \\ \frac{-2\mathcal{D}CMt}{\alpha\rho} &= \left[\frac{a_0^2}{2}\right]_{a_1}^{a_0} - \left[\frac{a_0^3}{3a_1}\right]_{a_1}^{a_0} \\ \frac{-2\mathcal{D}CMt}{\alpha\rho} &= \frac{a_0^2}{2} - \frac{a_1^2}{2} - \frac{a_0^3}{3a_1} + \frac{a_1^2}{3} \\ \frac{-2\mathcal{D}CMt}{\alpha\rho} &= -\frac{a_1^2}{6} - \frac{a_0^3}{3a_1} + \frac{a_0^2}{2} \\ \frac{2\mathcal{D}CMt}{\alpha\rho} &= \frac{a_1^2}{6} + \frac{a_0^3}{3a_1} - \frac{a_0^2}{2} \end{aligned} \tag{12}$$

α. . . stoichiometrical factor (in the case of the reaction $Mo + 3\ O = MoO_3$ the stoichiometrical factor equals 3).

When taking the degree of conversion into account, the following equations (equation 13) apply:

$$\begin{aligned} a_0 &= a_1(1-R)^{\frac{1}{3}} \\ \frac{2\mathcal{D}CMt}{\alpha\rho} &= \frac{a_1^2}{6} + \frac{a_1^3(1-R)}{3a_1} - \frac{a_1^2(1-R)^{\frac{2}{3}}}{2} \\ \frac{2\mathcal{D}CMt}{\alpha\rho} &= (\frac{1}{6} + \frac{1}{3}(1-R) - \frac{1}{2}(1-R)^{\frac{2}{3}})a_1^2 \\ \frac{2\mathcal{D}CMt}{\alpha\rho} &= (1 + 2(1-R) - 3(1-R)^{\frac{2}{3}})\frac{1}{6}a_1^2 \\ \frac{2\mathcal{D}CMt}{\alpha\rho} &= (1 + 2 - 2R - 3(1-R)^{\frac{2}{3}})\frac{1}{6}a_1^2 \\ \frac{2\mathcal{D}CMt}{\alpha\rho} &= (3 - 2R - 3(1-R)^{\frac{2}{3}})\frac{1}{6}a_1^2 \\ \frac{2\mathcal{D}CMt}{\alpha\rho} &= (\frac{1}{2} - \frac{1}{3}R - \frac{1}{2}(1-R)^{\frac{2}{3}})a_1^2 \end{aligned} \tag{13}$$

This approach shows inaccuracies when conversion rates exceed 90 %, because the change in volume of the sample is not accounted for. A plot of t against $\frac{1}{2} - \frac{1}{3}R - \frac{1}{2}(1-R)^{\frac{2}{3}})a_1^2$ should result in a straight line. This deduction was done on the basis of Habashi [43], Crank [44] as well as Ginstling and Brounshtein [45].

2.5.4 Theoretical background for the evaluation of the activation energy

The calculation of the gibbs free energy (equation 14) for the oxidation of the individual elements of the alloy can provide a first indication towards the oxidation behavior of the investigated alloy.

$$\Delta G = -RTlnK = -RTln\frac{(a_{oxide})^x}{(a_{element})^y(p_{O_2})} \tag{14}$$

ΔG... gibbs free energy, R... gas constant, T... temperature, $a_{Element} = 1$... activity of element, a_{Oxid}= 1... activity of oxide, p_{O_2}... partial oxygen pressure, x, y... stoichiometric coefficients

A lower gibbs free energy, a lesser minimally required activity of the element for the formation of the oxide and a higher equilibrium constant increase the probability for the oxidation of the element, although the change in activity of the elements in a binary system has to be taken into account.

To evaluate the predominant reaction mechanism through kinetic parameters, the following equations 15-19 are available. The extent of conversion of the sample can be calculated through equation 15.

$$\gamma = \frac{w - w_A}{w_E - w_A} \tag{15}$$

γ ... extent of conversion, w ... present weight, w_A ... weight in the beginning, w_E ... weight at the end

The effect of the temperature (depending on the heating rate) on the activation energy in non-isothermal oxidation experiments can be calculated according to equation 16 [46].

$$g(\gamma) = \int_0^T \frac{A}{\beta}\, exp\left[\frac{-E_a}{RT}\right] dT \tag{16}$$

T ... temperature, R ... gas constant, E_a ... activation energy, β ... heating rate, A ... constant, $g(\gamma)$ ... integrated form of γ

The effect of the temperature due to changed heating-rates onto the activation can be deduced from models like Kissinger-Akahir-Sunose (KAS) and results in equation 17 [46].

$$ln\frac{\beta_i}{T^2_{\gamma,i}} = constant - \left[\frac{-E_a}{RT_{\gamma,i}}\right] \tag{17}$$

T ... temperature, R ... gas constant, E_a ... activation energy, β ... heating rate, i ... various heating rates, γ ... degree of sample oxidized

The influence of the temperature onto the activation energy in isothermal experiments can be expressed through equation 18 [46].

$$g(\gamma) = \int_0^t A\, exp\left[\frac{-E_a}{RT}\right] dt \tag{18}$$

t ... time, R ... gas constant, E_a ... activation energy, A ... constant

The change in activation energy due the change in oxidation degree over time can be described through equation 19 [46]

$$t_\gamma = \frac{1}{A\, exp\left[\frac{-E_a}{RT}\right]} \tag{19}$$

t ... time, to have passed until the conversion degree γ is reached, R ... gas constant, E_a ... activation energy, A ... constant

The constant A is directly proportional to the degree of conversion of the sample and can therefore be derived from repeated isothermal experiments. [12, 46]

2.6 Rotary kiln

Rotary kilns are are widely used for processing different materials. The figure 2.11 displays a schematic layout of a rotary kiln. In order to meet the needs of rotary kiln technologies for metallurgical purposes, calzination as well as reduction processes and the cement industry this type of furnace comes in different shapes. The way of heat transfer to the material is one of the main criteria for classifying the furnaces:

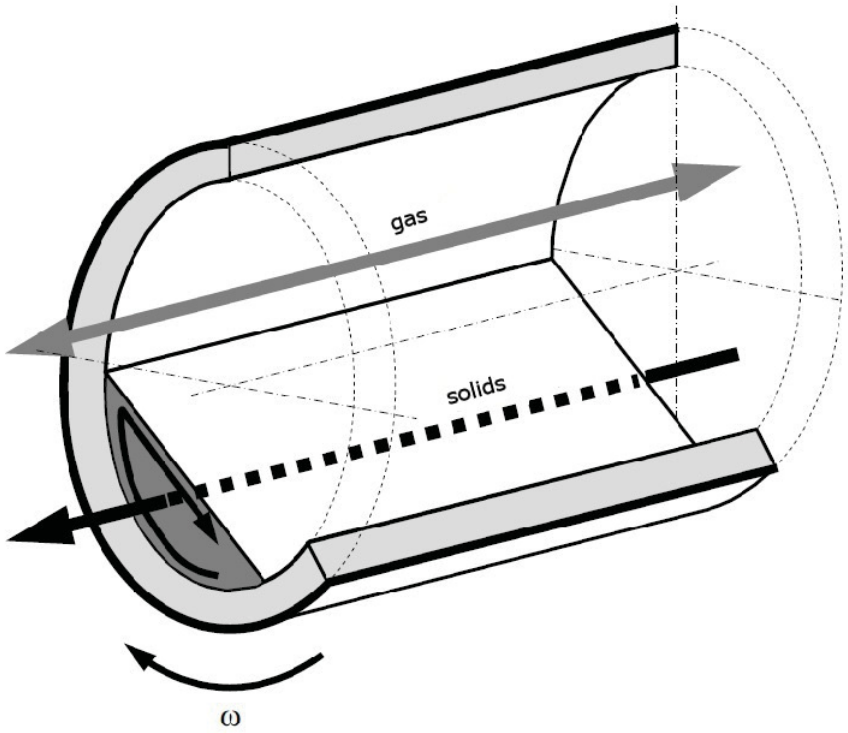

Figure 2.11: Schematic layout of a rotary kiln [47]

- Directly heated rotary kiln: Gas burners heat the oven atmosphere.
- Indirectly heated rotary kiln: Heating elements, steam or waste gas heat the outside of the kiln and therefore the heat has to pass the furnace wall.

Common elements of all rotary kilns are material charging screws or containers, which ensure a steady material flow into the furnace. Directly heated kilns mostly consist of steel with a

refractory lining. If indirectly heated, there exists no refractory lining. The rotation is introduced via an engine, connected to the kiln by a gear wheel. The end of the kiln usually includes a container to store processed material. In order to control the process the furnace has gaskets to protect the oven atmosphere against the surrounding air. Gas and material usually flow in counter current to enhance the yield of the process, which will be mainly influenced by the following parameters.

- Temperature
- Atmosphere within the furnace
- Gas velocity
- Rotating speed
- Inclination of the kiln
- Filling degree

2.7 Behaviour of the bed within the rotary kiln

Within a bed there are always two layers and three possible transversal transport mechanisms (figure 2.12).Particles in the active layer can either

- glide
- roll
- cascade

on the inactive layer beneath it. For most industrial processes, rolling is the most preferable, due to the superior mixing of the bed and the constant renewal of the active layer.
The Froud number (equation 20), which takes into account the diameter and the rotation speed of the kiln can provide an estimation on which transversal material flow will occur. [48]

$$Fr = \frac{\omega^2 R}{g} \tag{20}$$

ω... angular velocity, R... inner diameter of the kiln and g... gravity acceleration

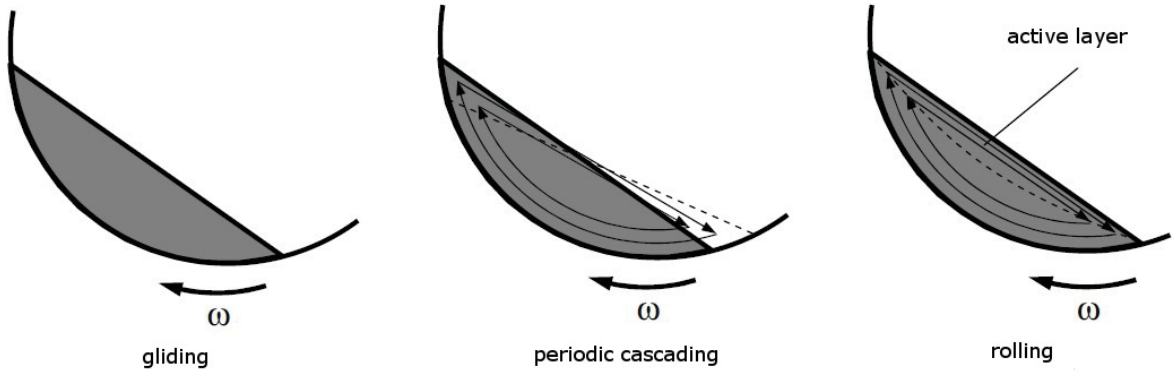

Figure 2.12: Transversal material transport through the kiln [47]

The equation 21 is in good accordance with experimental results, taking into account the ratio of particle size and inner diameter of the kiln, filling degree and the maximum repose angle. [49]

$$Fr = 8\,\frac{d}{D}\frac{1}{sin^2\,\epsilon}\left(0,35\,\beta - \frac{8,75\,\pi}{180}\right)^2 sin\beta \tag{21}$$

d/D... ratio of particle size and inner diameter of the kiln, ϵ... filling degree β... maximum repose angle

Froude-values < 1 suggest more of a gravity related and less of an inertial tranversal transportation method, which means that the bed moves through the furnace following a screw-shaped line at very small Froude-values ($0 > Fr > 10^{-4}$), without the particles within the bed rearranging themselves (gliding). Hence this is unwanted in industrial processes and can be counteracted by increasing the roughness of the inner kiln wall. Ideally, Froud-values should be $10^{-5} < Fr < 10^{-1}$, promoting transversal particle movement within the active layer. Periodic sliding of the active layer represents a state close to the unwanted, screw-shaped movement of the bed, whereas rolling presents the preferred transversal movement of the active layer in the middle of the mentioned Froud-value range and periodic cascading signifies the boundary towards the cascading, often seen in ball mills at the upper end of the continuum. If Froude-values exceed unity, the material sticks to the inner kiln wall, like in centrifuges, due to the dominant influence of the inertia of the particles. The transition from periodic gliding towards rolling in the active layer can be mathematically described, using an equilibrium of forces-method by the filling rate of the triangle ABC, displayed in figure 2.13. If this triangles cannot

discharge the material in time through periodic gliding, rolling sets in. This transitional criteria is mainly related to the particle size, however relatively indifferent to the filling degree of the kiln. The critical Froude-value diminishes if the inner kiln diameter increases, the inner kiln wall is less rough, the filling degree higher and/or the dumping angle of the material decreases. The rolling towards periodic cascading transition strongly depends on the filling degree of the kiln and sets in when the dynamic angle of repose approaches a critical value and a certain fraction of the bed reaches the upper half of the furnace during the rotation. Apart from the Froud-value, the transversal movement of the active layer depends on the rotation speed of the kiln, the friction coefficient of the inner kiln wall, the filling degree, the rheological properties of the particles (ratio particle size to kiln diameter) and the angle of repose. [48, 49]

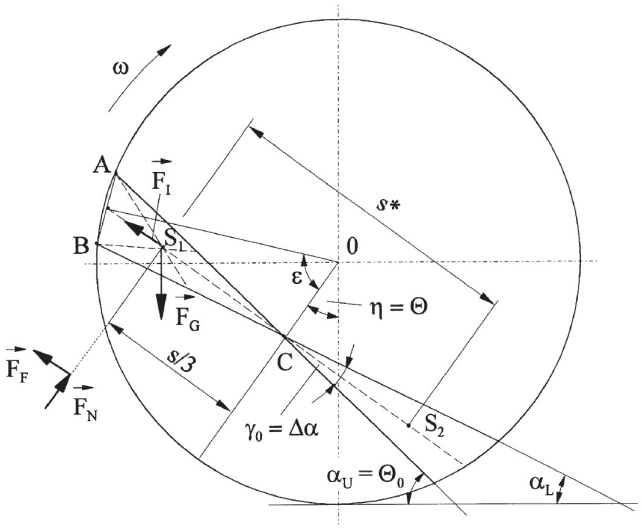

Figure 2.13: Criteria for the transition from periodic gliding towards rolling in the active layer

The inactive layer is much bigger than the active one, volume-wise. It follows a screw-shaped path through the kiln, much like a plug flow. Every particle from the inactive layer evententually reaches the active layer and reacts with the furnace atmosphere. The figure 2.14 displays some parameters, characterizing the behavior of the bed in rotary furnaces. [50, 51]

2.8 Transition of heat in a rotary kiln

There are three main heat transfer mechanisms [51]:

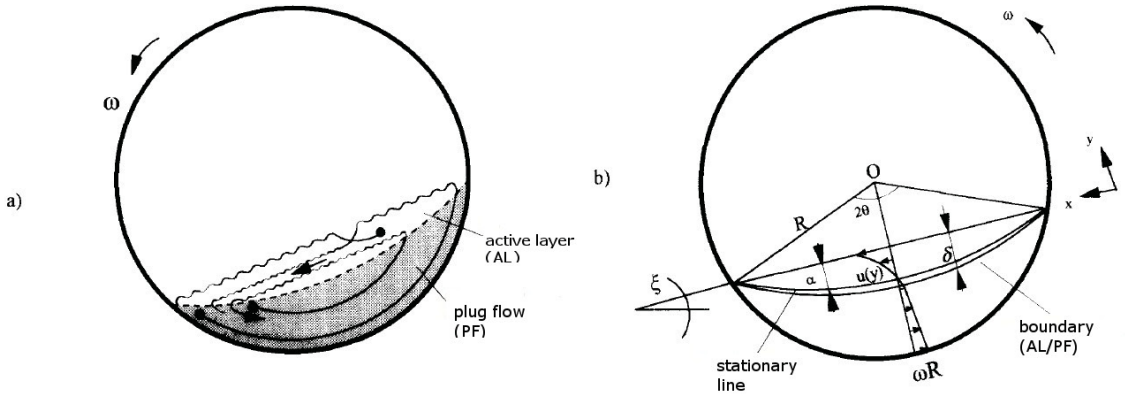

Figure 2.14: Display of a bed in a rotary kiln furnace; ω... angular velocity, Θ... repose angle, δ... thickness of the active layer, α... distance from the bed surface to the standstill line, u... velocity parallel to the bed surface, R... inner kiln diameter, ξ... inclination of the bed surface

- The heat conduction can be described by equation 22:

$$\dot{Q} = \frac{\lambda}{d} A \left(T_2 - T_1\right) \tag{22}$$

$\dot{Q}$... Heat flow, λ... heat conductivity, A... area, T... temperature, d... thickness

- Heat radiation can be mathematically derived from the Stefan-Boltzman-constant (equation 23):

$$\dot{Q} = \epsilon \, A \, \sigma \left(T_2^4 - T_1^4\right) \tag{23}$$

$\dot{Q}$... heat flow, ϵ... heat exchange coefficient, A... area, T... temperature, σ... Stefan-Boltzmann-constant

The heat exchange due to radiation can be calculated as follows (equation 24):

$$\epsilon = \frac{1}{\frac{1}{\epsilon_1} + \frac{1}{\epsilon_2} - 1} \tag{24}$$

- Convection: The heat transfer coefficient α can be obtained through the Nusselt-number. The heat flow can be calculated as follows (equation 25):

$$\dot{Q} = \alpha \; A \; (T_2 - T_1) \tag{25}$$

$\dot{Q}$... heat flow, α... heat transfer coefficient, A... area, T... temperature

In indirectly heated rotary kilns, the heat flow mainly takes place through conduction from the oven wall into the bed but also through heat transfer between the oven atmosphere and the bed as well as between the inner kiln wall and the oven atmosphere. [51].
The heat transfer within the bed occurs through conduction, if the particles are in contact with each other but also through the gas phase in between particles. Heat is transported through radiation between neighboring particles. The heat conduction in the gas phase diminishes drastically, when the distance between the particles proofs to be shorter than the mean free path of the gas molecules. Due to the spherical shape of most particles, the gap between them and hence the heat transportation increase quickly. However this does not apply to particles, close to the inner kiln wall. Experiments have shown, in accordance to the discussed theoretical considerations, that the heat transfer within the bed is much better than between the bed and the kiln wall, which results in a temperature drop close to the surface. Due to the steady mixing of the bed in the active layer the differences in temperature towards the oven atmosphere and the kiln wall can be ignored for industrial applications and a homogeneous temperature profile can be assumed within the bed. However segregation within the bed can still cause a temperature profile. [47]
The heat transport from the atmosphere towards the bed and the kiln wall is due the turbulent gas flow, the heat transfer is apart from the temperature also dependent on convection and radiation. Radiation represents the main heat transfer mechanism at temperatures exceeding 800 °C. Thermodynamically the convective heat transfer in a roatary kiln is similar to a sheet or a non circular pipe in a gas stream. [47]

When upscaling a rotary kiln, one needs to take into consideration, that the heat transfer is more and more limited with increasing size due to a relatively decreasing bed surface-area and mean residence time of the solids. This will be illustrated through the following equations. The equation 26 calculates the mass flow rate:

$$\dot{M} = 148 \; n \; \phi \; tan\alpha \; D^3 \tag{26}$$

$\dot{M}$... mass flow rate, ϕ... filling degree, n... rotation speed [U·min^{-1}], α... inclination of the kiln, D... kiln diameter

When doubling the length and the diameter of a kiln but not the filling degree, the exposed bed surface area is also doubled. However the mass flow rate becomes eight times as big as well as the ratio surface area to mass flow decreases. This consequently reduces the heat transmission which represents the limiting upscaling factor (equation 26).

Inhomogeneous material often causes problems in rotary kiln processes. Difficulties with different grain sizes can best be illustrated through the example of the cement industry. Over-calcination of small particles is to be avoided while the same process conditions must ensure the complete processing of larger particles as well. The active layer constantly renews itself, exposing new material available for heat transfer from the oven atmosphere. Due to the rotating motion of the kiln, a segregation between bigger and smaller particles occurs causing a temperature gradient within the bed. Smaller particles tend to accumulate in the center of the bed, which makes it less likely for them to reach the active layer, leading to limited processing of those particles. In the case of the cement industry this actually results in an overall positive effect leading to a more balanced processing of bigger and smaller particles.
The dominant heat transfer mechanism in indirectly heated rotary kilns from the inner kiln wall into the bed increases linearly with the increase off the mass flow rate. The rotation speed does not have a significant effect on this heat transfer mechanism. [50, 51]

2.9 Mean residence time of solids

The mean residence time of solids in rotary kilns primarily depends on the following parameters:

- Kiln size (length and diameter)
- Process parameters (mass flow, rotation speed and inclination of kiln)
- Material properties and filling degree
- Transportation aids within the kiln (discharge barrier)

Taking these parameters into account, equations for estimation of the mean residence time within the kiln were developed. The equation 27 is a simple approach to the calculation of the

mean residence time, not including the material input rate or transportation aids. The equation proves to be especially accurate (deviations between -10 % and +4 %) in combination with a low filling degree (< 10 %), which can be achieved through low material input and/or high rotation speed. [52]

$$MRT = 1,77 \, \frac{L}{D} \, \frac{\sqrt{\Theta}}{n \, \beta} \tag{27}$$

MRT... mean residence time L... length of kiln, D... diameter of kiln, Θ... inclination of the bed in motion, n... rotation speed, β... inclination of the kiln

Considering only the geometrical properties of the kiln, the mean residence time can be calculated as follows (equation 28):

$$t = \frac{L}{60 \, \pi \, D \, n \, tan\alpha} \qquad tan\alpha = \frac{h}{2 \, r \, \pi} \tag{28}$$

t... mean residence time, L... length of kiln, n... rotation speed [U·min^{-1}], α... inclination of kiln, h... axial motion of the bed per turn

The axial motion of the bed due to the different transversal movements of the active layer directly influences the mean residence time. Various equations were developed to estimate the mean residence time of the material within the kiln, taking the different transversal movements into account. The axial velocity of the material in the kiln, with the bed gliding through the furnace (no transversal motion) can be calculated through equation 29. [53]

$$v_s = \omega \, R_i \, \frac{sin\alpha}{sin\mu} \tag{29}$$

ω... rotation speed, R_i... inner radius of the kiln, α... inclination of kiln, μ... friction factor between bed and inner kiln surface

The parameters used to calculate the axial material velocity are displayed in figure 2.15. It expects particles within the passive layer to move through the kiln along an imaginary helical curve. As soon as a particle reaches the active layer the model assumes for it to slide over the bed surface, following an ideal slope line and hence achieving an axial distance of Δz.
The time the particle takes to slide over the bed surface is disregarded due to the very short time this takes in comparison with the duration the particle remains in the passive layer. Integration over all turning radiuses leads to equation 30. [54]

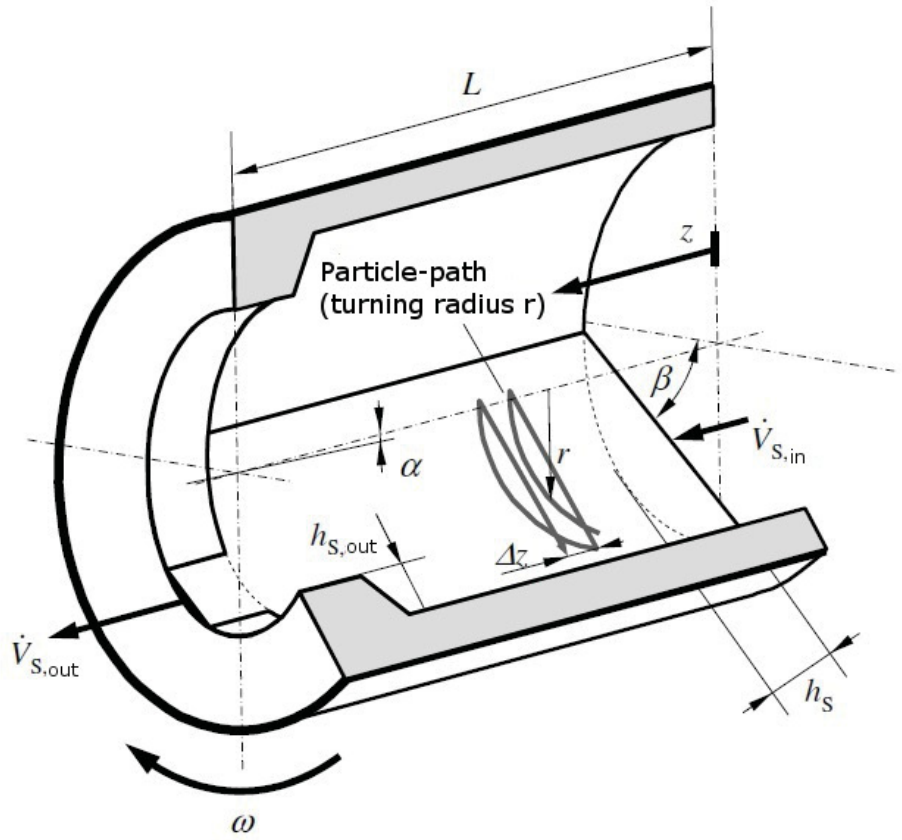

Figure 2.15: Rotary kiln with discharge barrier; z... axial coordinate, $\dot{V}_{S,in}$... input material flow rate, α... inclination of kiln, ω... rotation speed, $v_s(z)$... material velocity within the kiln, $h_{S,out}$... height of discharge barrier, β... dynamic angle of repose, L... length, $A_S(z)$... cross section of the bed, $h_S(z)$... depth of bed [54]

$$\dot{V}_S = A_s\, v_S = \frac{2}{3}\,\omega\, R_i^3 \left(\frac{tan\alpha}{sin\beta} - \frac{\delta h_S}{\delta z}\, cot\beta\right)\left(2\,\frac{h_S}{R_i} - \frac{h_S^2}{R_i^2}\right)^{\frac{3}{2}} \tag{30}$$

A_S... cross section of the bed, h_S... depth of bed, $\dot{V}_s$... material flow rate, ω... rotation speed, R_i... inner kiln radius, α... inclination of kiln, β... dynamic angle of repose

The simplifications in equation 31 highlight the fact, that the velocity of the material in the kiln mainly increases with higher rotation speed and inclination of the kiln and diminishes with increasing angle of repose and higher bed depth [55]. The lower bed velocity with increasing bed depth is actually a result of two contradicting processes. A higher bed depth will automatically lead to a greater distance each particle moves in axial direction when sliding over the bed

surface, which would imply a higher material velocity with increasing bed depths. However, higher bed depth also means a much longer period of time has to pass until one and the same particle reaches the active layer and can cover the distance in axial direction . This latter effect is dominant, which means that small bed depths lead to more frequent transversal motions of the particles and hence higher material velocity within the kiln. [54, 55]

$$\frac{A_S}{\pi\ R_i^2} \approx \frac{1}{2}\left(\frac{h_S}{R_i}\right)^{\frac{4}{3}} \qquad \left(2\frac{h_S}{R_i} - \frac{h_S^2}{R_i^2}\right)^{\frac{3}{2}} \approx 1,24\ \frac{h_S}{R_i}$$

$$v_S = 1,653\ \omega\ R_i^{\frac{4}{3}}\ h_S^{-\frac{1}{3}}\left(\frac{tan\alpha}{sin\beta} - \frac{\delta h_S}{\delta z}\ cot\beta\right) \tag{31}$$

A_S... cross section of the bed, h_S... depth of bed, $\dot{V}_s$... material flow rate, ω... rotation speed, R_i... kiln radius, α... inclination of kiln, β... dynamic angle of repose

2.9.1 Material flow conditions within the kiln

The Peclet number (equation 32) gives a good estimation of the material flow conditions within the kiln.

$$Pe = \frac{2\ \gamma^2}{\sigma^2} \tag{32}$$

γ... mean residence time, σ^2... empirical variance of mean residence time

A plug flow can be assumed if the Peclet number exceeds 100. A higher length to diameter ratio leads to increasing Peclet number values, which means, that the empirical distribution of the material residence time within the kiln approaches a narrower normal distribution. An empirical residence time distribution of zero would represent a perfect plug flow. The filling degree of the kiln does not have a high influence on the material flow conditions. Higher rotation speed and larger bed surface lead to a higher Peclet number value and hence an approximation towards an ideal plug flow of the material. [56]

2.9.2 Filling degree and rotation speed of the kiln

If the material flow remains constant the filling degree and the rotation speed are inversely linear connected. Also the homogeneity of the bed depth influences this interrelationship. The mean

residence time increases with growing filling degree at an homogeneous bed depth. However to calculate the mean residence time of the material assuming an inhomogeneous bed depth, the bed profile needs to be taken into account. The rotation speed has no influence on the bed-depth-profile but as mentioned before higher rotation speed decreases the mean residence time of the material. [56]

If the input material flow and the rotation speed of the kiln are summarized ($\frac{\dot{m}}{n}\ [kg]$) a linear connection with the amount of material present in the furnace at a given moment can be observed. The rotation speed has a much higher influence on the mean residence time than the material input rate hence a reduction of the rotation speed leads to a strong increase in the mean residence time of the material in the kiln. The higher the rotation speed, the less influence a change of the material input rate exerts on the mean residence time. [52]

2.9.3 Grain size of the material

Smaller grains generally lead to higher residence times than bigger ones [56]. The model discussed above [54] assumes an infinitely thin active layer and particles gliding on an ideal fall line over the bed surface. However, realistically the gliding particles within the active layer are sidetracked by other particles on their way down, leading to a transversal mixing of the bed. The deviation of the particles in their transversal movement also leads to an axial dispersion which is further promoted by large Froude numbers, small radius to length ratios, high filling degree and most of all inhomogeneous particle sizes. A variance in grain size or density also lead to a segregation of the bed due to smaller particles having a greater likelihood of coming across gaps on the bed surface while gliding down and consequently accumulating in the center of the bed. Saemans model predicts that particles in the center of the bed follow a path with a smaller turning radius and consequently exhibit less transversal motion than particles closer to the surface bed. Hence, smaller particles tend to have a higher mean residence time than bigger ones. [47]

3 Experiments

The following chapter will introduce a series of experiments in order to thoroughly characterize the materials in question and to lay the experimental groundwork for the introduction of an industrial scale recycling process.

3.1 Oxidation kinetics

These experiments were conducted in order to get insights regarding the conversion behavior of various refractory metal alloys under an oxidizing atmosphere over time. The experimental build up consisted of a tube furnace with a rotameter and a filter system (figure 3.1a) as well as a ceramic bin containing a piece of refractory material to hold the sample (figure 3.1b). A gravimetrical approach as described in section 2.5 was chosen to study the oxidation kinetics. The data necessary for the evaluation was collected with the help of a precision scale.

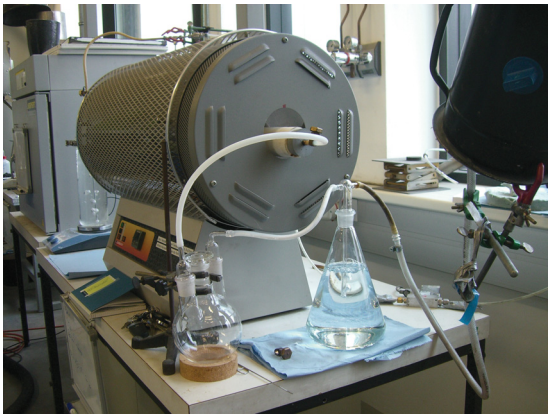

(a) Carbolite tube furnace with filter system

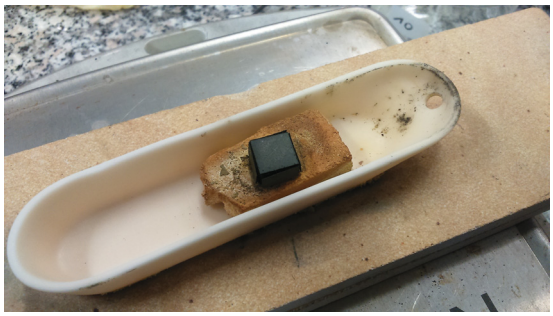

(b) Ceramic bin with refractory material and sample

Figure 3.1: Experimental setup for the determination of the oxidation kinetics

3.1.1 Oxidation kinetics of a molybdenum-tantalum alloy

The investigated material is a molybdenum-tantalum alloy with 10 wt-% tantalum according to the SEM/EDX analysis, displayed in table 3.3. Two sets of experiments were conducted with

different gas velocities. Weight and time were measured during the experiment, whereas the remaining parameters in table 3.4 resulted from the formulas introduced in section 2.5. The columns marked in yellow are used to plot the conversion of the sample over time, not taking into account the diffusion of oxygen through the product layer. The inclination of the linear smoothing function for the data points give the velocity constant for a set temperature. When the diffusion through the product layer is included the data marked blue in the table is plotted. The data plots are shown in the results chapter and the appendix. The tables 3.4 and 6.1-6.5 show the data gained from experiments conducted with a gas velocity of 10 l/min of air, whereas tables 6.6-6.10 refer to experiments run with a gas velocity of 1 l/min. The temperatures were chosen to be between 850 °C and 975 °C according to table 3.2.

The calculations were done, assuming 23.1 wt-% oxygen in air and an air-density according to table 3.1 [57]. The corresponding oxygen concentrations according to equation 33 are also listed in table 3.1.

$$n_i = \frac{m_i}{M_i}$$

$$1 \;\; kg \;\; air: \qquad n_{O_2} = \frac{231.32 \;\; g}{31.9988 \;\; [g/kmol]} = 7.22 \;\; mol \tag{33}$$

$$C = \frac{mol}{g} \cdot \rho_{air} \;\; [mol/cm^3]$$

Table 3.1: Air density at various temperatures and corresponding oxygen content

Temperature [°C]	Air density [g/cm^3]	Oxygen concentration [mol/cm^3]
975	0.2828	$2.0442 \cdot 10^{-6}$
950	0.2887	$2.0871 \cdot 10^{-6}$
925	0.2946	$2.1298 \cdot 10^{-6}$
900	0.3005	$2.1724 \cdot 10^{-6}$
875	0.3075	$2.2231 \cdot 10^{-6}$
850	0.3145	$2.2737 \cdot 10^{-6}$

Table 3.2: Process parameters for iso-thermal experiments on a Mo-Ta alloy

	Material	Temperature [°C]	Gas velocity [l/min]	Gas composition
ISO Mo-Ta 13	MoTa 11	975	10	21 % O_2, 79 % N_2
ISO Mo-Ta 1	MoTa 11	950	10	21 % O_2, 79 % N_2
ISO Mo-Ta 12	MoTa 11	925	10	21 % O_2, 79 % N_2
ISO Mo-Ta 2	MoTa 11	900	10	21 % O_2, 79 % N_2
ISO Mo-Ta 10	MoTa 11	875	10	21 % O_2, 79 % N_2
ISO Mo-Ta 3	MoTa 11	850	10	21 % O_2, 79 % N_2
ISO Mo-Ta 14	MoTa 11	975	1	21 % O_2, 79 % N_2
ISO Mo-Ta 5	MoTa 11	950	1	21 % O_2, 79 % N_2
ISO Mo-Ta 8	MoTa 11	925	1	21 % O_2, 79 % N_2
ISO Mo-Ta 4	MoTa 11	900	1	21 % O_2, 79 % N_2
ISO Mo-Ta 7	MoTa 11	875	1	21 % O_2, 79 % N_2
ISO Mo-Ta 6	MoTa 11	850	1	21 % O_2, 79 % N_2

Table 3.3: Composition of molybdenum-tantalum alloy

Element	wt.-%	at.-%
Mo	89.96	94.41
Ta	10.04	5.59

Table 3.4: Evaluated data from trial ISO Mo-Ta 1

Time [min]	Time [sec]	Weight [g]	R $(g_0 - g)/g_0$	W $Wo^{1/3} - W^{1/3}[g^{1/3}]$	$(2/g)^{2/3}Ct$ $[s \cdot cm^2 \cdot g^{-2/3}]$	$(2 \cdot C \cdot M \cdot t)/(\alpha \cdot \rho)$ [s]	$(0.5 - 1/3 \cdot R - 0.5 \cdot ((1-R)^{2/3})) \cdot a1^2$ $[cm^2]$
0	0	3.63	0.000	0.000	0.000	0.000	0.000
20	1200	3.35	0.077	0.041	80.975	0.016	0.034
40	2400	3.05	0.160	0.087	161.951	0.032	0.153
60	3600	2.76	0.240	0.134	242.926	0.048	0.359
85	5100	2.23	0.386	0.230	344.145	0.068	1.011
105	6300	1.79	0.507	0.323	425.120	0.084	1.896
125	7500	1.69	0.534	0.346	506.095	0.100	2.151
145	8700	1.56	0.570	0.377	587.071	0.116	2.518
165	9900	1.43	0.606	0.410	668.046	0.132	2.929
185	11100	1.11	0.694	0.501	749.021	0.148	4.165
205	12300	0.83	0.771	0.597	829.996	0.164	5.592
245	14700	0.57	0.843	0.759	991.947	0.196	7.348
265	15900	0.47	0.871	0.754	1,072.922	0.212	8.186
285	17100	0.48	0.868	0.754	1,153.897	0.228	8.097
305	18300	0.48	0.868	0.754	1,234.873	0.244	8.097

3.1.2 Oxidation of a tungsten-rhenium alloy

The tungsten-rhenium alloy used in the experiments described below, contains 25 weight percent rhenium, according to the SEM/EDX analysis displayed in table 3.5, whereas table 3.6 indicates the relation between process gas conditions and oxygen concentration. The process parameters were chosen according to table 3.7. The experiments were conducted within a temperature range of 850 °C to 950 °C and a process atmosphere of 10 l/min 90 % O_2 and 10 % N_2. The experimental setup and the calculations conducted were along the lines of those describes in the section above and can be seen in tables 6.12-6.16 in the appendix.

Table 3.5: Composition of tungsten-rhenium alloy

Element	wt.-%	at.-%
W	74.70	74.94
Re	25.30	25.06

Table 3.6: Oxygen concentration in the process gas according to the ideal gas equation

Temperature [°C]	Oxygen fraction in gas-stream [%]	Oxygen concentration [mol/cm^3]
1000	100	$9.5708 \cdot 10^{-6}$
950	100	$9.962 \cdot 10^{-6}$
950	90	$8.9658 \cdot 10^{-6}$
925	90	$9.15291 \cdot 10^{-6}$
900	90	$9.34803 \cdot 10^{-6}$
875	90	$9.55161 \cdot 10^{-6}$
850	100	$1.08491 \cdot 10^{-5}$
850	90	$9.76419 \cdot 10^{-6}$

Table 3.7: Process parameters for isothermal experiments on a W-Re 25 alloy

Experiment	Material	Temperature [°C]	Gas velocity [l/min]	Gas composition
ISO W-Re 7	W-Re 25	900	10	90 % O_2, 10 % N_2
ISO W-Re 8	W-Re 25	850	10	90 % O_2, 10 % N_2
ISO W-Re 9	W-Re 25	950	10	90 % O_2, 10 % N_2
ISO W-Re 10	W-Re 25	925	10	90 % O_2, 10 % N_2
ISO W-Re 11	W-Re 25	875	10	90 % O_2, 10 % N_2
ISO W-Re 4	W-Re 25	850	3	100 % O_2
ISO W-Re 5	W-Re 25	950	3	100 % O_2
ISO W-Re 6	W-Re 25	1000	3	100 % O_2

3.2 Pilot tests on different materials

After the characterization of the oxidation kinetics, the purpose of these pilot experiments was to gain experience on how well and under which conditions the alloys can be separated into their components. This represents a key aspect, since the purer the products are, the higher is the value of the future recycling product. The materials described below (table 3.8 and figure 3.2) were exposed to different process parameters in order to test the behavior of each of the alloy components in different atmospheres.

Table 3.8: Chemical composition of the materials used in the pilot tests

[wt.-%]	Mo	Ta	W	Re	Cu	Nb	O
Mo-W grains	varying		varying				
Mo 1-5 mm	100						
Mo chips	100						
Mo-Ta chips	89.72	10.28					
W-Re wire/grains			75.14	25.86			
W-Re chips			93.31	6.69			
Mo-W grains	50		50				
Mo-Nb grains	90					10	
Mo-Cu	82.94				17.06		

Table 3.9 lists all the pilot experiments conducted as well as the associated process parameters. Figure 3.3 shows the experimental setups for various experiments. The heated length of the furnace is 1 meter and the inner diameter of the pipes amounts to 5.5 cm. The gas stream

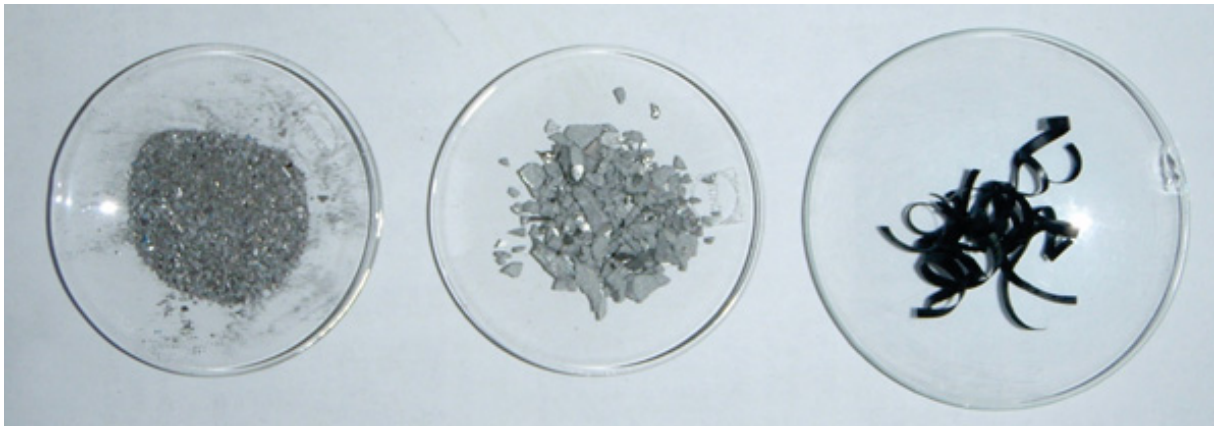

(a) Molybdenum < 1 mm; molybdenum 1-5 mm; molybdenum chips

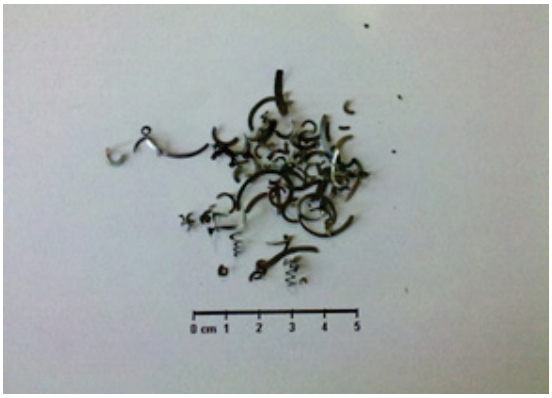

(b) Mo-Ta chips

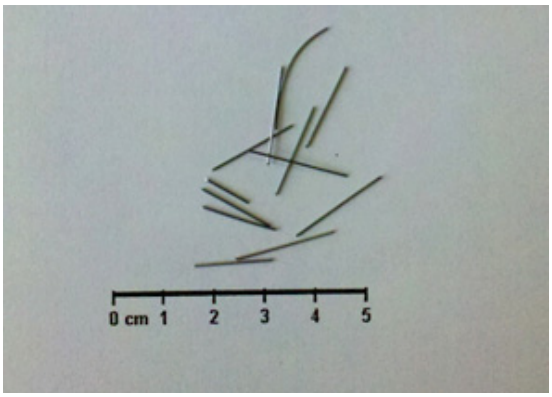

(c) W-Re wire

Figure 3.2: Some of the materials used in the pilot experiments

was controlled by a digital rotameter. The off gas flows through a filter bottle which was used as a gravitational separator and another bottle filled with water which served as a wet scrubber before the gas enters the ventilation system. The samples were weighted before and after the initial experiments in order to obtain an idea of the degree of conversion in addition to the REM-EDX analysis. The results of the weight change can also be seen in table 3.9. In later experiments only the purity of the products was analyzed, since the conversion behavior was already established. Experiments Mo-Ox 1 to Mo-Ox 7 were supposedly done on pure molybdenum, however the characterization of the residues showed, that is was actually a mixture of molybdenum and tungsten grains for experiments Mo-Ox 1-3 and a tungsten containing molybdenum alloy, where not even the EDX analysis of the material could detect the tungsten content in the first place, for experiments Mo-Ox 4-7 respectively. The poor degree of conversion of the suspected Mo grains in experiment Mo-Ox 1 under synthetic air despite

a temperature of 1000 °C lead to a reintroduction of the residue material into the furnace under the same process conditions (Mo-Ox 2). Mo-Ox 3 was conducted under Ar-O_2 80-20 vol.-% atmosphere and in a steel pipe (figure 3.3e and 3.3d). This provoked a weight gain of the sample, probably also due to oxidation of the steel pipe resulting in oxidic particles that fell into the crucible. Almost no MoO_3 was found in the pipe after cool down, but all the more iron oxide particles from the steel pipe. Experiments Mo-Ox 4-7 were done with molybdenum grains of 1-5 mm under synthetic air atmosphere, since the Ar-O_2 80-20 vol.-% process gas did not yield a good degree of conversion of the sample. A small amount of residue could be detected within the crucible after the experiment, which means the conversion of the molybdenum was not ideal. The EDX analysis showed that the residue was mostly tungsten trioxide, which remained in the crucible, since its vapor pressure does not increase significantly until temperatures exceed 1200 °C [34]. Due to the extensive oxidation of the steel pipe in experiment Mo-Ox 4, the experimental setup was changed to a ceramic pipe and condenser (figure 3.3b and 3.3c). A lower temperature of 900 °C enabled the evaluation of the influence of the temperature on the degree of conversion. This lead to a bigger reduction of sample weight than the one observed in the previous experiment, despite the reduced temperature. Also a blockage appeared in the pipe due to sublimed material was formed. The temperature was further reduced to 800 °C in experiment Mo-Ox 6 in order to investigate the conversion of Mo in oxidizing atmosphere at a lower temperature. The duration of exposure of the sample in the furnace was doubled from previously 4 hours to now 8 hours. These process parameters resulted in a weight reduction of the sample which is lower but comparable to the experiments conducted at higher temperatures. Due to the formation of a blockage yet again, experiment Mo-Ox 7 was conducted with an increased gas stream of 5 l/min. Sublimed material still condensed within the pipe outside the heating zone, however a small hole that matched the gas inlet in diameter remained free, due to the increased gas stream volume.

Table 3.9: Process parameters of pilot experiments

	Mo-Ox 1	Mo-Ox 2	Mo-Ox 3	Mo-Ox 4	Mo-Ox 5	Mo-Ox 6	Mo-Ox 7	W-Re-Ox 8	W-Re-Ox 9
Material									
Mo-W grains	X		X						
Mo 1–5 mm				X	X	X	X		
Residue prev. exp.		X							
W-Re								X	X
Process gas									
Air	X	X							
Ar-O_2			X						
Synth. air				X	X	X	X	X	X
Gas stream [l/min]			1	1	1	1	5	5	5
Furnace parameters									
Heating time [h]	4	4	4	4	4	4	4	1	1
Heating rate [°C/min]	4.1	4.1	4.1	4.1	3.6	3.2	3.6	8	8
Temperature [°C]	1.000	1.000	1.000	1.000	900	800	900	500	600
Weight									
Initial weight [g]	5.001	2.699	5.001	5.004	5.002	5.001	5.002	4.974	
Crucible [g]	8.884	8.884	6.670	8.836	8.827	9.712	8.575	8.388	
End weight [g]	11.583	11.512	14.261	9.740	9.169	10.647	9.159	13.268	
Sublimat [g]	2.302	0.070	-2.590	4.100	4.660	4.065	4.418		0.0941

	W-Re-Ox 10	Mo-Ta-Ox 11	W-Re-Ox 12	W-Re-Ox 13	Mo-Ta-Ox 14	Mo-HOx 15	Mo-HOx 16	Mo-Ta-Ox 17	Mo-Ta-Ox 18
Material									
Mo 1–5 mm						X	X		
W-Re wire	X		X	X					
Mo-Ta chips		X			X			X	X
Process gas									
Synth. air	X	X	X	X	X	X	X	X	X
Gas stream [l/min]	5	5	5	5	5	5	3	5	5
Temperature H_2O [°C]						60	60		
Furnace parameters									
Heating time [h]	2	2	2	2	2	2	2	2	2
Heating rate [°C/min]	8	8	8	8	8	8	8	8	8
Temperature [°C]	800	900	900	900	800	750	800	700	750
Weight									
Initial weight [g]	5.026	X	5.150	2.314	2.543	5.165	5.500	2.684	3.047
Crucible [g]	8.388	X	8.197	8.799	8.199	7.970	8.893	8.693	7.994
End weight [g]	X	X	12.966	10.393	9.316	13.237	11.159	12.544	12.410
Sublimat [g]	X	X	0.381	0.120	1.426	-0.103	3.234	-1.167	-1.369

	Mo-Cu-Ox 19	W-Re-Ox 20	W-Re-Ox 21	W-Re-Ox 22	Mo-Nb-Ox 23	Mo-W-Ox 24
Material						
Mo-Cu pieces	X					
W-Re chips		X	X			
W-Re wire/grains				X		
Mo-Nb grains					X	
Mo-W grains						X
Heating rate [°C/min]	8 20-721 °C 4 721-900 °C					
Temperature [°C]	900	900	850	900	900	850
Heating time [h]		6	6			
Process gas	synth. air	2h 80% O_2 20% N_2 4h 100% O_2	80% O_2 20% N_2	90% O_2 10% N_2	air	88% N_2 12% O_2
Gas stream [l/min]	5	5	5	5	5	5

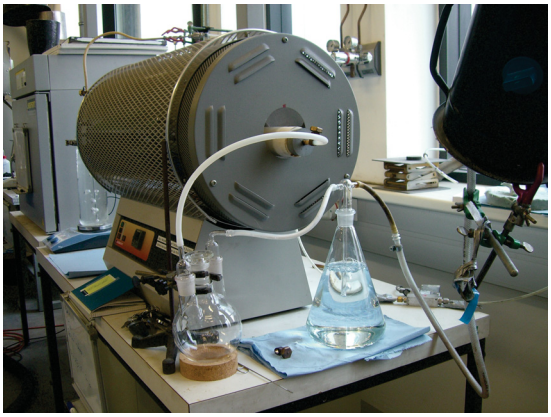

(a) Experimental setup for pilot experiments

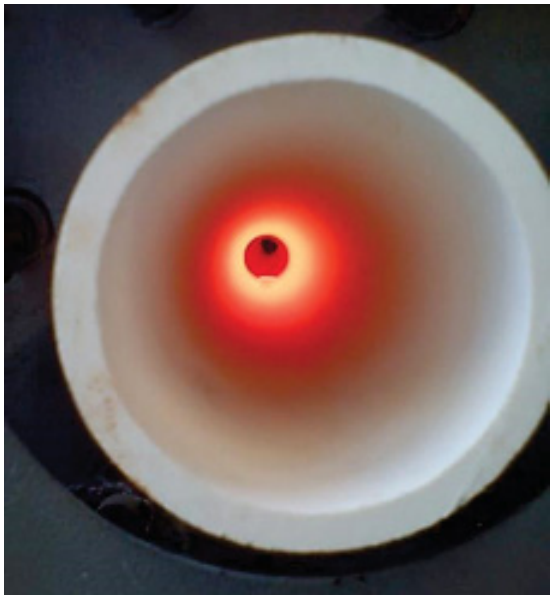

(b) Ceramic pipe

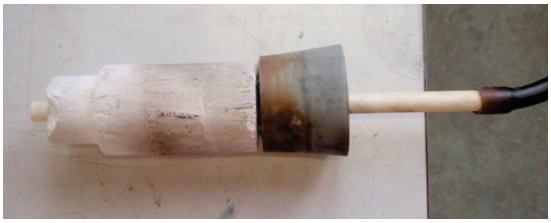

(c) Ceramic condenser

(d) Steel condenser

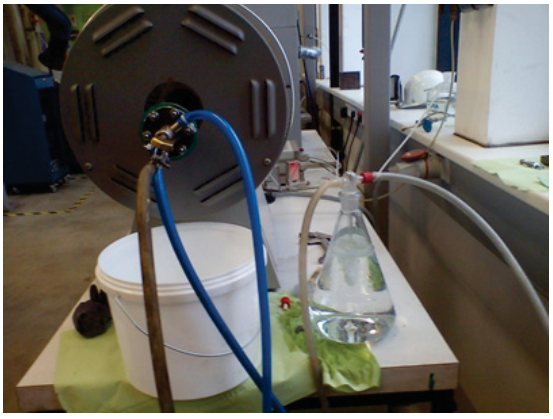

(e) Steel pipe

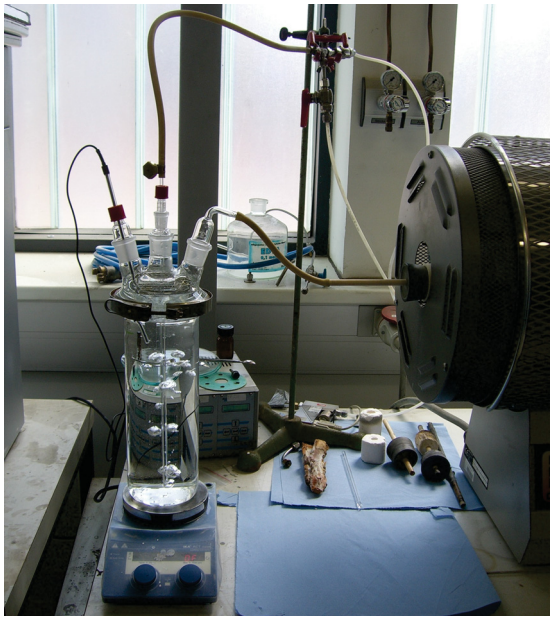

(f) Experimental setup for MoHOx experiments

Figure 3.3: Variations of experimental setup for the pilot experiments

To investigate the possibility to separate Mo-Ta alloy chips into their components through oxidation the following experiments were conducted. Investigation Mo-Ta Ox 11 was conducted at
900 °C in 5 l/min synthetic air. A complete conversion of the sample could be achieved. The following experiments were conducted to investigate the effect of reduced temperature on the degree of conversion and the impurity concentration in the products. The degree of conversion sank with decreasing temperatures in experiments Mo-Ta Ox 14 (800 °C), Mo-Ta Ox 17 and 18 with 700 °C and 750 °C respectively. In experiments Mo-HOx 15 and 16 the process gas flowed through a heated water bottle (60 °C) before entering the furnace, in order to add some humidity to the gas stream (figure 3.3f). The purpose of this was to investigate if the formation of molybdenum oxide hydroxides and their high vapor pressure could lead to lower process temperatures. Very little conversion took place in experiment Mo-HOx 15, that had a target temperature of 750 °C. An increase of 50 °C however lead to a much better degree of conversion of the sample. Also a liquid phase appeared in the crucible that solidified in a glass like manner upon cool down.

The experiments conducted on W-Re-wire with the chemical composition displayed in table 3.8 were initially performed at 500 °C (W-Re Ox 8) in synthetic air due to the postulated low sublimation point of 363 °C for rheniumheptoxide [34]. However no visible conversion of the material could be detected at the end of the experiment. The wire pieces were reintroduced into the furnace and the temperature increased to 600 °C (W-Re Ox 9) but again no conversion took place and only a very small weight gain of the sample could be measured. For experiment W-Re Ox 10 the temperature was increased to 800 °C. The filter bottle contained some blue Re-oxide sublimate and the wire seemed to be converted to a degree. To further increase the transformation rate, the next trials applied 900 °C. With these process parameters and an exposure time of the sample of 8 h the wire sample seemed to be fully converted after this experiment. During the first attempt (W-Re Ox 12) there was a power blackout, which is why the experiment was repeated with identical parameters (W-Re Ox 13). Experiments W-Re Ox 20 and 21 treated W-Re chips, which contain less rhenium. The temperature was set to 900 °C again but the oxygen content in the gas stream was increased to 80 vol.-% during the first two hours and 100 vol.-% during the last 4 hours of experiment W-Re Ox 20. No sublimate could be detected after the experiment, however the sample seemed to be fully converted.

Experiment W-Re Ox 21 proceeded with a lower temperature of 850 °C and 80 vol.-% oxygen in the gas stream. No sublimate condensed in the filter bottle, which is why this experiment was not repeated, despite the fact that the crucible broke at the end of the experiment and no sample could be collected. In order to get a significant amount of sublimate to enable a high quality analysis on impurities, experiment W-Re Ox 22 took place with W-Re grains, containing a higher amount of rhenium (table 3.8) and 90 vol.-% oxygen in the gas stream, which led to a complete conversion of the sample as well as a sufficient amount of sublimate for analysis in the filter bottle.

Further pilot experiments were conducted on Mo-Cu, Mo-Nb and Mo-W alloys. The oxidation of a Mo-Cu alloy (Mo-Cu Ox 19) resulted in a liquid phase due to the formation of a low melting eutectic. Hence no separation of the components was feasible. Therefore a different approach was chosen in this case (see next chapter). The material Mo-Nb (Mo-Nb Ox 23) was oxidized in 900 °C synthetic air in order to investigate the possibility to separate the alloy into its components with as little impurities as possible in each fraction. Experiment Mo-W Ox 24 on a W-Mo alloy was conducted for the same purpose under a process atmosphere with 12 vol.-% oxygen at 900 °C.

Separation of a Mo-Cu composite

This section describes the attempt to split a Mo-Cu composite and make the fractions available for re-use. The material is displayed in figure 3.4, its composition can be seen in table 3.8.
Due to the fact that a separation through oxidation did not succeed (Mo-Cu Ox 19), a different approach had to be chosen. The material was cut into chips and put into a tube furnace together with zinc at a weight ratio 1:10. Figure 3.5 displays the Cu-Zn phase diagram which represents the basis of this experiment to dissolve the copper, present in the compound into the zinc. The process parameters of the experiments conducted in the tube furnace can be seen in table 3.10.
Experiment Mo-Cu 1 was conducted under synthetic air which caused the formation of a thick oxidic layer, leaving only a small amount of liquid zinc available for copper dissolution in the crucible. Therefore experiment Mo-Cu 2 applied a crucible covered with a graphite plate. This however lead to an entirely reducing atmosphere within the crucible inducing the evaporation of metallic zinc, which oxidized in the furnace and was carried to the filter, once again leaving no

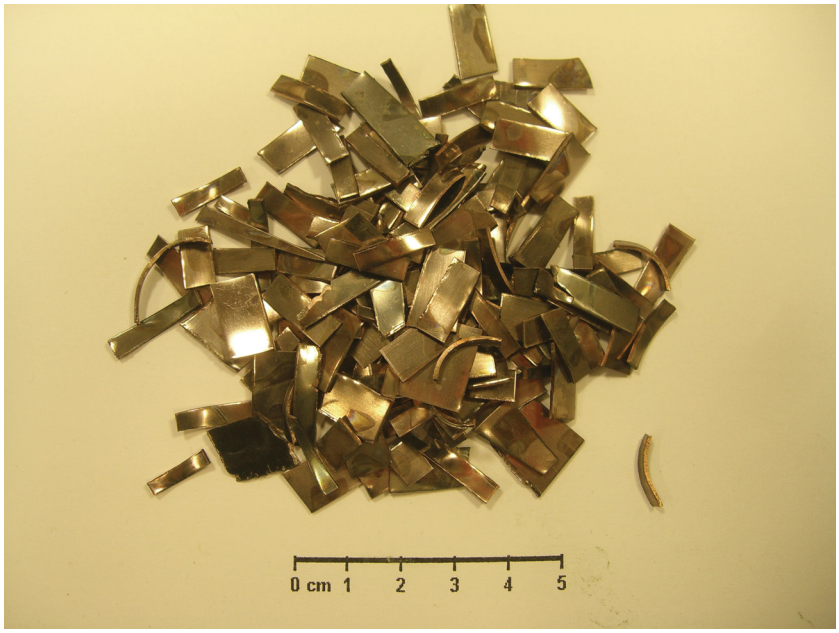

Figure 3.4: Mo-Cu composite

zinc in the crucible for the copper to dissolve in. Experiment Mo-Cu 3 used a reduced gas flow so an initially formed protective zinc oxide layer protected the rest of the zinc from oxidizing. To avoid excessive oxidation of zinc the experiment Mo-Cu 4 took place with nitrogen as an inert process gas during the heating phase to prevent oxidation of the Mo-Cu chips before the zinc has molten.

After the cooling of the materials the chips were mechanically extracted from the zinc matrix and introduced into a vacuum furnace (figure 3.6) in order to evaporate the zinc and copper and leave the molybdenum chips. The process parameters for the vacuum distillation experiments are displayed in table 3.11.

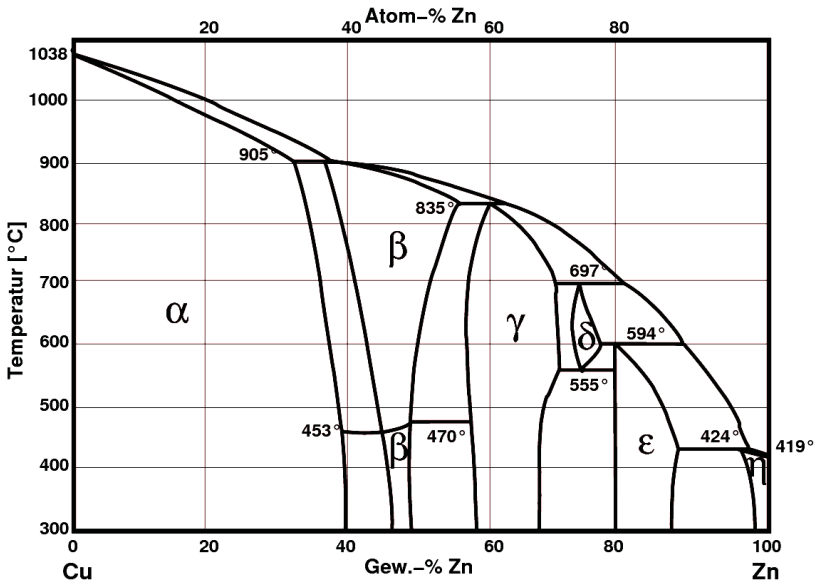

Figure 3.5: Binary phase diagram of Cu-Zn [58]

Table 3.10: Process parameters of Mo-Cu chips in liquid zinc

	Mo-Cu 1	Mo-Cu 2	Mo-Cu 3	Mo-Cu 4
Weight Mo-Cu [g]	19.4	20	5.4	5.4
Weight Zn [g]	194	200	54	54
Process gas	Synth. air	Synth. air + graphite	Synth. air	Nitrogen
Temperature [° C]	700	650	650	25-500
Time [min]	240	240	240	60
Gas velocity [l/min]	5	5	1	5
Process gas				Synth. air
Temperature [° C]				650
Time [min]				180
Gas velocity [l/min]				5
Heating time [min]				

Table 3.11: Process parameters of vacuum distillation

	Mo-Cu 1	Mo-Cu 3	Mo-Cu 4
Temperature [° C]	550-600	650	650
Time [min]	300	300	240
Pressure [bar]	$3 \cdot 10^{-2}$	$8 \cdot 10^{-2}$	$8 \cdot 10^{-3}$

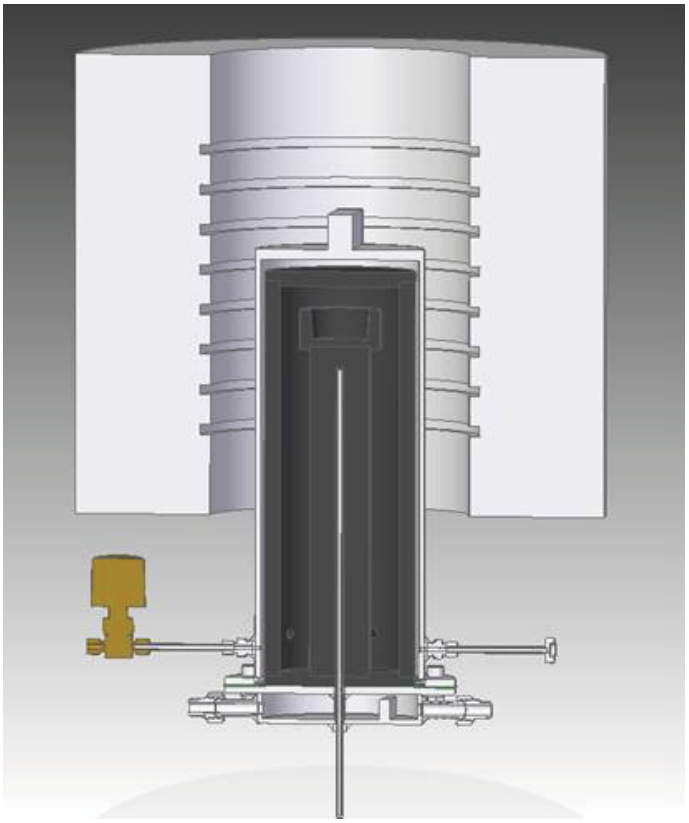

Figure 3.6: Vacuumdestillation furnace to remove zinc

3.3 Optimization of process parameters

In order to investigate the optimal process parameters for the treatment of Mo-Ta 10 samples concerning oxidation time for a conversion degree of 30 wt.-% as well as the residual MoO_3 in the Ta oxide fraction after fully oxidizing the sample, the following experiments took place. Table 3.12 lists the variations for each factor. The charge within the tube furnace comprised 20 g of sample material for each experiment at 10 l/min gas flow, according to a statistical design of experiments (DoE) done with MODDE 7. The samples were weighed and photographed every 20 minutes and thereafter recharged into the furnace. The tantalum fraction was analyzed with SEM-EDX after the experiment in order to determine the residual Mo content within the sample. The experiment ended when two consecutive weight measurements did not differ. The stoichiometrically calculated weight of the sample is 2.4 g when it is fully oxidized and all of the MoO_3 evaporated. Due to the fact that the reaction speed slows down considerably towards the end of the experiments (see figure 6.1), introducing new influence factors on the oxidation time, the statistical analysis of the oxidation time only considered the data for samples when they weighed > 6 g. The factors were varied according to table 3.12.

Table 3.12: Range of varied process parameters

Temperature [°C]	Grain size [mm]	Oxygen content [vol-%]
850	< 1	12
875	1-2	21
900	2-4	35
925	4-6.3	60
950	> 6.3	

Table 3.12 lists the vatiations of each factor, table 3.13 displays the experimental design for optimizing the oxidation time of a Mo-Ta 10 alloy, whereas table 3.14 introduces the process parameters for improving the residual molybdenum content within the tantalum oxide fraction.

Table 3.13: Experimental design for optimizing the oxidation time in a Mo-Ta 10 alloy

Grain size [mm]	Oxygen content [vol.-%]	Temperature [C]	Oxidation time [min]
> 6.3	12	850	272
1-2	35	850	157
> 6.3	35	850	225
> 6.3	12	950	150
> 6.3	35	950	47
2-4	21	925	74
4-6.3	21	925	157
2-4	12	900	100
2-4	21	900	82
1-2	21	900	50
< 1	35	900	90
2-4	12	875	125
1-2	35	875	58
2-4	21	900	120
2-4	60	950	134
2-4	60	900	222
> 6.3	60	900	216
4-6.3	60	850	380
> 6.2-4	60	950	113

Table 3.14: Experimental design for optimizing the residual MoO_3 content within the tantalum oxide fraction

Grain size [mm]	Oxygen content [vol.-%]	Temperature [°C]	Residual MoO_3 [wt.-%]
> 6.3	12	850	10.9
1-2	35	850	29.5
> 6.3	35	850	34.3
> 6.3	12	950	4.1
> 6.3	35	950	4.4
1-2	12	925	4.8
2-4	21	925	8
4-6.3	21	925	15.3
> 6.3	12	925	26.5
4-6.3	35	850	31.5
2-4	12	900	5.4
2-4	21	900	5.3
1-2	21	900	4.9
< 1	35	900	20.6
2-4	12	875	9.7
1-2	35	875	19.4
4-6.3	12	900	5.5
2-4	60	850	31
2-4	60	950	17.4
4-6.3	60	900	29.8
2-4	60	900	30.9
> 6.3	60	900	29
4-6.3	60	850	32.7

3.4 Experiments in a laboratory size rotary kiln

The materials processed in the laboratory size rotary kiln (figure 3.8), which has a heated length of 100 cm and an inner diameter of 10 cm are shown in table 3.15 and figure 3.7 whereas the most important process parameters of the experiments are listed in table 3.16.

Table 3.15: Chemical composition of materials used in the rotary kiln experiments

[wt.-%]	Mo	Ti	W	Re	Ta	O
Mo-Ti chips	99.51	0.49				
W-Re chips			93.31	6.69		
Mo-Ta chips	89.72				10.28	
Mo-W pellets	28.3		48.1			23.3

	Material	Heating rate [°C/h]	Time tt [h]	Parts [g]	Number	Sample weigt [g]	Temperature [°C]	$\dot{V}$ [l/min]	Gas	n [min-1]	α [°]	Theoret. res. time [min]
D-Mo 1	Mo 1-5 mm	400	1 h	50	5	257.5	900	3.4	Synth. air	6.45	1.4	22
D-Mo 2	Mo 1-5 mm	400	4 h	20	5	100	900	3.4	Synth. air	2.6	0.45	240
D-Mo 3	Mo 1-5 mm	400	4 h	20	5	106.17	900	3.4	synth. air	2.6	0.45	240
D-Mo-Ta 4	Mo-Ta	400	4 h	50	5	250	900	31.66	Synth. air	2.6	0.45	240
D-Mo-Ta 5	Mo-Ta	400	4 h	1x160; 3x50	4	310	900	31.66	Synth. air	2,6	0,45	240
D-Mo-Ti 6	Mo-Ti	300	4 h	50	5	250	900	31.66	Synth. air	2.6	0.45	240
D-Mo-Ta 7	Mo-Ta	400	4 h	50	5	251.71	900	17.82	Enr. air	2.6	0.45	240
D-Mo-Ti 8	Mo-Ti	400	4 h	50	5	250	900	32	Enr. air	2.6	0.45	240
D-Mo-Ta 9	Mo-Ta	400	4 h	25	10	250	900	32	Enr. air	2.6	0.45	240
D-Mo-Ta 10	Mo-Ta	400	4 h	20	12	240	900	50	Synth. air	2.6	0.45	240
D-Mo-Ta 11	Mo-Ta	200	3 h	20	10	200	900	50	Synth. air	2.6	0.45	240
D-Mo-Ta 12	Residue from D-Mo-Ta 11	400	4 h	ca. 20	1	ca. 20	900	50	Synth. air	2.6	0.45	240
D-Mo-Ta 13	Mo-Ta	400	3 h	5	40	200	900	50	Synth. air	2.6	0.45	240
D-W-Re 14	W-Re	400	4 h	5	40	200	900	50/40	Synth. air	2.6	0.45	240
D-Mo-Ta 15	Mo-Ta	400	4.5h	5	48	240	900	50	15% O_2 85% N_2	2.6	0.45	240
D-Mo-Ta 16	Mo-Ta	400	5 h	5	48	240	900	50	12% O_2 88% N_2	2.6	0.45	240
D-Mo-Ti 17	Mo-W	300	5 h	5	48	240	900	30	Synth. air	2.6	0.45	240
D-Mo-Ti 18	Mo-W	400	4 h	5	20	100	900	30	15% O_2 85% N_2	2.6	0.45	240
D-W-Re 19	W-Re	400	4 h	2	25	50	900	30	100% O_2	2.6	0.45	240
D-W-Re 20	W-Re	400	4 h	80	25	1860	900	20	80% O_2 20% N_2	2.6	0.45	240
D-W-Re 21	W-Re	400	4 h	80	25	1423	900	20	90% O_2 10% N_2	2.6	0.45	240

Table 3.16: Process parameters of experiments in the laboratory rotary kiln

time tt... time at target temperature, $\dot{V}$ ... gas flow rate, n... rotations per minute, theoret. res. time... theoretical residence time according to equation 35

(a) W-Re-chips

(b) Mo-Ti-chips

(c) Mo-Ta-chips

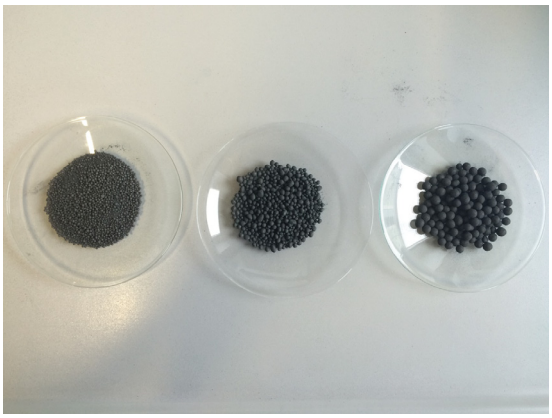

(d) Mo-W pellets

Figure 3.7: Sample materials for the experiments with the rotary kiln

The sample material is weighted and parted in order to simulate a continuous process through feeding the sample in small parts over a set amount of time. The amount of available oxygen can be adjusted through the gas flow rate as well as by changing the oxygen content in the process gas. The theoretical residence time of the material in the kiln can be calculated through considering the rotation speed, the inclination of the kiln and the inner diameter of the pipe according to equations 34 and 35. The actual residence time can hence be adjusted through regulating the rotation speed and the inclination of the kiln. The determination of the theoretical movement of the passive layer in axial direction per full rotation can be done according to the following equation:

$$x = tan\alpha \cdot D \cdot \pi \tag{34}$$

x... Theoretical axial movement per full rotation, α... inclination, D... inner diameter of the kiln

Figure 3.8: Laboratory rotary kiln

The theoretical residence time of the material in the kiln can be deducted through the following equation:

$$t = (L/x)/U \tag{35}$$

t... residence time, L... length of kiln, U... rotation speed [min^{-1}]

The following section will describe the experiments displayed in table 3.16. All experiments were done with a counter current gas flow at 900 °C, since that temperature proved to work best in the pilot experiments. If not otherwise mentioned, the process gas used consisted of synthetic air. The sublimed material, which was conveyed into the filter bottle with the gas stream was always collected and analyzed after the experiments as well as the samples retrieved from the kiln and the drop tank. The results of these analysis can be seen in section

4.20. Experiments D-Mo 1, D-Mo 2 and D-Mo 3 were conducted with molybdenum grains of 1-5 mm, containing tungsten impurities. These trials primarily served to study the behavior of the material in the bigger furnace compared to the one used in the pilot experiments as well as to understand the specifics of the furnace itself. The test D-Mo 1 showed considerable sublimation of the approx. 250 g of material charged into the furnace during the experiment, however also unreacted grains were found in the drop tank at the end of the kiln after the experiment. Furthermore a nose of resublimed material was formed along the inner circumference of the kiln at the end of the heating zone (figure 6.22a in the appendix). In order to increase the degree of conversion of the material the inclination of the kiln was decreased as well as the rotation speed. To test the new furnace configuration only 100 g of material were charged for experiment D-Mo 2. During that trial resublimed MoO_3 formed a thick blockage within the kiln at the end of the heating zone in gas flow direction (figure 6.22b and 6.22c) in the appendix). Furthermore the pipe broke due to thermal shock also at the end of the heating zone (figures 6.22b and 6.22c in the appendix). No material reached the drop tank. Therefore, D-Mo 3 was conducted in order to repeat the previous experiment so no parameters were changed. Again a blockage of resublimed material could be found in the pipe, as well an empty drop tank. So quite similar results could be found, which means that the pipe probably broke late in the experiment D-Mo 2.

In order to decrease the blockages in the pipe the gas flow rate was increased approx. 10-fold compared to the previous experiments (from 3.4 to 31.66 l/min). 250 g of Mo-Ta chips (chemical composition see table 3.15) were charged into kiln for experiment D-Mo-Ta 4. When looking at the bed within the kiln while charging, periodic cascading of the material could be observed (according to figure 2.12). No blockage of the pipe could be seen, however after cooling down the furnace a big quantity of chips stuck in the charging device (approx. 160 g), which means only a small amount of feed reached the inside of the furnace. Little material was found in the drop tank, however the chips inside the kiln were only partly converted and also sintered together (figure 6.22d in the appendix). Due to the failure of the charging device in this experiment it was repeated with identical parameters (D-Mo-Ta 5) and a total charge of 250 g Mo-Ta chips. A big amount of chips (160 g) was fed in the beginning in order to test the charging device and check for blockages and stuck chips. The rest of the chips was charged in two portions of 50 g each. After the experiment no blockage of the pipe could be detected. Some chips were transported back against the material flow direction towards the

feed entrance. The drop tank contained sublimate that was not conveyed out of the kiln with the gas stream as well as partly converted chips. For the experiment D-Mo-Ta 7 enriched air with 34 vol.% O_2 was used to enhance the degree of conversion of the chips. A reduced flow rate simultaneously served to test the new process parameter configuration. The bed in this experiment glided through the kiln - no transversal movement could be detected. A blockage of the pipe formed by resublimed material at the end of the heating zone, which was mechanically removed after 3 hours. The blockage presented itself with a round hole in the middle which matched the gas inlet in diameter. Also at the beginning of the heating zone in gas flow direction, a very thin re-sublimate film was formed, most likely during cool-down of the furnace, which collapsed when opening the kiln. Some material reverted against the material flow direction and out of the heating zone and was hence not fully converted. Experiment D-Mo-Ta 9 once again applied a gas flow rate of 32 l/min, and the enrichment of the process gas with oxygen was reduced to 24 vol.-% because the enrichment of the air in experiment D-Mo-Ta 7 combined with reduction of the gas flow rate seemed to promote the formation of a blockage in the pipe. During the investigation D-Mo-Ta 9 the formed noses in the pipe were regularly removed in order to avoid the formation of a blockage. However during the last period of the experiment a blockage formed yet again, only leaving open a small hole in the axial direction of the gas inlet (figure 6.22f). Some chips were reverted to the material inlet and therefore not entirely converted. The drop tank contained sintered chips as displayed in figure 6.22e in the appendix. For the investigation D-Mo-Ta 10, the charged sample of 240 g Mo-Ta chips was split into 12 parts in order to reduce the height of the bed and hence reduce the tendency of chips sintering together and limiting their conversion due to lack of exposure to the furnace atmosphere as could be seen in the previous experiment. Also no additional oxygen was added to the synthetic air and the gas-flow-rate further increased to 50 l/min to prevent the formation of a blockage, which indeed did not form. The drop tank however contained sintered chips. No parameters were changed for the experiment D-Mo-Ta 11, which was used to do a video analysis of the bed within the kiln. Halfway through the experiment the gas flow stopped, which lead to a quick formation of a blockage in the pipe. The drop container contained big sintered pieces. Those pieces were ground and reintroduced into the furnace in experiment D-Mo-Ta 12 in order to investigate if the sintered material can be further converted if ground and introduced to a second oxidation stage. No material could be found in the drop tank after the experiment, so an almost complete conversion of the material is likely. Despite the low amount of material

and the high gas flow rate a small nose of resublimed material was formed along the inner diameter of the kiln at the end of the heating zone in the direction of the gas flow. To investigate the possibilities to avoid a sintering of the chips in the kiln and a low degree of conversion, experiment D-Mo-Ta 13 was done. The 200 g of material charged for this experiment were split into 40 parts, further reducing the bed height and therefore the possibility of sintering due to a decreased amount of contact area among the chips. Once again a nose emerged inside the kiln leading to a reverse transportation and hence a diminished conversion degree of the material, because the chips could not pass the nose and enter the heating zone. The drop container showed smaller sintered pieces compared to the previous experiments. To study the effect of a reduced oxygen content in the oven atmosphere, experiments D-Mo-Ta 15 and 16 were done. D-Mo -Ta 15 was conducted with 15 vol-% O_2 in the process gas as well as 50 l/min gas flow rate. A blockage was formed during the cooling phase of the kiln. At the end of the experiment the residues were weighted which resulted in 32 g for the blockage material, 10.04 g in the drop container, 65 g of reverted material, 49.5 g of sublimate in the filter and 43 g of material in the feed area. For experiment D-Mo-Ta 16 a further reduction of the O_2 content to 12 vol.-% took place. The formed blockage had to be removed twice throughout the experiment. No material entered the drop container during the experiment and the kiln was nearly empty, which suggest a high degree of conversion of the material.

For the experiment D-Mo-Ti 6 chips with the chemical composition displayed in table 3.15 were put into the kiln. Due to a failure in the rotameter system, the gas flow rate of 31.66 l/min synthetic air could be turned on only the first hour of the experiment, which resulted in the formation of a blockage and a limited conversion degree of the material. D-Mo-Ti 8 was conducted with oxygen-enriched air of 34 vol.% O_2, which lead to a quick formation of a kiln blockage, leading to a very poor degree of conversion of the charged material, since the majority of the chips could not pass the blockage and did not enter the heating zone. The drop tank contained small sintered particles. Due to the continuing problems with blockages in the kiln in experiment D-Mo-Ti 17, the amount of charged material was reduced from 250 g as in the previous experiments to 100 g, while also going back to using synthetic air in experiment D-Mo-Ti 18. The formed blockage in the kiln during investigation D-Mo-Ti 17 was not stable and most likely did not prevent any chips from entering the heating zone. The drop container showed some sintered particles. The experiment D-Mo-Ti 18 with only 15 vol.% O_2 in the process gas

and a reduced material feed of 100 g only showed a nose along the inner diameter of the kiln at the end of the heating zone in the direction of the gas flow.

Experiment D-W-Re 14 was conducted with tungsten-rhenium chips with the chemical composition displayed in table 3.15. 200 g of chips were charged into the furnace in small portions of 5 g each. However the chips did not form a bed but stuck to the kiln wall. The temperature in this experiment dropped to 670 °C after two hours due to a power problem and also the gas flow rate had to be reduced from 50 l/min to 40 l/min. A dark blue layer accumulated inside the pipe and the filter system. The chips did not seem to have experienced a high degree of conversion after the experiment. Due to the experience gathered in the pilot test the trial D-W-Re was conducted with 100 vol.-% O_2 as process gas. The very exothermic oxidation of the chips induced a great thermal shock which destroyed the pipe. Hence experiment D-W-Re 20 was conducted with only 80 vol.-% O_2 in the process gas. 1860 g of chips were charged into the furnace in order to collect enough sublimate sample to perform a high quality analysis. Due to the exothermic reaction the temperature of the kiln rose to 1067 °C. A visual inspection of the chips after the experiment showed a good degree of conversion. Similar results could be achieved, by experiment D-W-Re 21 with 90 vol.-% O_2 in the process gas.

In order to recycle a molybdenum and tungsten containing abrasive slurry, pellets were produced on a pelletizing plate, using water with 10-40 wt.-% molasses as binder [59,60]. The pelletizing experiments of the slurry are described in a bachelor thesis [61]. All experiments operated at 900 °C and 15 vol.-% O_2 in the process gas. These parameters resulted from the experiences drawn from the pilot experiments also described in [61]. Table 3.17 shows the conducted experiments on pellets varying in grain-size and molasses content of the binder and the associated process parameters.

Table 3.17: Process parameters for converting pellets in rotary kiln

	O_2 [l/min]	N_2 [l/min]	Grain size [mm]	Weight [g]	Melasses in binder [wt-%]	Portions [g]
D-Mo-W P1	4.5	25.5	4-6.3 mm	267	10	26
D-Mo-W P2	4.5	25.5	2-4	184.6	10	18
D-Mo-W P3	4.5	25.5	2-4	284.6	15	28
D-Mo-W P4	4.5	25.5	4-6.3 mm	242.92	15	15
D-Mo-W P5	4.5	25.5	> 2	182.16	15	10
D-Mo-W P6	4.5	25.5	< 6.3	250.1	15	10
D-Mo-W P7	4.5	25.5	> 2	172.46	10	10
D-Mo-W P8	4.5	25.5	< 6.3	514.26	40	/

3.5 Upscaling-experiments in a industrial size rotary kiln

Two industrial sized experiments were conducted on the basis of the experiences draw from the previous investigations on Mo-Ta 10 chips. The first experiment (IBU 1) was conducted on an indirectly heated rotary kiln. The furnace specifications can be seen in table 3.18. As displayed in figure 3.9 the experiment was done in a counter current setup with a filter system and a charging device. The initial process parameters can be deducted from table 3.19. The upscaling of the gas stream was done through taking the increased diameter and cross section of the kiln into account. The start occuredwith an oxygen content of 12 vol.-% in the process gas to prevent the formation of a blockage and maximize the output.

Table 3.18: Specific facts to the rotary kilns used in the industrial size experiments IBU 1 and IBU 2

Parameter	Kiln for experiment IBU 1	Kiln for experiment IBU 2
Inner kiln diameter	0.4 m	0.3 m
Length, heated length	5 m, 3 m	7.4 m
Heating	Indirect electricity	Direct natural gas burner
Temperature range	150-1200 °C	150-1550 °C
Inclination	0.25 °	1.5 °
Rotation speed	3 min^{-1}	3 min^{-1}
Mass flow rate	10-100 kg/h	10-100 kg/h

Table 3.19: Initial process parameters for industrial sized experiments

Parameter	Experiment IBU 1	Experiment IBU 2
Temperature	Zone 1 1000 °C Zone2-3 900 °C	900-1200 °C
Theoretical residence time	7 h	7 h
Process gas	12 vol.-% oxygen	0-12 vol.-% oxygen
Gas flow rate	220 l/min air 150 l/min N_2	to be tested
Material flow rate	10 kg/h	10 kg/h

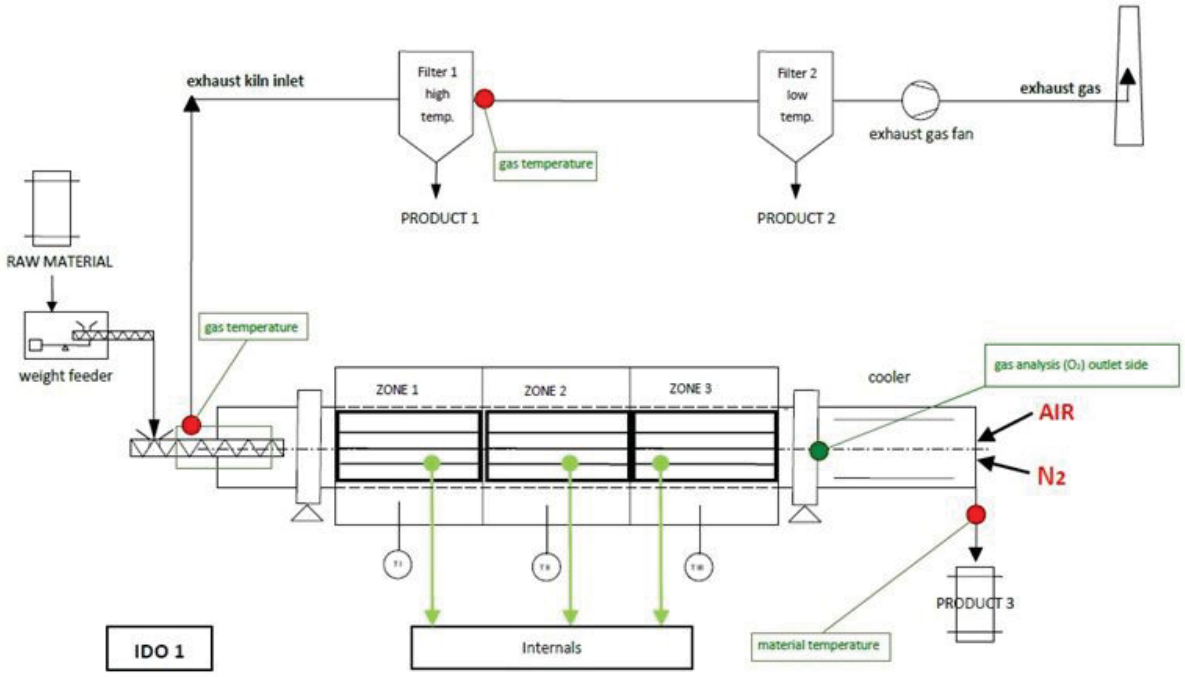

Figure 3.9: Schematic kiln design for industrial size experiment IBU 1

Experiment IBU 1 ran for 16.5 hours. After four hours the exhaust pipe was blocked due to condensation of MoO_3 sublimate, which had to be removed manually. To prevent further blockages the temperature close to the charging device was increased from 900 °C to 1000 °C, which consequently raised the temperature in the high temperature filter from 650 °C to 750 °C averting condensation in the exhaust pipe. After 12 hours no more mechanical removal of the blockage was necessary and the process ran stable until it had to be stopped due to problems with the charging system. The detailed changes of the process parameters throughout the experiment can be deducted from figure 6.25 in the appendix.

Due to the problems with the formation of ferromolybdenum (see results section) during the experiment IBU 1, the following test IBU 2 was conducted in a directly heated kiln (table 3.18) with a refractory lining. The initial process parameters can be seen in table 3.19. In order to protect the charging device, it was flushed with nitrogen throughout the experiment. To prevent blockages a big settling tank was connected directly to the end of the furnace in gas flow direction. Due to the expansion of the gas, it cools down and the sublimed material condenses in this big space, not blocking any exhaust pipes. The schematic process flow chart can be seen in figure 3.10. The detailed changes of the process parameters throughout the experiment can be deducted from figures 6.27-6.30 (appendix).

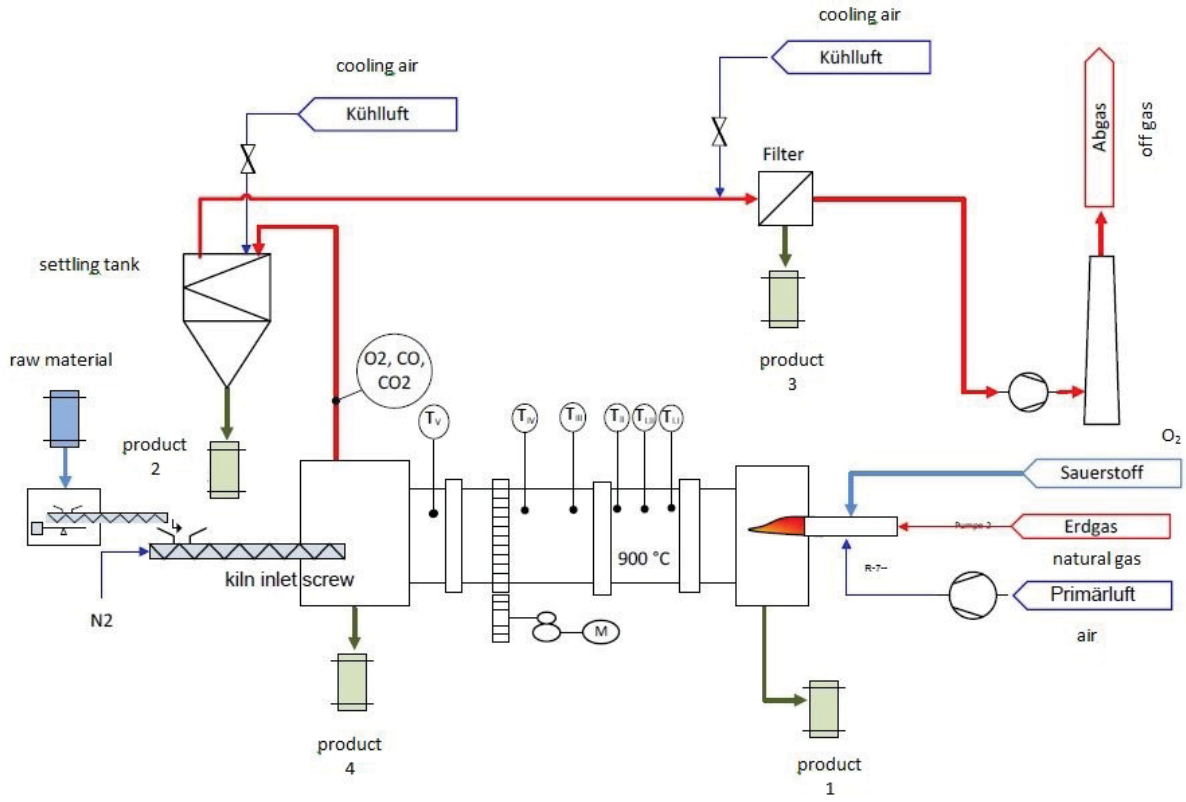

Figure 3.10: Schematic kiln design for industrial size experiment IBU 2

4 Results

This chapter lists the results of the conducted experiments. Their interpretation can be found in the discussion chapter of this thesis. When chemical compositions are stated in tables throughout this chapter, elements listed under "'Rest"' are always sorted according to their concentration within the analyzed substance, starting with the highest.

4.1 Oxidation kinetics

The results of the conducted isothermal experiments on molybdenum-tantalum and tungsten-rhenium alloys are described in the following sections.

4.1.1 Oxidation kinetics of a molybdenum-tantalum alloy

The evaluation of the rate constant for a specific temperature and alloy was performed through measuring the inclination of the plotted data points drawn from the yellow columns in tables 3.4 and 6.1-6.5 as well as tables 6.6-6.10. Therefore a linear trend-line was fitted to the data points (yellow line in figure 4.1-4.6). The better the fit, the higher the coefficient of determinatio R^2. The same method was applied for the deduction of the conversion of the sample at a specific temperature, taking the diffusion through the product layer into account (blue line in figure 4.1-4.6). The deducted rate constants and diffusion coefficients for the Mo-Ta alloy are displayed in table 4.1.

Table 4.1: Results regarding the rate constant for isothermal experiments on a Mo-Ta alloy

	Material	Temperature [°C]	rate constante k [g/(cm^2·s)]	diffusion coefficient d [cm^2/s]
ISO Mo-Ta 13	MoTa 11	975	0.000767	41.1
ISO Mo-Ta 1	MoTa 11	950	0.000711	39.3
ISO Mo-Ta 12	MoTa 11	925	0.000556	23.7
ISO Mo-Ta 2	MoTa 11	900	0.000295	9.42
ISO Mo-Ta 10	MoTa 11	875	0.000224	7.39
ISO Mo-Ta 3	MoTa 11	850	0.000225	3.05
ISO Mo-Ta 14	MoTa 11	975	0.000583	27.2
ISO Mo-Ta 5	MoTa 11	950	0.000609	32.4
ISO Mo-Ta 8	MoTa 11	925	0.000370	15.1
ISO Mo-Ta 4	MoTa 11	900	0.000313	12.4
ISO Mo-Ta 7	MoTa 11	875	0.000347	10.9
ISO Mo-Ta 6	MoTa 11	850	0.000297	3.16

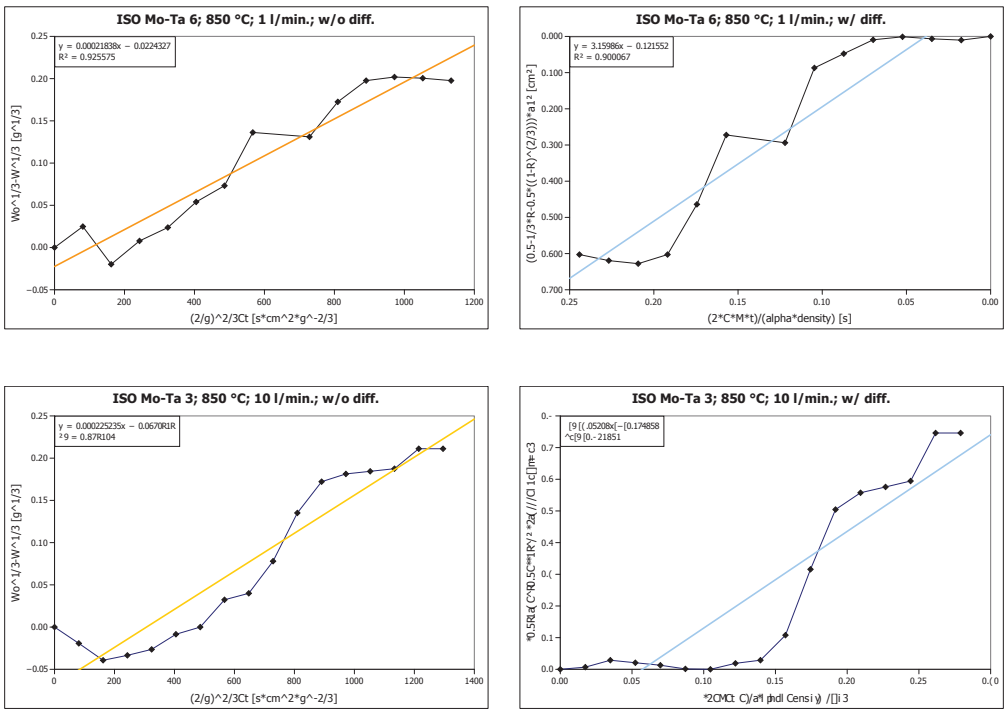

Figure 4.1: Determination of rate constant for 850 °C

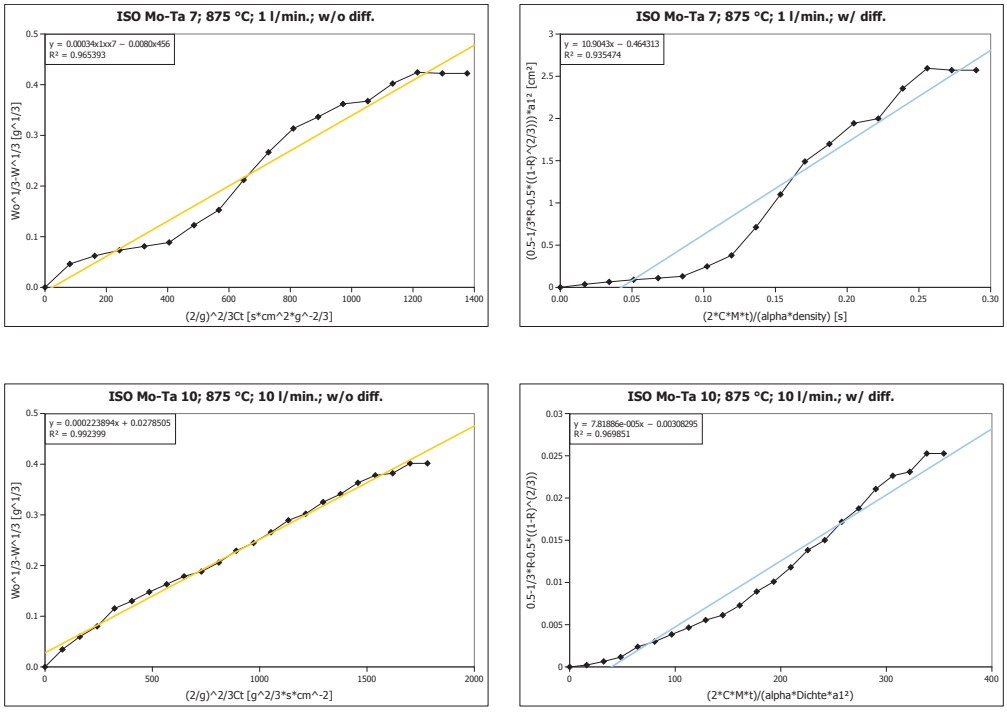

Figure 4.2: Determination of rate constant for 875 °C

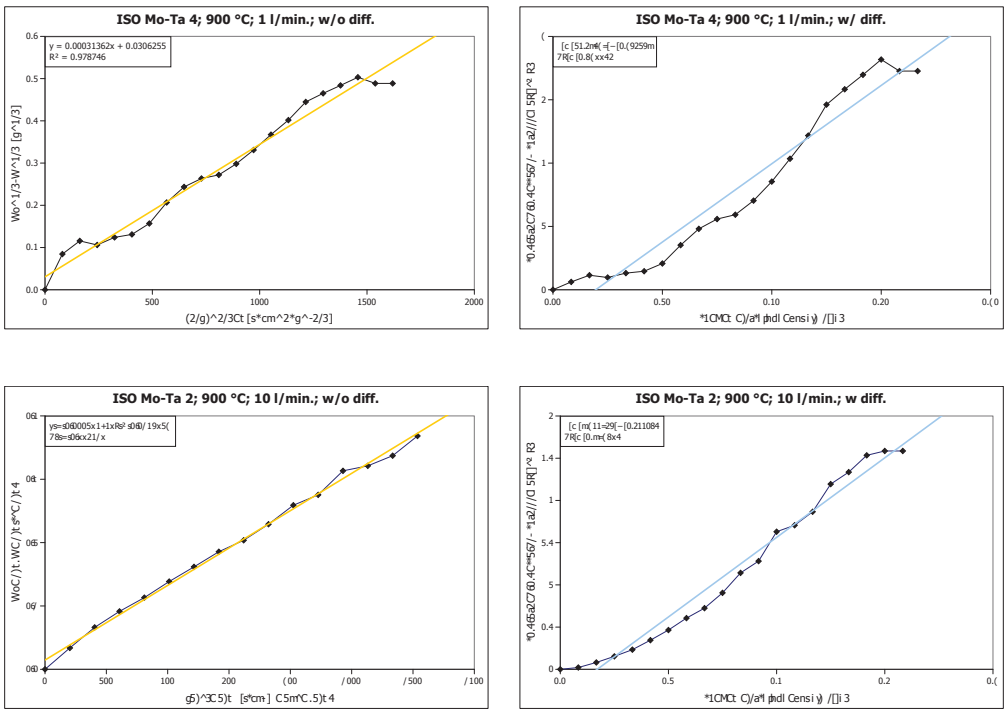

Figure 4.3: Determination of rate constant for 900 °C

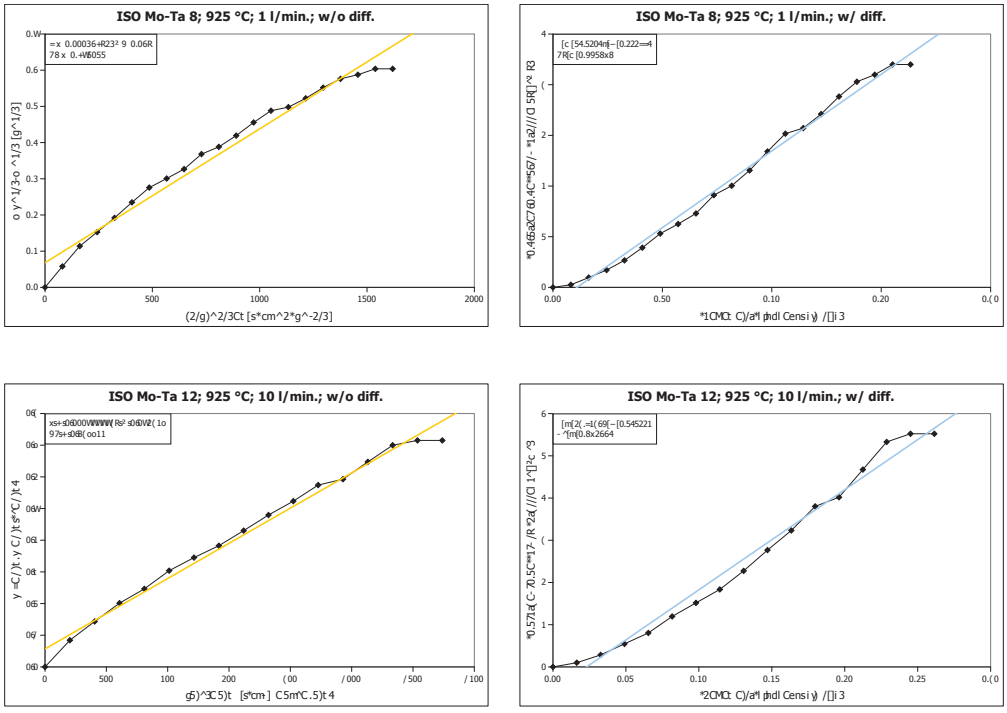

Figure 4.4: Determination of rate constant for 925 °C

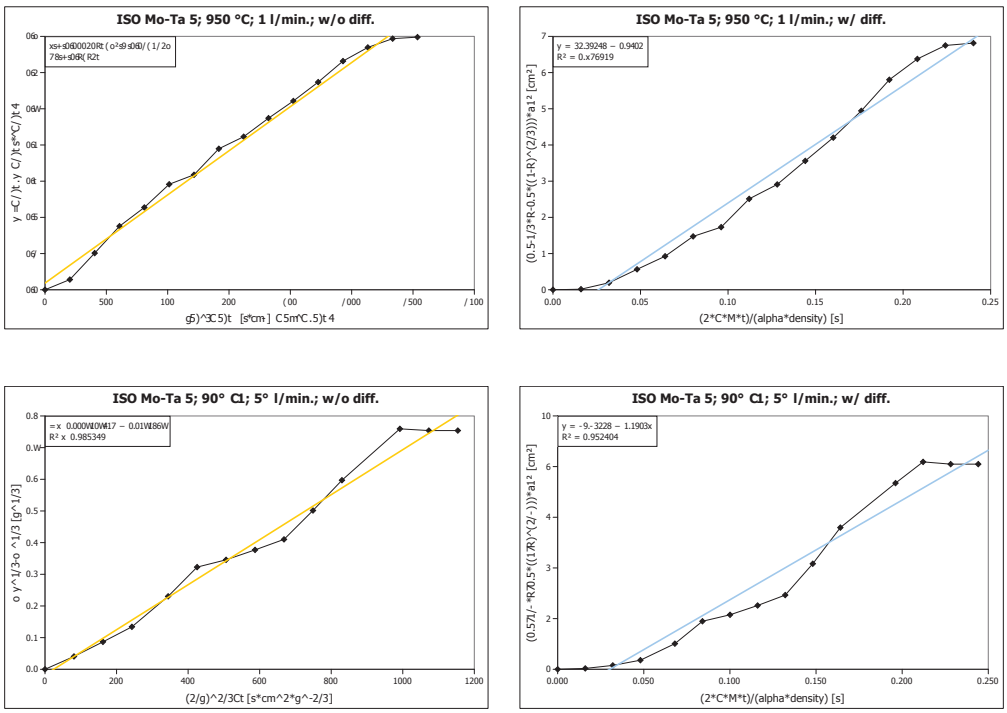

Figure 4.5: Determination of rate constant for 950 °C

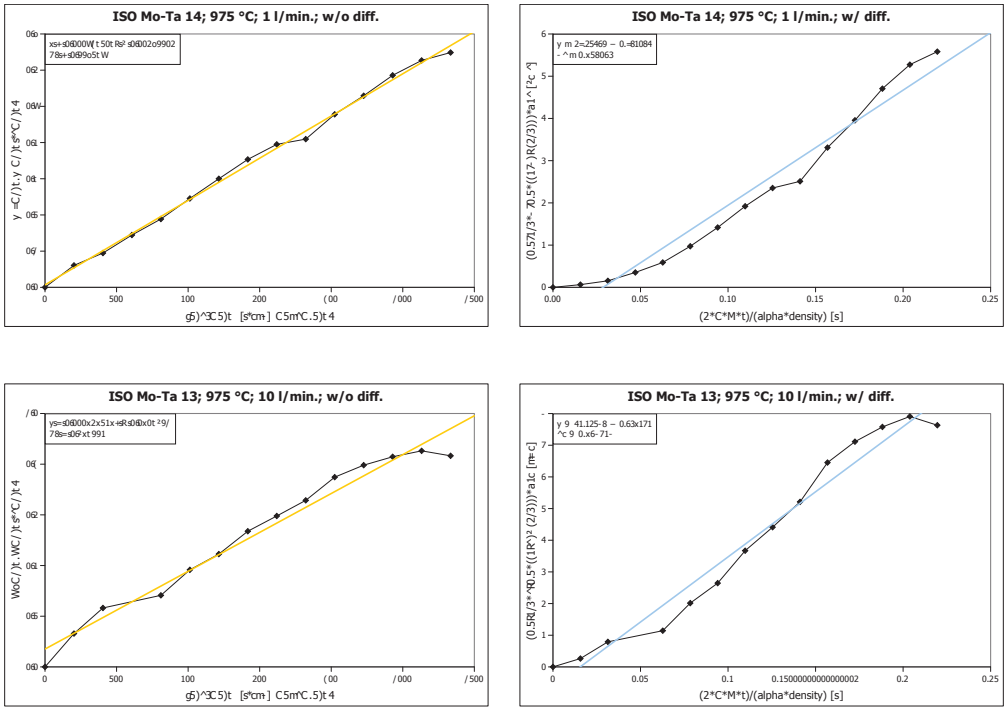

Figure 4.6: Determination of rate constant for 975 °C

The R-values, which give the accuracy of the fit can be seen in tables 4.2a and 4.2b.

Table 4.2: R^2-values of temperature dependency of rate constant

(a) R^2-values of temperature dependency of rate constant at 1 l/min

Temperature [°C]	R^2 without diffusion [-]	R^2 with diffusion	Difference in R^2-values [-]
850	0.897	0.822	0.075
875	0.992	0.970	0.023
900	0.996	0.975	0.022
925	0.985	0.953	0.033
950	0.975	0.992	-0.017
975	0.997	0.958	0.039
Sum	5.844	5.669	0.175

(b) R^2-values of temperature dependency of rate constant at 10 l/min

Temperature [°C]	R^2 without diffusion [-]	R^2 with diffusion [-]	Difference in R^2-values [-]
850	0.926	0.900	0.0255
875	0.965	0.935	0.0299
900	0.979	0.948	0.0310
925	0.975	0.992	-0.017
950	0.990	0.977	0.0128
975	0.974	0.969	0.0048
Sum	5.808	5.721	0.0874

All statistic analysis was conducted using GNU-R. The differences between the R^2-values for disregarding the diffusion through the product layer and taking the diffusion into account, for the respective gas velocity were tested for normal distribution. The results of the performed Shapiro-Wilk test are displayed in table 4.3. Due to the low p-values the data is likely to be normally distributed, hence a t-test was conducted. A one-sided approach was chosen for paired samples, since the difference in R^2-values (table 4.2a, 4.2b) already suggests that the data drawn from the approach not taking into account the diffusion through the product layer, leads to a better fit. This hypothesis is supported by a significant result in the t-test executed for the experimental data of the trials applying a gas flow rate of 1 l/min and a strong tendency towards significance for the experimental data of trials using a gas flow rate of 10 l/min.

Table 4.3: Statistical analysis of differences between taking/not taking the diffusion through the product layer into account

Shapiro-Wilk normality test			
data:	R_diff1	data:	R_diff10
W = 0.95	p-value = 0.74	W = 0.89	p-value = 0.30
Paired one-sided t-test			
t-value	p-value	t-value	p-value
2.39	0.031	1.95	0.055

When comparing the accuracy of fit for the different gas velocities (1 l/min and 10 l/min) for taking or not taking the diffusion through the product layer into account respectively, the results do not suggest a significant difference (table 4.4).

Table 4.4: Statistical analysis of differences between the gas velocities

Shapiro-Wilk normality test			
data:	R1_10_wo	data:	R1_10_w
W = 0.92	p-value = 0.47	W = 0.92	p-value = 0.50
Paired two-sided t-test			
data:	R_1wo & R_10wo	data:	R_1w & R_10w
t = 0.65	p-value = 0.55	t = -0.48	p-value = 0.65

In order to gain insights into the dependence of the rate constant on temperature, the natural logarithm of the rate constant is plotted over the inverse temperature, according to the arrhenius-approach explained in chapter 2.5. If one single chemical mechanism predominates the conversion of the material the dependence of the rate constant on the temperature is also called activation energy. However in the case of the molybdenum-tantalum alloy this is not the case, since oxidation and sublimation run simultaneously. Figure 4.7 shows the influence of temperature on the rate constant at 1 l/min (figure 4.7a) and 10 l/min (figure 4.7b) synthetic air. The inclination of the fitted line from the approach without taking the diffusion through the oxide layer into account, results, according to equation 36, for both gas flow in the values displayed

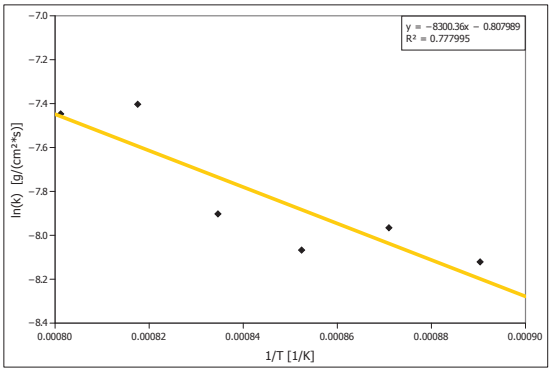

(a) Influence of temperature on the rate constant at 1 l/min synthetic air

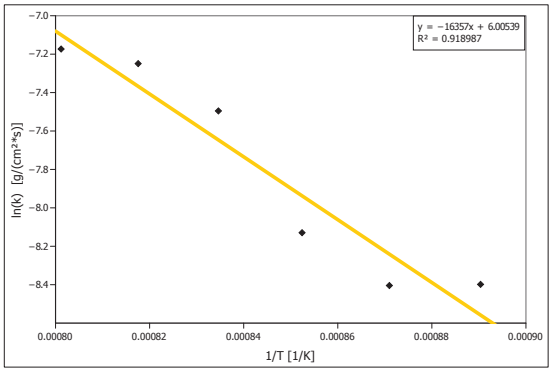

(b) Influence of temperature on the rate constant at 10 l/min synthetic air

Figure 4.7: Influence of temperature on the rate constant concerning the conversion of a MoTa 11-samples

in table 4.5.

$$ln\ k = ln\ k_0 - \frac{E}{RT} \tag{36}$$

Table 4.5: Activation energy for molybdenum oxidation and sublimation under different gas-velocity rates

1 l/min	10 l/min
69.009 kJ/mol	135.992 kJ/mol

The resulting conversion rate for Mo-Ta samples in 1 l/min air and 10 l/min air within a temperature range from 850 - 975 °C can be seen in equation 37 and 38 respectively.

$$k = 4.17 \cdot 10^{-7} - e^{\frac{69009}{RT}} \tag{37}$$

$$k = 6.38 \cdot 10^{-10} - e^{\frac{135992}{RT}} \tag{38}$$

4.1.2 Oxidation kinetics of a tungsten-rhenium alloy

The data evaluation was conducted along the lines described in section 4.1.1.

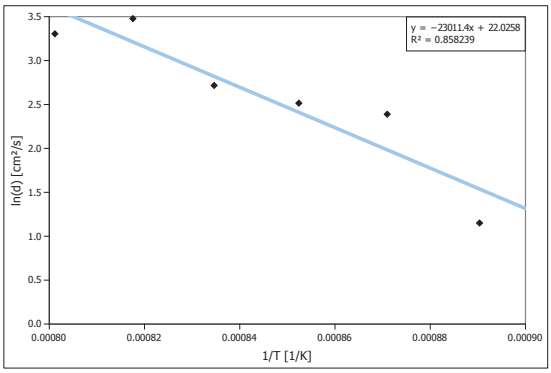

(a) Influence of temperature on the diffusion rate at 1 l/min synthetic air

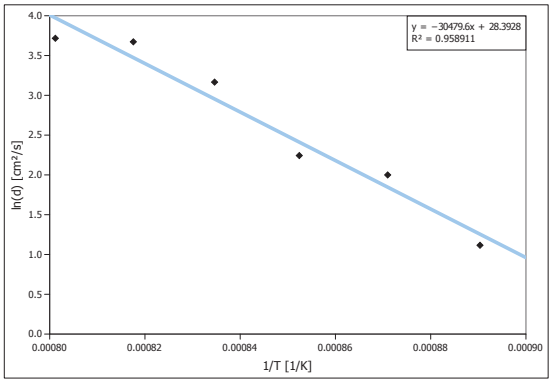

(b) Influence of temperature on the diffusion rate at 10 l/min synthetic air

Figure 4.8: Influence of temperature on the diffusion rate concerning the conversion of a MoTa 11-samples

The first oxidation kinetic experiments executed with 100% O_2 at 3 l/min gas flow rate, lead to data (table 6.17-6.19) which could not be linearized (figure 4.9) due to the periodic and intense spalling of the oxidic layer (figure 4.10).

Therefore, further experiments were performed with reduced oxygen content and increased gas flow rate in order to lower the oxidation intensity and the thickness of boundary layer respectively. This lead to a more homogeneous oxidation, which can be seen in figures 4.11 and 4.12. The deducted rate constants from the data displayed in tables 6.12-6.16 are listed in table 4.6.

Table 4.6: Rate constants and process parameters for isothermal experiments on a W-Re 25 alloy

Experiment	Material	Temperature [°C]	Rate constant k [g/(cm^2·s)]	Diffusion coefficient d [cm^2/s]
ISO W-Re 7	W-Re 25	900	$1.92 \cdot 10^{-05}$	0.011
ISO W-Re 8	W-Re 25	850	$6.10 \cdot 10^{-06}$	0.0048
ISO W-Re 9	W-Re 25	950	$3.39 \cdot 10^{-05}$	0.088
ISO W-Re 10	W-Re 25	925	$1.96 \cdot 10^{-05}$	0.0934
ISO W-Re 11	W-Re 25	875	$7.072 \cdot 10^{-06}$	0.0082

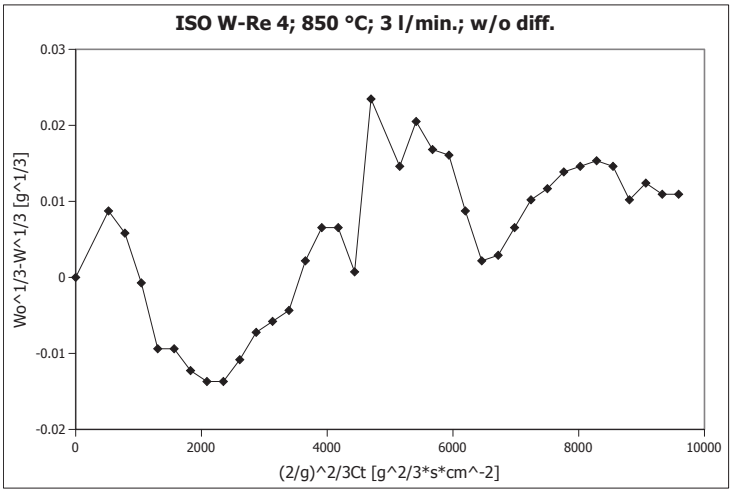

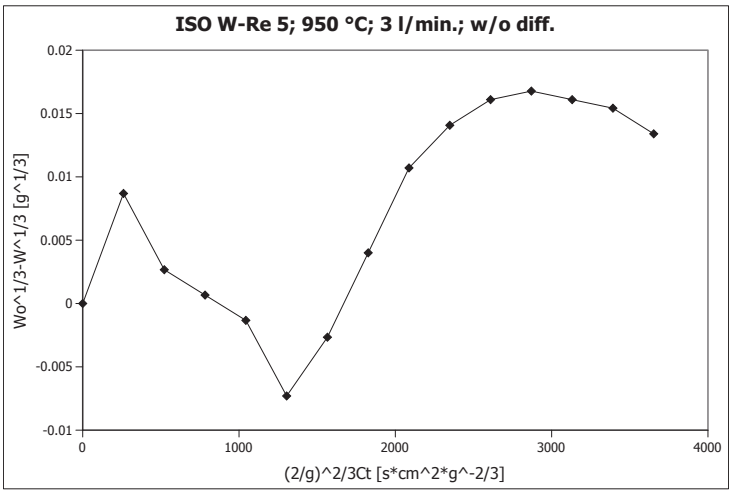

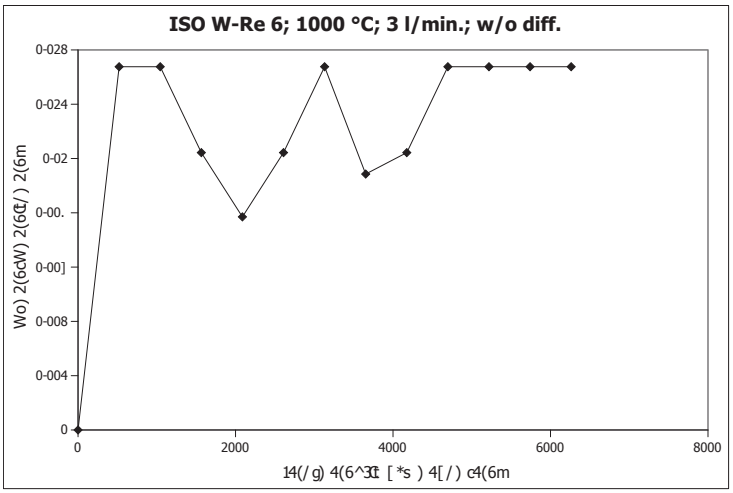

Figure 4.9: Oxidation behavior of a tungsten-rhenium alloy at 100 % O_2 and 3 l/min

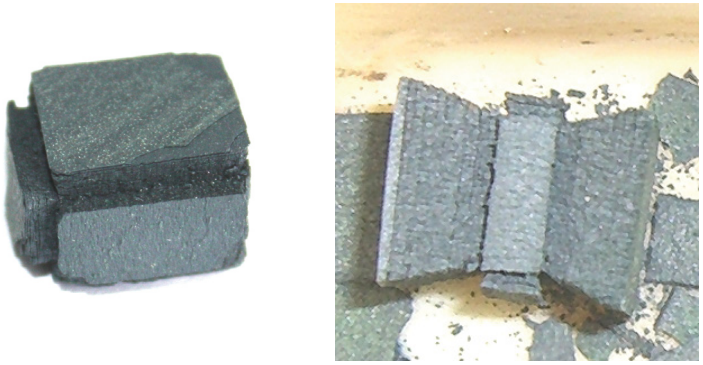

Figure 4.10: Periodic spalling of the oxidic layers in W-Re-samples at 100 % O_2 and 3 l/min

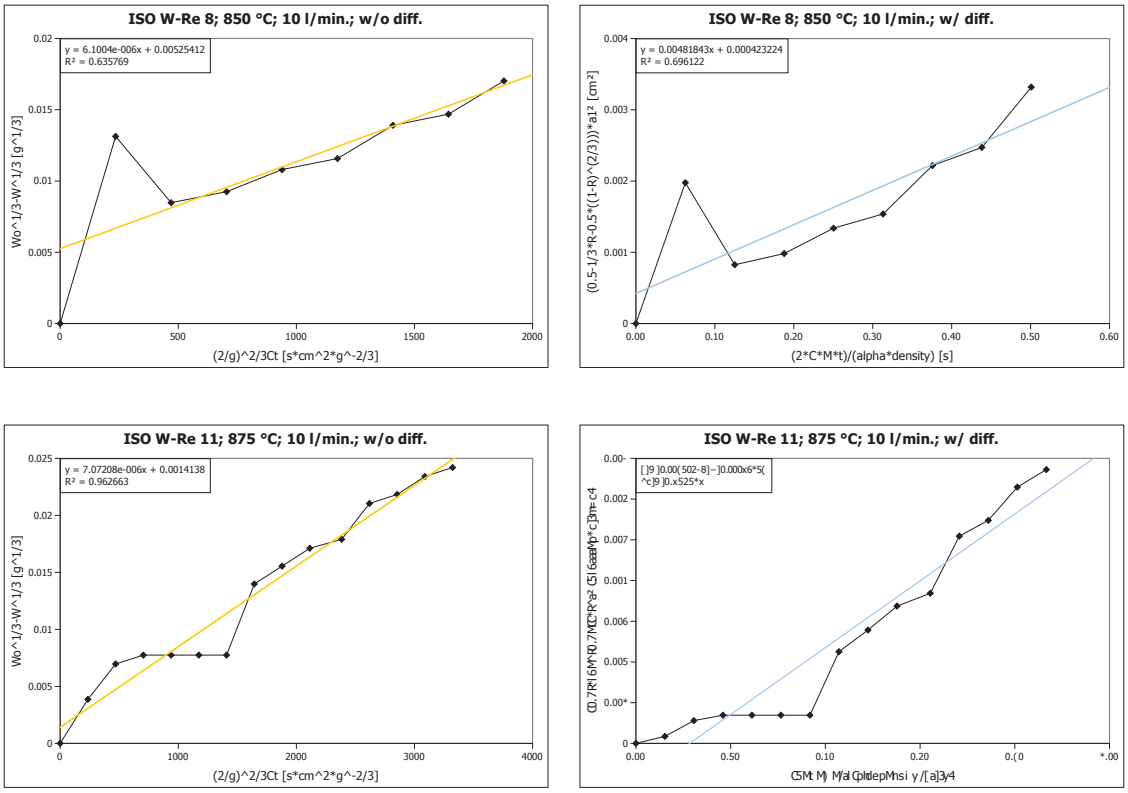

Figure 4.11: Oxidation behavior of a tungsten-rhenium-alloy with 90 % O_2 10 % N_2 and 10 l/min as a function of weight loss over time

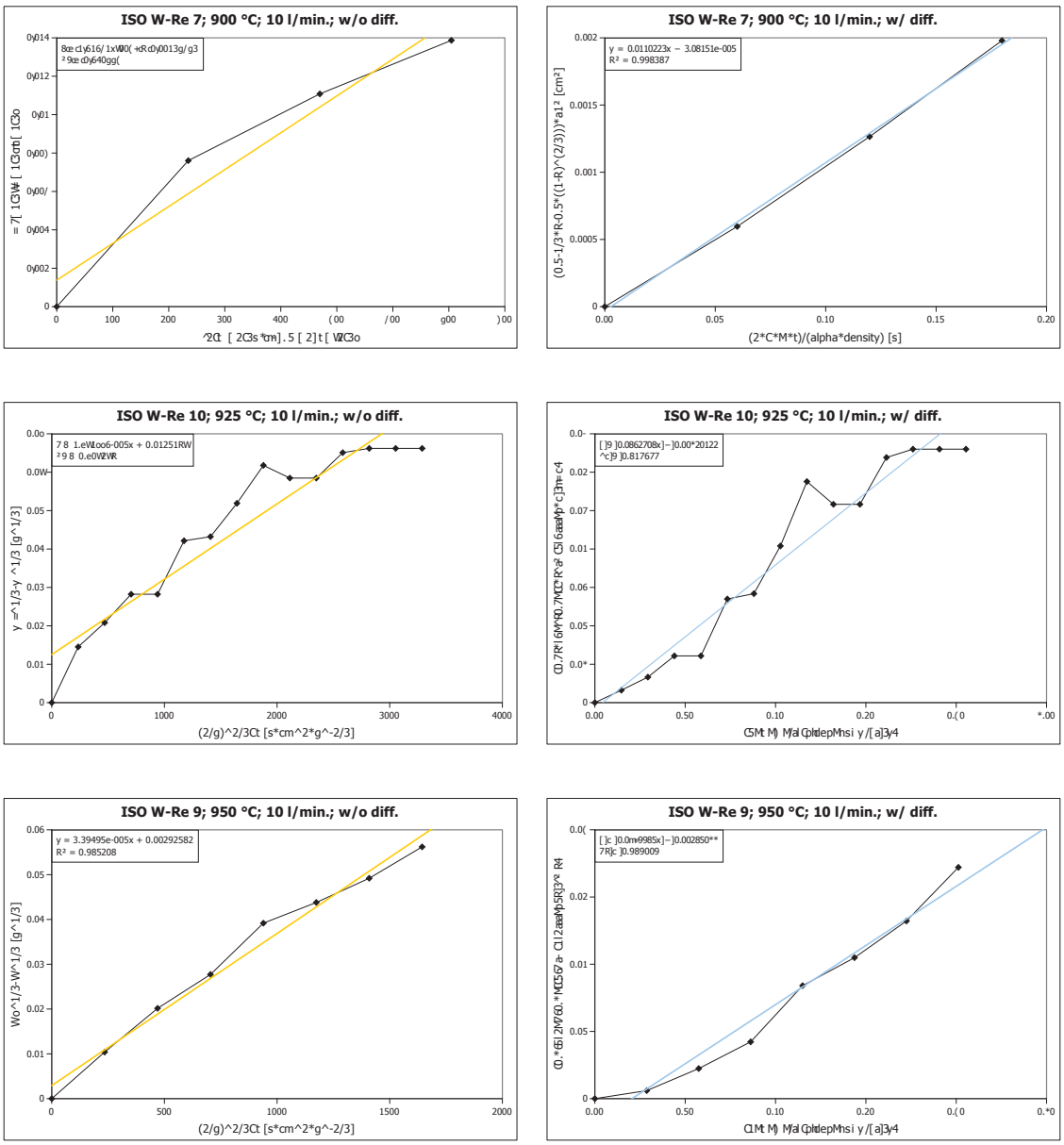

Figure 4.12: Oxidation behavior of a tungsten-rhenium-alloy with 90 % O_2 10 % N_2 and 10 l/min as a function of weight loss over time

In order to compare the accuracy of fit concerning the different approaches, a statistical evaluation of the R^2-values displayed in table 4.7 was conducted using GNU-R. The results of the statistical analysis can be seen in table 4.8. The differences in R^2-values between the approach taking the diffusion through the product layer into account and assuming a chemically controlled oxidation process showed a normal distribution (Shapiro-Wilk normality test). Because the differences in R^2-values in table 4.7 do not favor any of the two approches concerning accuracy of fit a two sided paired t-test was chosen, which showed no significance.

Table 4.7: R^2-values of temperature dependency of velocity constant

Temperature [°C]	R^2 without diffusion [-]	R^2 with diffusion [-]	Difference in R^2-value [-]
850	0.636	0.696	-0.060
875	0.963	0.926	0.036
900	0.941	0.998	-0.058
925	0.906	0.945	-0.039
950	0.985	0.969	0.016

Table 4.8: Statistical analysis of differences between taking/not taking the diffusion through the product layer into account

Shapiro-Wilk normality test	
data:	R_wo_w
W = 0.85	p-value = 0.21
Paired two-sided t-test	
data:	R_wo_w
t-value	p-value
-1.05	0.35

The dependency of the rate constant on the temperature was calculated using equation 36, drawing the data from the inclination of the data points in figure 4.13. The derived value is displayed in table 4.9.

The conversion of tungsten-rhenium samples in 90 % O_2 in a temperature range between 850 - 950 °C runs according to equation 39.

$$k = 2.35 \cdot 10^{-14} - e^{\frac{203545}{RT}} \tag{39}$$

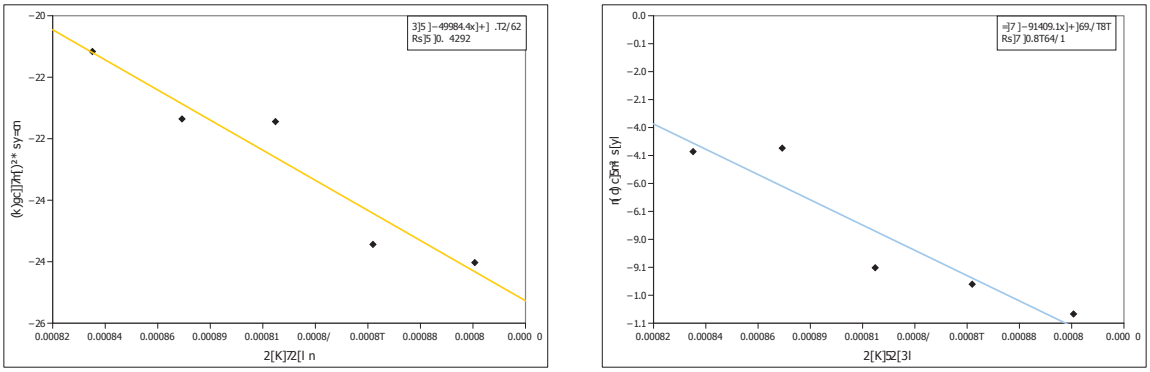

(a) Influence of temperature on the rate constant

(b) Influence of temperature on the diffusion related rate

Figure 4.13: Influence of temperature on the rate constant and diffusion related velocity rate on W-Re 25 samples at 10 l/min and 90 % O_2

Table 4.9: Activation energy for rhenium and tungsten oxidation and sublimation of rhenium

10 l/min
203.545 kJ/mol

4.2 Pilot tests on different materials

The pilot test were conducted to evaluate the process parameters to separate different alloys into their components. The chemical analysis were done with SEM-EDX, if not otherwise stated in tables 4.10 and 4.11. The composition of the residues in the crucible after the experiments are listed in table 4.10. The RFA results from experiment W-Re Ox 22 are only qualitative. Additionally, table 4.11 lists the SEM-EDX results of the resublimed material, collected from the filter bottle. The interpretation of these findings can be found in the discussion chapter.

Table 4.10: Chemical composition of the residues in crucible after experiments

[wt.-%]	Mo	W	Re	Ta	Nb	Cu	O	Rest
MoOx 1/2	6.88	74.28					16.89	Al, Fe, Ca, K
MoOx 3	6.89	78.21					12.54	Fe, Al
MoOx 4	1.66	81.85					16.48	
MoOx 5	12.41	61.21					21.24	Si, Al, K
MoOx 6	48.58	26.98					23.07	Fe, Cu
MoOx 7	7.09	74.05					18.86	
WReOx 8/9 outer oxide layer		79.07	8.01				12.92	
WReOx 8/9 inner oxide layer		73.27	13.01				13.01	
WReOx 10 oxide layer		88.41					11.59	
WReOx 12/13		82.78					16.22	
MoTaOx 14	35.75			43.17			21.07	
MoTaOx 17	62.06			14.31			23.63	
MoTaOx 18								
MoCuOx 19	49.77					27.38	21.78	K, Al, Si
WReOx 22 RFA:	W,O							
WReOx 22		79.1					20.9	
MoNbOx 23	9.8				53.5		36.7	
MoWOx 24	17.0	58.4					24.6	

Table 4.11: Chemical composition of sublimed material

[wt.-%]	Mo	W	Re	O	Rest
MoOx 1/2	68.93	1.96		28.82	Al
MoOx 3	66.45	1.70		30.74	Cu, Fe, Cr
MoOx 3	71.62	0.41		27.97	
MoOx 5	69.12	0.83		29.63	
MoOx 6	66.75			32.49	
MoOx 7	66.46			33.54	
MoTaOx 11	76.06			23.94	
WReOx 13	49.44		27.06	23.5	
MoTaOx 17	74.84			25.16	
MoTa Ox 18	75.18			24.82	
MoCuOx 19	68.08			31.92	
WReOx 22 RFA:	Re, Si, Mo, Fe				
WReOx 22	0.2		75.2	23.6	Si
MoNbOx 23	44.4		4.7	39.1	Zn
MoWOx 24	53.3	0.6		45.7	Na, Al

Separation of molybdenum and copper composite

The residues were analyzed with SEM-EDX after the evaporation and recondensation of zinc. This process to recycle Mo-Cu chips produces pure zinc, a fraction rich in copper surrounding the chips and chips with reduced copper content as products. The results are summarized in tables 4.12-4.18.

Table 4.12: Composition of the chip surface after experiment Mo-Cu 1

(a) Spectrum 59

Element	wt.-%
Molybdenum	91.0
Oxygen	7.3
Copper	1.3
Aluminum	0.4

(b) Spectrum 60

Element	wt.-%
Molybdenum	73.9
Copper	13.2
Oxygen	10.5
Zinc	1.1
Calcium	0.6
Aluminum	0.5
Silicium	0.2

Table 4.13: Composition of evaporated and condensed zinc after experiment Mo-Cu 1

(a) Spectrum 8

Element	wt.-%
Zinc	98.0
Oxygen	1.7
Nickel	0.3

(b) Spectrum 5

Element	wt.-%
Zinc	100

Table 4.14: Composition of the chip surface after experiment Mo-Cu 3

(a) Spectrum 10

Element	wt.-%
Molybdenum	92.5
Copper	7.5

(b) Spectrum 9

Element	wt.-%
Molybdenum	92.2
Copper	5.3
Sulfur	2.5

(c) Spectrum 11

Element	wt.-%
Molybdenum	41.1
Oxygen	27.2
Zinc	27.1
Sodium	2.1
Copper	1.3
Rest	1.1

Table 4.15: Composition of the evaporated zinc after experiment Mo-Cu 3

(a) Spectrum 12

Element	wt.-%
Zinc	98.1
Oxygen	1.6
Nickel	0.3

(b) Spectrum 13

Element	wt.-%
Zinc	96.2
Oxygen	3.8

The data displayed in table 4.16a is the chemical composition of the chip close to the chip surface, whereas table 4.16b shows the element contents of the chip, closer to the center. Additionally, table 4.17 depics the purity of the evaporated and condensed zinc.
Table 4.18 displays the chemical composition of the matrix surrounding the chips after evaporating the zinc.

Table 4.16: Composition of the chip after experiment Mo-Cu 4

(a) Spectrum 20

Element	wt.-%
Molybdenum	64.6
Oxygen	23.3
Lead	10.2
Copper	1.3
Antimony	0.4
Nickel	0.3

(b) Spectrum 21

Element	wt.-%
Molybdenum	61.3
Oxygen	25.5
Lead	5.5
Copper	3.3
Zinc	2.7
Antimony	1.1
Nickel	0.3
Aluminium	0.2

Table 4.17: Composition of the evaporated zinc after experiment Mo-Cu 4

Element	wt.-%
Zinc	99.7
Nickel	0.3

Table 4.18: Composition of the matrix surrounding the chips after experiment Mo-Cu 4

(a) Spectrum 54

Element	wt.-%
Molybdenum	31.9
Copper	29.3
Zinc	21.7
Oxygen	10.1
Antimony	2.9
Aluminium	1.9
Sodium	1.9
Iron	0.3

(b) Spectrum 49

Element	wt.-%
Copper	87.2
Zinc	8.6
Molybdenum	1.7
Antimony	1.5
Aluminium	0.6
Silicium	0.1
Iron	0.1

4.3 Optimization of process parameters

The results of the gravimetrical investigation are displayed in figures 4.14 and 6.1. The formation of a liquid phase was found in some of the experiments. If the liquid phase occurred at the beginning of the experiment but vanished at a later point in time, this point is marked pink in figure 4.14. For the formation of a liquid phase that arose throughout the experiment, there is a red mark to be found in figure 4.14 when it was first observed. The conditions under which a liquid phase appeared are displayed in table 4.19. The chemical analysis of the solidified liquid phase with SEM-EDX shows a molybdenum-tantalum oxide with varying elements contents (approx. 40 wt.-% Ta, 30 wt.-% Mo, 30 wt.-% oxygen).

Table 4.19: Conditions under which the liquid phase formed

Grainsize [mm]	O_2-content [vol.-%]	Temperature [°C]	Liquid phase [min]
< 1	12	850	80
> 6.3	12	850	186
1-2	35	850	20
> 6.3	35	850	80
1-2	12	850	120
< 1	35	900	40
2-4	60	850	From start
2-4	60	950	From start
4-6.3	60	900	From start
2-4	60	900	From start
> 6.3	60	900	From start
4-6.3	60	850	From start
> 6.3	60	950	From start

The data on oxidation time and residual MoO_3 in the tantalum oxide fraction was subjected to a statistical analysis and fitted to a trend line considering each process parameter as a factor, its squares and the mutual interaction of the factors. Equations 40 and 41 are the resulting empirical relations to estimate the oxidation time as well as the residual Mo content when inserting the temperature [°C], oxygen content of the process gas [vol.-%] and grain size [mm]. The equations are able to predict the results, found in the experiments with 79 % accuracy for the residual Mo content in the tantalum fraction and 94 % accuracy for the oxidation time. Figures 4.15-4.17 and 4.18-4.20 display the expected responses according to the model concerning the oxidation time and the residual Mo content respectively. The quality of the data

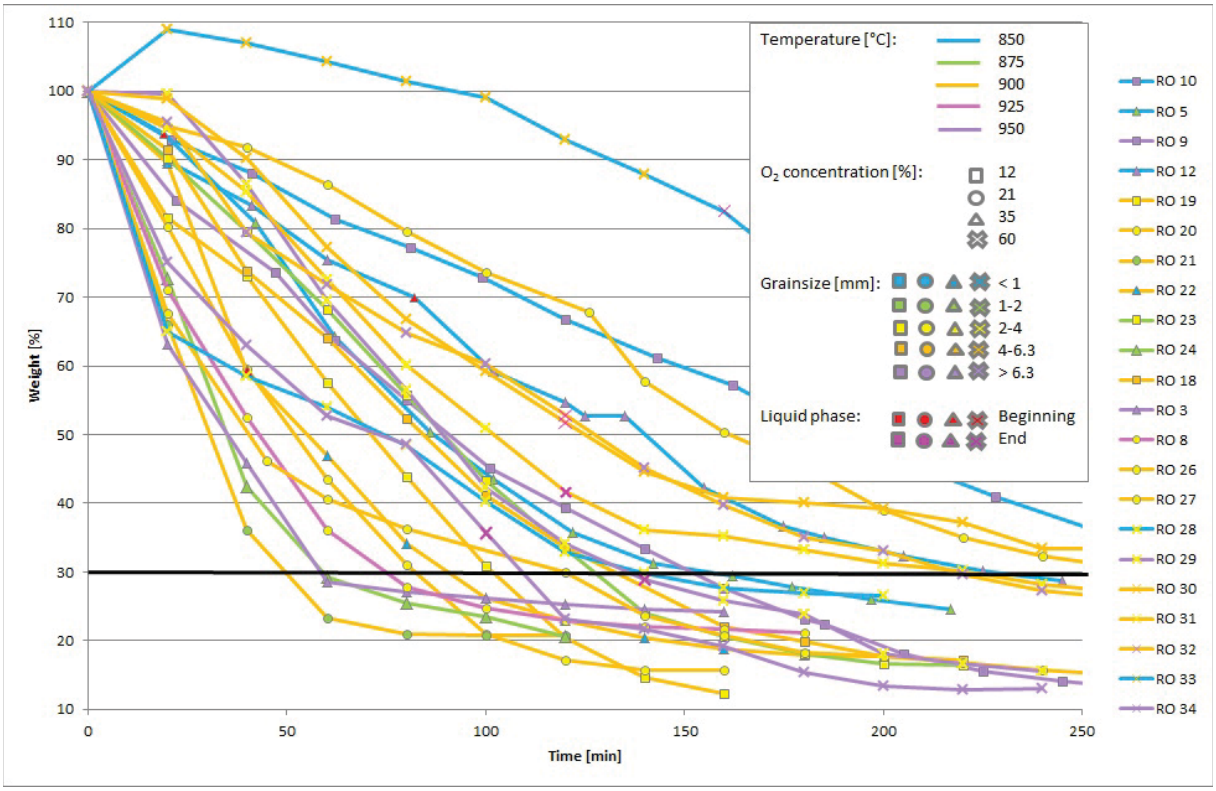

Figure 4.14: Results of gravimetric experiments for optimizing process parameters, weight loss as a function of time

can be estimated by looking at figures 6.2-6.10 and 6.11-6.19 in the appendix, displaying the predicted influence of one process parameter on the oxidation time of the sample or the residual MoO_3-content within the tantalum oxide fraction, while keeping the other ones constant at the values displayed in the upper right corner of these figures. The prediction was calculated using a

5 % confidence interval, which is represented by the upper and lower lines within the figures. The magnitude of each of the coefficients is displayed in figures 6.20 and 6.21. A significant influence can be assumed, when the confidence interval bar does not cross the abscise of the plot.

$$\begin{aligned} t\ [min] = 4748.36 - Gr \cdot 204.50 + \\ O_2 \cdot 27.79 - T \cdot 11.04 - Gr \cdot Gr \cdot 0.749 + O_2 \cdot O_2 \cdot 0.126 + \\ T \cdot T \cdot 0.00650 - Gr \cdot O_2 \cdot 0.528 - Gr \cdot T \cdot 0.187 - O_2 \cdot T \cdot 0.0366 \end{aligned} \quad (40)$$

Gr. . . grain size [mm], O_2. . . oxygen content of the process gas [vol.-%], T. . . temperature [°C]

$$
\begin{aligned}
Mo\ \ [wt.-\%] = 1546.96 + Gr \cdot 11.56 + \\
O_2 \cdot 3.94 + T \cdot 3.41 + Gr \cdot Gr \cdot 0.37 - O_2 \cdot O_2 \cdot 0.0053 - \\
T \cdot T \cdot 0.0019 - Gr \cdot O_2 \cdot 0.079 - Gr \cdot T \cdot 0.012 - O_2 \cdot T \cdot 0.0031
\end{aligned} \tag{41}
$$

Gr. . . grain size [mm], O_2. . . oxygen content of the process gas [vol.-%], T. . . temperature [°C]

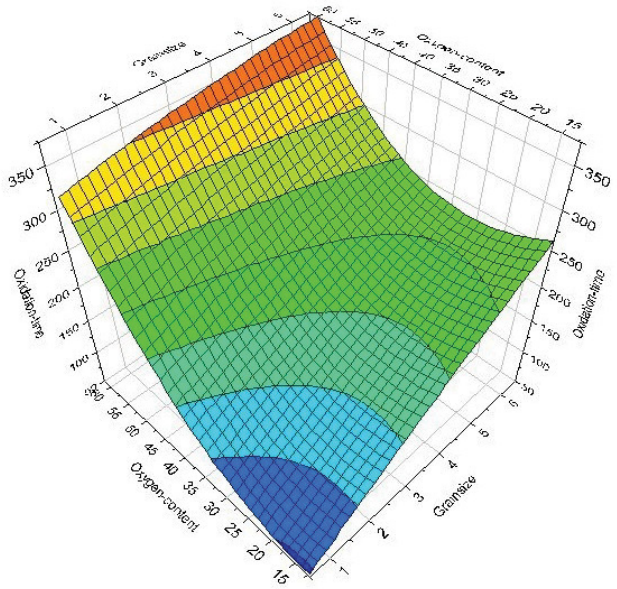

Figure 4.15: Expected response according to the model concerning the oxidation time when varying the grain size and oxygen content of the process gas at 850 °C

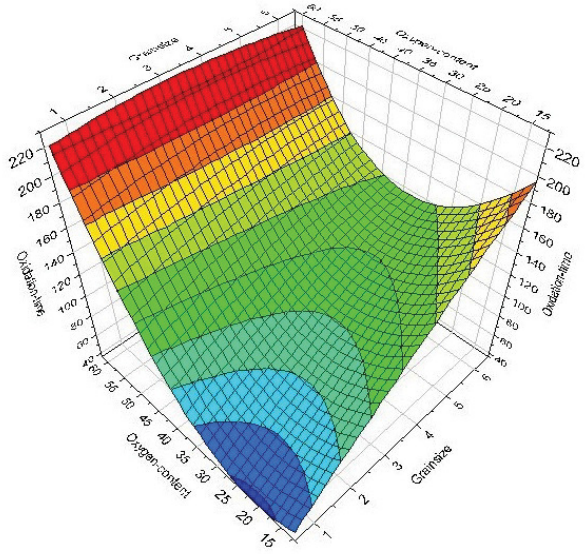

Figure 4.16: Expected response according to the model concerning the oxidation time when varying the grain size and oxygen content of the process gas at 900 °C

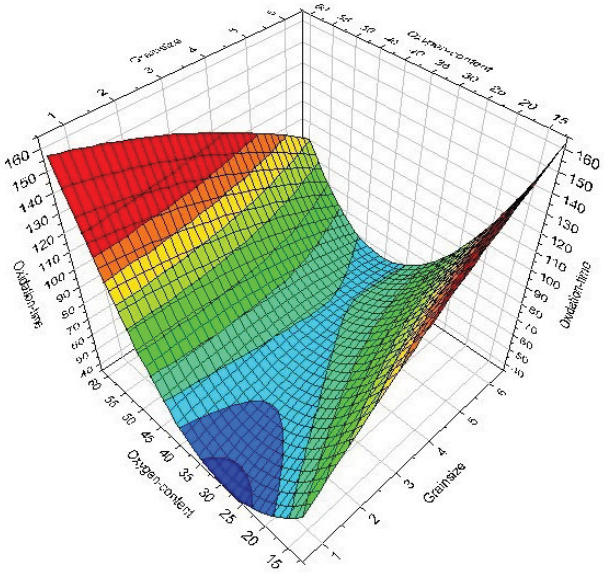

Figure 4.17: Expected response according to the model concerning the oxidation time when varying the grain size and oxygen content of the process gas at 950 °C

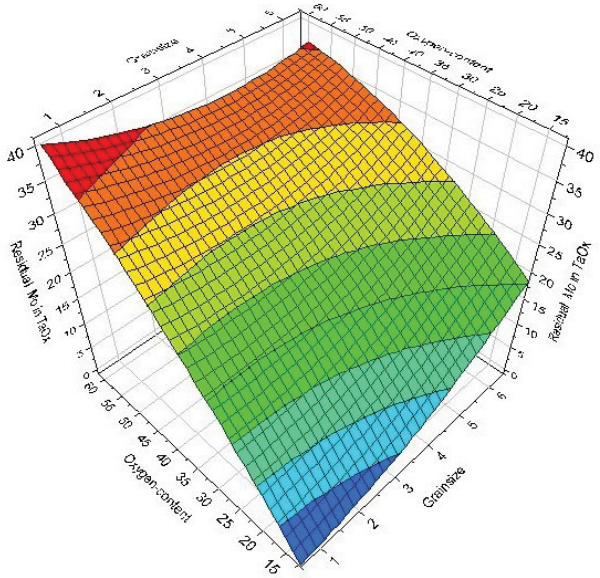

Figure 4.18: Expected response according to the model concerning the residual Mo content within the oxidic tantalum fraction when varying the grain size and oxygen content of the process gas at 850 °C

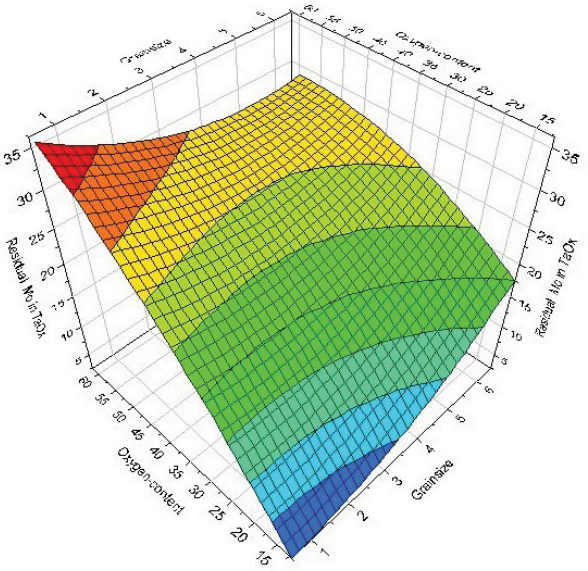

Figure 4.19: Expected response according to the model concerning the residual Mo content within the oxidic tantalum fraction when varying the grain size and oxygen content of the process gas at 900 °C

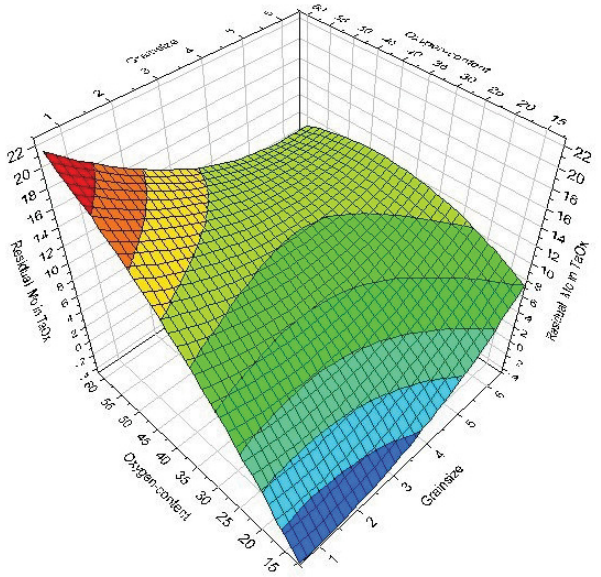

Figure 4.20: Expected response according to the model concerning the residual Mo content within the oxidic tantalum fraction when varying the grain size and oxygen content of the process gas at 950 °C

4.4 Results of experiments in a laboratory rotary kiln

The experiments in the laboratory rotary kiln were conducted to perform the first upscaling step from the pilot experiments. The chemical analysis of the products are listed in table 4.20 for trials D-Mo 1 until D-Mo-Ta 9. Table 4.21 shows the SEM-EDX analysis of the fractions collected after experiments D-Mo-Ta 10 to D-W-Re 20. The areas marked grey represent residues collected from the drop tank, which should contain a higher content of the non volatile oxides. The volatile oxides are MoO_3 and Re_2O_7. Whereas the other materials either came from the filter bottle or the charging area which should represent fractions rich in recondensated substances due to the counter current process. The sample from the charging area was collected if no sublimated material had reached the filter bottle. In order to get a more detailed insight into the purity of the sublimated fraction ICP-OES analysis were done on the contents of the filter bottle. These results are listed in table 4.22. The results of the chemical analysis of the fractions collected after the conversion of the produced pellets in the laboratory size rotary kiln can be seen in table 4.23.

Table 4.20: Chemical analysis of residues after experiments conducted in the laboratory rotary kiln

[wt.-%]	Mo	O	W	Ta	Re	Ti	Rest	MoO_3	WO_3	Re_2O_7	Ta_2O_5	Rest
D-Mo 1 filter SEM-EDX	75.56	24.44										
D-Mo 2 charging area SEM-EDX	74.93	25.07										
D-Mo 3 filter SEM-EDX	75.01	24.99										
D-Mo-Ta 4 filter SEM-EDX	75.18	24.82										
D-Mo-Ta 4 drop tank SEM-EDX	73.55	19.97		6.48								
D-Mo-Ta 5 filter SEM-EDX	76.80	23.30										
D-Mo-Ta 5 charging area SEM-EDX	74.75	25.25										
D-Mo-Ta 5 kiln entrance SEM-EDX	75.67	24.33										
D-Mo-Ta 5 chip spectrum 2 SEM-EDX	87.68	2.81		9.51								
D-Mo-Ta 5 chip spectrum 3 SEM-EDX	76.01	17.74		6.51								
D-Mo-Ta 5 chip spectrum 4 SEM-EDX	39.22	15.10		45.68								
D-Mo-Ti 6 chip SEM-EDX	99.49					0.51						
D-Mo-Ti 6 filter RFA	66.54	33.33	0.0829		0.0461			99.84	0.105	0.0599		
D-Mo-Ta 7 filter SEM-EDX	71.96	28.04	0.0907					99.89	0.114			
RFA	66.57	33.33										
D-Mo-Ta 7 drop tank SEM-EDX	72.52	25.45	1.19			0.85						
D-Mo Ti 8 filter SEM-EDX	67.65	32.02	0.219		0.140		Na	99.54	0.276	0.182		
RFA	66.34	33.22										
D-Mo-Ti 8 drop tank SEM-EDX	81.47	18.24				0.3						
D-Mo-Ta 9 filter SEM-EDX	64.96	34.21	0.155				Na, Cu	99.80	0.196			
RFA	66.52	33.32										
D-Mo-Ta 9 drop tank SEM-EDX sintered spectrum 1	69.94	20.57	1.67	6.57			Al, K					
D-Mo-Ta 9 drop tank SEM-EDX sintered spectrum 2	40.92	23.00		34.25			Al, K					
D-Mo-Ta 9 blockage SEM-EDX	71.76	28.24										

Table 4.21: Chemical analysis of residues after experiments conducted in the laboratory rotary kiln

[wt.-%]	Mo	O	W	Ta	Re	Ti	Rest	MoO_3	WO_3	Re_2O_7	Ta_2O_5	Rest
D-Mo Ta 10 filter SEM-EDX	69.08	30.92										
D-Mo-Ta 11 filter RFA	66.66	33.33						99.99				
D-Mo-Ta 12 filter RFA	66.64	33.33					Ni	99.98				NiO
D-Mo-Ta 13 filter RFA	66.46	33.42					P	99.72				P_2O_5
D-W-Re 14 sublimate kiln wall RFA	19.47	25.78	7.91	1.14	44.46		K, Al, Fe, Ca	29.22	9.98	57.82	1.40	K_2O, Al_2O_3, Fe_2O_3, CaO
D-Mo-Ta 15 filter SEM-EDX	57.5	39.0					S (1.9), Cu, Na, Pd, Al					
D-Mo-Ta 15 drop tank SEM-EDX	40.00	31.73	8.02	17.07			Zn, Al, Si, Ni					
D-Mo-Ta 16 filter SEM-EDX	58.8	40.5					Cu, Na					
D-Mo-Ti 17 filter SEM-EDX	57.3	38.6					S (2.1), W, Cu Pd, Na, Al					
D-Mo-Ti 17 drop tank SEM-EDX	48.32	37.60	9.43				Sr, K, Al, Ti, Ca					
D-Mo-Ti 18 filter SEM-EDX	58.2	41.4					Na, Al					
D-Mo-Ti 18 charging area SEM-EDX	59.5	38.9	0.7				Cu, Na, Al					
D-Mo-Ti 18 drop tank SEM-EDX	18.2	30.9	39.2				Al (4.7), Sr(3.6), Si(1.8), Ti, K					
D-W-Re 20 filter SEM-EDX	0.2	24.9			74.9							
D-W-Re 20 drop tank SEM-EDX spectrum 1		25.1	74.9									
D-W-Re 20 drop tank SEM-EDX spectrum 2	0.2	27.4	68.2		3.8		Fe					
D-W-Re 21 charging area SEM-EDX	0.7	23.3			75.1		Al, Na					
D-W-Re 21 drop-tank	0.7	23.6	74.6				Fe, Ni, Al					

Table 4.22: ICP analysis of sublimed material collected from the filter bottle after various experiments

[µg/g]	D-Mo 2	D-MoTa 7	D-MoTa 12	D-MoTa 13 subl	D-MoTa 13 res	D-MoTa 15 subl	D-MoTa 15 res
Ta	66	41	498	1593		15	
W	24	982	46	64	< 20	922	< 20
Mo					< 10		< 10

Table 4.23 shows the SEM-EDX analysis of residues from rotary kiln experiments on pelletized slurry.

Table 4.23: SEM-EDX analysis of residues from rotary kiln experiments on pelletized slurry

[wt.-%]	Mo	W	O	Rest
D-Mo-W P1 drop tank	2.0	67.3	30.5	K
D-Mo-W P1 charging area	40.0	27.5	32.3	
D-Mo-W P2 drop tank	3.0	63.5	33.3	K
D-Mo-W P2 charging area	41.0	22.4	36.6	
D-Mo-W P3 drop tank	4.0	64.6	31.3	K
D-Mo-W P3 filter	52.5	2.1	44.6	Cu, Na
D-Mo-W P4 drop tank	2.1	67.8	29.9	K
D-Mo-W P4 charging area	29.2	38.4	32.3	K
D-Mo-W P5 filter	61.9	0.9	35.9	K, Fe, Al, Na
D-Mo-W P6 filter	61.0	6.2	32.2	K
D-Mo-W P7 filter	62.7	2.6	34.5	

4.5 Results of upscaling experiments in an industrial rotary kiln

The purity of the products represents a key result of the industrial size experiments. Table 4.24 shows the most important results of the ICP-analysis of the MoO_3 fraction collected from the filter. The residues taken from the drop tank were also analyzed. The results of the RFA and ICP analysis are displayed in table 4.25. Due to the high content of molybdenum and iron in the material from the drop tank as well as the significant damages to the kiln wall (figure 6.26a), the charging device (figure 6.26c) and the construction inside the kiln (figure 6.26b) further investigations were conducted after the experiment.

An experiment simulating the conditions during experiment IBU 1 was executed in the furnace,

Table 4.24: Filter fraction ICP IBU 1, MoO_3 with listed impurities at different times

[µg/g]	9:35	13:20	14:45
Ta	482	64	319
W	873	4282	3127

Table 4.25: Residue fraction IBU tec 1

RFA [wt.-%]	9:00	22:00
Mo	34.05	30.45
Fe	12.15	12.95
Cr	5.40	5.55
Ni	4.80	4.7
Ta	13.45	14.50
Ti	1.95	4.00
W	1.95	3.00
ICP [µg/g]		
Mn	2000	2000
Si	3055	3428

used for the pilot experiments. The Mo-Ta chips were charged on top of a steel plate, made of the same alloy as the charging device into a crucible. After oxidizing the chips for 4 hours at 900 °C, a RFA analysis provided the composition of the products. The results can be seen in table 4.26.

Table 4.26: XRD phase analysis IBU 1

Phase	MoO_3	MoO_3	$Fe_2(MoO_4)_3$	$FeTaO_4$	$Mo_{13}O_{33}$	Mo_2TaO_{11}
	Othorombic	Monoclinic				
Solid residue in crucible	x	x	x	x	x	x
Powder residue in crucible	x	x	x	x	x	
Material on steel plate	x	x	x	x		
Steel plate	x	x	x	x	x	

Before performing the next experiment the effect of oxidizing Mo-Ta chips on a piece of refractory lining identical to the one in the kiln, used for experiment IBU 2, was studied to eliminate further

risk of damage. No visible damage to the refractory material could be seen after oxidizing chips for four hours on top of it. The chemical analysis from the filter fraction as well as from the drop tank sample can be seen in tables 4.27 and 4.28 respectively. The mass of the filter fraction quantified the output of the process. These results can be seen in table 6.20, whereas table 4.29 shows the purities for MoO_3 that Plansee SE requires from their suppliers.

Table 4.27: Impurity contents [µg/g] of filter fraction, IBU 2

Date Time	P4 27.5 16:10	P7 27.5 18:15	P9 27.5 22:10	P11 28.5 2:10	P13 28.5 6:10	P15 28.5 10:10	P17 28.5 14:10	P19 28.5 18:00	P21 28.5 22:10	P23 29.5 3:10	P25 29.5 6:10	P27 29.5 10:10	P29
Ta	93	56	136	158	252	3630	101	59	25	29	43	1389	510
W	94	74	107	68	66	86	367	538	489	412	389	335	132
Ti	13	8	10	7	5	114	< 2	< 2	< 2	< 2	< 2	141	2
Fe	91	62	37	58	16	1832	10	< 5	< 5	< 5	7	133	39
Cr	3	3	3	10	3	18	3	3	3	3	3	6	5
Al	23	28	39	23	31	629	9	< 5	< 5	< 5	9	91	37
Pb	< 5	< 5	< 5	< 5	< 5	< 5	< 5	< 5	< 5	< 5	< 5	< 5	< 5
Mg	< 5	6	< 5	< 5	80	< 5	< 5	< 5	< 5	< 5	< 5	17	6
Ni	< 5	< 5	49	7	< 5	19	< 5	5	5	-	< 5	7	< 5
Cu	-	< 5	5	6	8	104	< 5	< 5	< 5	< 5	< 5	38	15
Si	12	15		19	16	26	14	14	14	18	18	27	15
K	105	65	184	70	48	163	101	68	100	278	118	90	123
Na	27	18	49	21	16	119	34	20	24	36	31	57	42
Ca	22	112	67	34	< 10	499	< 10	< 10	< 10	< 10	< 10	111	34
C	222	201	377	3015	1985	1405	279	230	169	275	289	177	1225

Table 4.28: Impurity contents of drop tank fraction, IBU 2

	EDX MUL			RFA Plansee		ICP Plansee							
Date Time	Mo [wt.-%]	Ta [wt.-%]	O [wt.-%]	Mo [wt.-%]	Ta [wt.-%]	Al [μg/g]	Cr [μg/g]	Fe [μg/g]	Ni [μg/g]	Ca [μg/g]	Mn [μg/g]	Ti [μg/g]	Zr [μg/g]
27.05.2015 10:00	34.4	22.3	40.1		9.8	1254	17	504	32	1102	50	157	17
27.05.2015 13:00	26.1	30.6	37.1		18.8	2010	51	1686	126	6615	476	895	200
27.05.2015 18:00	34.4	22.3	40.1		18.2	2114	67	2062	156	6444	327	1478	311
27.05.2015 23:00	43.0	16.2	38.7										
28.05.2015 00:00	38.5	23.6	36.2		11.3	1630	21	863	37	4006	71	792	205
28.05.2015 04:00	41.2	20.5	37.1		10.8	1187	20	587	39	2555	46	203	91
28.05.2015 08:00	47.0	35.5	16.4		12.1	993	27	685	14	2594	38	164	48
28.05.2015 14:00	31.5	21.7	46.8		11.25	944	25	425	45	1284	16	229	52
28.05.2015 18:00	35.9	26.4	36.4		14.55	782	14	398	20	1944	25	106	41
28.05.2015 22:10	24.9	38.8	26.4		18.4	1473	22	888	29	4232	45	324	116
29.05.2015 03:10	11.7	51.2	32.7	13.6	82.85	1954	84	928	45	4858	122	705	216
29.05.2015 06:10	25.4	33.9	37.9		26.75	1713	24	1158	63	6585	63	275	104
29.05.2015 10:10	17.8	46.3	32.6	35.4	49.75	1641	239	2158	419	6235	129	444	103
29.05.2015 14:10	19.7	40.8	34.6		52.9	2058	37	1293	79	5425	65	449	106

Table 4.29: Plansee requirements for MoO_3 used in primary Mo metal production

Element [µg/g]	Max. values	Element [µg/g]	Max.values
Al	10	Pb	10
Ca	10	Si	20
Cr	10	Ti	10
Cu	10	C	50
Fe	10	W	150
K	20-70	$H_2O + NH_3$	1500
Mg	10	Ni	5
Na	20	others	20

5 Discussion

The following chapter will discuss the results of each series of executed experiments, especially emphasizing corresponding and contradicting results along the up-scaling process.

5.1 Oxidation kinetic experiments

The experiments on oxidation kinetics fitted the gravimetrical results for the conversion of the sample assuming a purely chemically controlled process as the first approach and a solemnly diffusion controlled process as the second approach. The truth can be assumed to lie somewhere in between. There is no data available yet on the oxidation kinetics of a similar Mo-Ta alloy however the ratio of a chemically controlled conversion to a diffusion controlled one can be estimated when comparing the results of this work to the data from the literature on pure molybdenum. The plotted data according to the two approaches was reviewed concerning the accuracy of fit towards a linear trend line to evaluate independently, from the research on which process is actually dominant in the conversion and the resulting velocity rate and diffusion constant, how well each of the model is suitable to describe the conversion.
The rate constants found within this work for Mo-Ta samples increase with rising temperatures and there is also a tendency for higher values at growing gas flow rates within the furnace. This is most likely due to a thinner cloud of sublimed product surrounding the sample at higher gas velocities, which is in good accordance with the stated effect of amplified gas velocities resulting in faster molybdenum conversion in the literature [8]. When comparing the values to those, which result from equation 2 for pure molybdenum, drawn from the literature and only valid for a temperature range between 700 °C and 800 °C, there exists a very good accordance at 850 °C. However with increased temperatures, the equation would result in values approx. 10-fold higher than the ones drawn from the conversion of the sample. This leads to the conclusion that the ratio of chemically controlled to diffusion controlled in the conversion mechanism depends on the temperature. At higher temperatures, the reaction is likely to become more diffusion regulated, since the chemically controlled conversion relates exponentially to the temperature according to Arrhenius' approach, whereas the diffusion coefficient according to

Ficks law linearly increases with the temperature [62, 63]. The activation energy drawn from the conducted experiments is lower than the values stated in the literature [8], which might be due to the presence of tantalum in the alloy and its tendency to react with oxygen. The overall activation energy found for oxidation and sublimation at the lesser gas flow rate is lower than for the higher one because a thicker boundary layer can form around the sample which leads to a more diffusion controlled process, which is less susceptible to change due to temperature modifications. The accuracy of fit to the linear trend line is significantly higher and shows a strong tendency towards a better fit for the approach, which does not take the diffusion through the product layer into account for the samples oxidized in 10 l/min and 1 l/min gas flow rate respectively. This means that the gas velocities applied in these experiments were high enough in order to keep the gaseous product layer around the sample thin. Also the formed Mo oxide layer seems to be porous enough, so that the approach assuming a chemically controlled conversion of the material can explain the ongoing mechanisms leading to the change in weight of the sample. Both approaches however show relatively high accordance with the linear fit. The overall better fit of the approach not taking the diffusion into account is mostly due to the flat increase of the diffusion barrier in the beginning phase of each experiment, while the oxide layer is still building up. The conversion rates found in the oxidation experiments for the W-Re 25 samples were lower than the ones for the Mo-Ta samples. The determined overall activation energy was considerably higher than the ones found for lower temperatures in pure tungsten. This might be due to the ongoing sublimation process in W-Re samples. The overall accuracy of fit of the linear trend line was not as high as in the Mo-Ta samples, which probably can be explained by the observed periodic spalling of the oxidic layer.

5.2 Pilot experiments on various materials

The pilot experiments were conducted to investigate possible process parameters to separate different alloys into their components through oxidation and selective sublimation. For the experiments Mo-Ox 1-7 the influence of the temperature on the degree of separation between molybdenum and tungsten as well as the effect of the gas flow within the furnace and the process gas composition on the degree of conversion of the sample can be deducted. The results of the SEM-EDX analysis show, that no detectable amount of tungsten oxide sublimes and condenses in the filter bottle at temperatures of 900 °C and below. The increase of the gas

velocity raises the speed of conversion according to the literature (figure 2.3) [8]. When looking at experiments Mo-Ox 5 and Mo-Ox 7 which only differ in gas flow rate, the former, conducted with the lower gas throughput shows a slightly higher degree of conversion of the sample, however this does not contradict the literature since the experiments were run for a set amount of time, which by far exceeded the time necessary for a complete reaction with oxygen of the sample, hence no conclusion can be drawn concerning the oxidation rate. The Ar-O_2 process gas seems to inhibit the sublimation of MoO_3 since a considerable weight gain of the sample could be observed after the experiment. The steel pipe oxidized in the conditions present during the experiments and caused a contamination of the samples due to oxides spalling from the pipe and falling into the crucible. The higher gas flow rate lead to an uninhibited gas flow throughout the pipe, generating a small area, that was not blocked by sublimed material.

The conversion of the Mo-Ta resulted in a MoO_3 sublimate. The conducted SEM-EDX analysis showed no impurities within the substance. The best conversion rate could be achieved at 900 °C. However there were still 36 wt.-% Mo left in the crucible. An improved outcome could probably be achieved by increasing the oxygen content in the process gas or by raising the temperature. The attempt to create Mo hydroxides which might have a higher vapor pressure than molybdenum trioxide failed. No satisfactory degree of conversion could be achieved at temperatures lower, than the ones needed to sublime MoO_3. However, at 800 °C the formation of a liquid phase in the crucible could be observed, while oxidizing the Mo-Ta chips.
When oxidizing W-Re in synthetic air a minimum temperature of 900 °C is needed for a full conversion of the sample despite the postulated high vapor pressure of rhenium oxide at lower temperatures [34]. No tungsten oxide was detected in the sublimed rhenium oxide fraction by SEM-EDX or RFA analysis. In a partly converted sample oxidized at 500 and 600 °C there exists a gradient of rhenium as well as oxygen content in the oxide layer leading to the conclusion that the oxidation of the metallic surface takes place simultaneously to the slow evaporation of rhenium oxide out of the oxide layer during the conversion. When exposing a sample to synthetic air at 800 °C, no rhenium oxide can be detected by SEM-EDX in the oxide layer of the partly converted sample. The fastest conversion rates are achievable through a high oxygen content within the process gas. A co-sublimation of MoO_3 could be observed at 900 °C. In order to reduce the Mo oxide impurities in the rhenium oxide sublimate the temperature would have to be lowered, consequently also diminishing the rate of conversion of the rhenium.

When oxidizing a Mo-W sample at 900 °C a small amount of tungsten oxide is also sublimed as already discussed for experiments Mo Ox 1-7. The molybdenum-niobium sample showed a sublimate free of Nb-impurities that could be detected by SEM-EDX analysis, which means that a separation of the alloy into its components via oxidation is possible. The amount of molybdenum oxide in the niobium oxide fraction within the crucible could probably be reduced through optimization of the process parameters. The oxidation of the Mo-Cu alloy lead to a liquid phase, hence oxidizing the sample is not a suitable technique to withdraw copper from the alloy. The results of an alternative process are discussed below.

5.3 Separation of a Mo-Cu composite

The SEM/EDX analysis of the chips and distilled zinc from the experiment Mo-Cu 1 suggest a heterogeneous removal of the copper-content throughout the analyzed surface area, since its content varies between 1.3 wt.-% and 13 %. This could be due to localized oxidation of the material which inhibits the diffusion of copper into the zinc. The analyzed chip from the experiment Mo-Cu 3 shows a significant reduction of the copper content (1.3-5.3 wt.-% remaining within the chip). The composition at the edge of the chip suggests the formation of MoO_3 and some remaining zinc which could not be removed through distillation, probably also due to the formation of zinc oxide. The chip from experiment Mo-Cu 4 was cut in half in order to analyze the composition close to the surface as well as in the center of the chip. A gradient concerning the removal of copper within the chip could be observed from the center of the span towards the surface. The high zinc and oxygen contents in the center of the chip can be explained by the small width of the chip and the excitation volume of the SEM/EDX beam, which causes the simultaneous incitation of the center as well as the edge. The detected antimony can be explained by a contamination of the furnace by preceding experiments, whereas the origin of the measured lead content is unknown. A reduction of the copper content can be observed throughout the chip. The distilled zinc presents itself with a nickel content of unknown origin throughout all conducted experiments.

The remaining material surrounding the chips after the evaporation of the zinc contains about 30 wt.-% copper which proves the dissolution of copper in zinc. A detailed SEM analysis of particles suggests a coagulation of the copper, because locally up to 87 wt.-% copper can be detected. Also some remaining zinc, which probably oxidized despite the vacuum and therefore

could not be evaporated can be found in the remaining material.
Smaller grain sizes could improve and speed up the dissolution of copper in the zinc due to an enhancement of the volume to surface ratio. Alternatively a straight forward copper removal in vacuum should be pursued.

5.4 Optimizing process parameters for the conversion

The most important result from the experiments on optimizing the process parameters was the systematic investigation on the conditions which promote the formation of a noticeable liquid phase. As stated in the literature section, a thin liquid film of MoO_3 or of a MoO_2-MoO_3 eutectic forms as an intermediate layer in the course of the oxidation of molybdenum and sublimation of MoO_3. The appearance of noticeable amounts of liquid phase during the conversion of Mo-Ta samples most likely equals an autocatalytic effect where the diffusion within the liquid phase is higher than the sublimation rate of molybdenum trioxide, hence metallic material is oxidized and dissolved by the liquid phase. Due to this mechanism more and more melt arises, which continuously reduces the surface available for oxidation and sublimation. All experiments done with 60 vol.-% oxygen in the process gas formed a liquid that surrounded the grains right from the beginning. However it subsided after some oxidation circles. Lower oxygen content in the process gas leads to a later formation of the liquid phase when temperatures are low (approx. 850 °C) and the grain size is either on the upper or lower end of the grain sizes investigated (< 1 mm to > 6.3 mm).
The experiments conducted in order to optimize the oxidation time and residual Mo oxide in the tantalum fraction both showed a high susceptibility of temperature modifications. The oxidation time decreases with increasing temperature, whereas the residual Mo oxide content declines with rising temperatures. Higher oxygen content in the process gas seems to extend the oxidation time as well as residual Mo content within the tantalum fraction. At low oxygen content of the process gas, big grain sizes increase oxidation time as well as the Mo content in the residue which indicates a lower degree of conversion of the sample. The existence of a liquid phase at low temperatures drastically increases the oxidation time. The formation of the melt at every temperature when oxidizing with 60 vol.-% oxygen in the process gas is very likely the reason for the prolonged oxidation time at high oxygen concentrations in the gas flow. The displayed high residue Mo oxide content at low temperatures and small grain sizes is due

to the formation of a liquid Mo-Ta-O-phase, which keeps the Mo oxide from subliming.

5.5 Laboratory rotary kiln

The experiments in the laboratory kiln represent the first upscaling step. This chapter discusses the specifics of operating a different and bigger furnace as well as the quality of the products achieved by the conducted experiments. The appendix shows SEM images of the collected products after the experiments. They systematically differ in structure, despite their sometimes identical chemical composition. The MoO_3 from the filter bottle is the finest, presenting spheres in the small micrometer range (figure 6.23a and 6.24), whereas the sublimate that falls out of the kiln when taking it apart after cool down is much coarser with long, but thin particles as well as spheres (figure 6.23b). The material forming the blockage in the kiln consists of a web of acicular particles respectively whiskers (figure 6.23d).

5.5.1 Influence of grain size

Smaller particles in the center of the bed are cooler because the do not come in contact with the hot kiln wall as often, which leads to a temperature gradient within the bed. For an exothermic reaction this actually causes a positive effect concerning the homogeneity of conversion of the material. The heat transfer in an indirectly heated kiln runs from the kiln wall to the oven atmosphere and into the filling. In case of an exothermic reaction, heat is generated at the surface of the filling which consists, of bigger particles, if the bed is high enough for particles to segregate. These particles need more time to oxidize due to their size. If the filling degree does not suffice for particles to segregate, the smaller particles will convert and evaporate quickly, changing the grain size distribution throughout the kiln. The video analysis of the filling in experiment "‘D-Mo-Ta 11"’ shows periodic cascading with transversal movement.

5.5.2 Influence of the variation of process parameters on key process markers

This section discusses the influence of different process parameters. The most important ones are the temperature, the gas composition and flow rate as well as the residence time of the material within the kiln.

The formation of a MoO_3 blockage within the tube at the beginning of the heating zone in material flow direction proved to be very problematic for the conduction of a continuous process,

due to material being prevented from entering the heating zone and hence being reverted into the charging area and not being converted. Apart from the low output of product a blockage in the pipe also acts as a filter accumulating more and more particles from the gas stream until finally the pressure rises within the furnace, because the gas can no longer escape the furnace in a controlled manner. Increasing the gas volume per time in the pilot experiments prevented the pipe from being entirely blocked by sublimed material. This approach was also tested in the rotary kiln experiments. The gas flow rate was changed from 18 l/min to 32 l/min in experiments "'D-Mo-Ta 7"' and "'D-Mo-Ta 9"' respectively. Also the process gas consisted of oxygen enriched air of 34 vol.-% and 25 vol.-% O_2. Both process parameters lead to a blockage of the pipe during the experiment, so no significant influence of the gas volume per time in this range can be found. Increasing the gas volume to 50 l/min in experiments "'D-Mo-Ta 10"', "'D-Mo-Ta 12"' and "'D-Mo-Ta 13"' only resulted in a formation of a nose along the inner circumference of the kiln at the end of the heating zone in gas flow direction.

The amount of sublimate passing through the furnace, which is dependent on the amount of material charged into the furnace, the theoretical residence time and the degree of conversion of the material has an effect on the formation of a blockage. This can be deducted from looking at experiments "'D-Mo 1"', "'D-Mo 3"', "'D-Mo-Ta 4"' and "'D-Mo-Ta 5"'.

Raising the amount of oxygen in the process gas facilitates the formation of a blockage ('D-Mo-Ta 4"' bzw. "'D-Mo-Ta 7"', "'D-Mo-Ta 9"' and "'D-Mo-Ta 10"'). Experiment "'D-Mo-Ta 10"' confirms the assumption that a high gas flow rate and no addition oxygen in the process gas (air) prevents the blockage of the kiln. Further reduction of the oxygen content in the process gas to 15 vol.-% and 12 vol.-% in experiments "'D-Mo-Ta 15"' and "'D-Mo-Ta 16"' respectively however lead, despite the high gas volume stream of 50 l/min to a blockage in experiment "'D-Mo-Ta 15"'. The blockage was most likely formed during cool down, since no chips were reverted. A good degree of conversion could be achieved with a lowered amount of oxygen in the process gas, because a very small amount of material could be detected in the drop tank after the experiments.

Due to the Ti oxide layer a small degree of conversion of the material resulted in experiment "'D-Mo-Ti 18"', hence only a small amount of sublimate was produced which prevented the build up of a blockage despite the oxygen content of 15 vol.-% in the process gas. Every experiment conducted with the Mo-Ti alloy presented a very low degree of conversion of the material compared to pure molybdenum despite the small amount of titanium (0.5 wt.-%) in the

alloy. The formation of a titanium oxide layer, which prevents the conversion of the material, is likely.

The conversion of the tantalum chips runs from the outside inwards (figure 6.23c). Close to the metallic surface of the chip, the oxide layer contains a small amount of oxygen that increases with distance from the metallic surface, peaking close to the surface of the oxide layer. MoO_3 sublimes at the surface of the oxide layer, lowering the oxygen content within the oxidic layer.

When the conditions within the furnace promote the formation of the liquid phase on Mo-Ta chips as described in the section for optimization of the process parameters, the material sinters (figure 6.23e) within the kiln and forms big near-sphere shaped particles, which have a very low residence time because they just roll through and a very low specific surface exposed to the furnace atmosphere, which causes a very low degree of conversion (experiments "'D-Mo-Ta 5"'and "'D-Mo-Ta 9"'). The reintroduction of the ground sintered fraction into the furnace leads to a further conversion of the material ("'D-Mo-Ta 12"'). Within the sintered particle there seems to be a phase richer in molybdenum and one containing more tantalum which means a segregation due to the formation of the liquid phase is likely. To prevent the material from sintering smaller amounts of material were charged per batch in order to reduce the bed height, which only resulted in smaller sintered particles. In order to limit sintering, low temperatures and small grain sizes should be avoided within the furnace, since they promote the appearance of the liquid phase.

5.5.3 Influence of the process parameters on the purity of the products

The conducted analysis agree with the results from the pilot experiments that a Mo-Ta alloy can be separated into its components by forming MoO_3 and tantalum oxide. Pure chemical MoO_2 and MoO_3 were analyzed before conducting the SEM-EDX analysis on the sublimates. The analysis showed 22.1 wt.-% oxygen and 77.9 wt.-% molybdenum as well as 33.0 wt.-% oxygen and 67.0 wt.-% molybdenum respectively.

The sublimed and condensed MoO_3 exhibited a chemical composition of 24-34 wt.-% oxygen and 67-76 wt.-% molybdenum. The oxygen content in the process gas has no systematical influence on the composition of the sublimate. The sodium and potassium content within the residues is from the lubricant, sticking to the chips, despite them being washed before charged. Tungsten can be present in small amounts in the original alloy, only showing up in the analysis

after the conversion within the furnace. Copper contents are most likely introduced to the sample during the SEM-EDX analysis. The RFA and ICP analysis agree well and the latter shows contents between 15 and 1593 ppm tantalum as well as between 46 and 992 ppm tungsten in the sublimate. The sublimed oxides are MoO_3 and WoO_3 which was to be expected. The residue from the drop tank shows molybdenum contents as low as 40 wt.-% depending on the conversion degree of the sample, making an improvement desirable. The ICP analysis indicates very low values for tungsten and molybdenum in the tantalum oxide fraction, which does not seem plausible and makes an error in choosing the sample likely.

The molybdenum-titanium alloy seemed to contain some tungsten as well, which was oxidized and also sublimed along with the MoO_3 showing up as an impurity of around 0.1 wt-% to the latter according to SEM-EDX and RFA analysis.

The separation of the tungsten from the rhenium oxide had a very good output considering the low/not detectable amount of rhenium oxide in the drop tank by SEM-EDX. Also the sublimate, showed no tungsten oxide content in the filter bottle, however if present molybdenum oxide is partly co-sublimed under the conditions needed to evaporate rhenium oxide. If rhenium oxide can be found in the drop tank, the SEM images show, that this is due to rhenium oxide dust, that sticks to the tungsten oxide grains due to turbulent conditions within the kiln.

The conversion of pelletized Mo-W slurry resulted in a very good enrichment of the elements molybdenum as well as tungsten in the filter and drop tank fractions respectively. Due to the thermodynamic limitations, already established in previous experiments a complete separation of tungsten and molybdenum oxide could not be achieved. There was no systematic pattern to be found on how the process parameters and pellet characteristics influence the purity of the fractions which amounted to between 2.0-4.0 wt.-% molybdenum in the drop tank residue and 0.9-6.2 wt.-% tungsten in the filter fraction. Pelletizing the slurry prevented the process gas flow to take fine slurry particles out of the reaction zone before a conversion can take place.

5.6 Industrial rotary kiln experiments

The upscaling of the process parameters (gas flow rate, material throughput), using the ratio of the cross sections of the laboratory rotary kiln to that of the indirectly heated industrial rotary kiln worked satisfactorily. A stable process state could be achieved over a period of about 10 hours. However after cool down considerable damages to the kiln wall and the charging device were

detected. The analysis of the products from an experiment, simulating the conditions, showed the formation of ferromolybdenum as well as ferrotantalum. Most likely a thin film of liquid phase formed on the chips which reacted with the iron of the kiln generating ferromolybdenum and ferrotantalum, which was detected in the XRD analysis. The chips were connected to the inner wall of the kiln for a short time by the formed brittle ferromolybdenum. Due the movement of the bed the brittle ferromolybdenum broke lose from the kiln wall, leaving a small whole. This would explain the damage of the kiln wall and the high content of ferromolybdenum in the residue from the drop tank.

The second experiment ran stable over a period of 56 hours. The best output of MoO_3 as well as purity of the drop tank fraction could be achieved through increasing the natural gas and the air flow rate as well as by the addition of oxygen, which lead to an increase in temperature to about 1150 °C close to the burner and 950 °C at the end of the kiln (29.6 3:10). Due to the higher temperature not only the output was raised, but also the nose that formed at the end of the kiln in material flow direction evaporated again. The purity of the product seems within the range of the Plansee SE requirements for MoO_3. Lower impurity values could most likely be achieved through washing and drying of the input material. During cool down of the furnace conditions, which promote the formation of a liquid phase according to the experiments for optimization of the process parameters arose (temperatures around 850 °C and small grains) and enabled a liquid phase which infiltrated the refractory lining of the kiln. In order to prevent this in the future, the furnace needs to be completely empty before cooling it down. This could be achieved through flushing the kiln with ceramic particles before cooling the furnace.

6 Conclusion and Outlook

After the conduction and evaluation of the experiments presented in this thesis the introduction of a stable industrial recycling process of Mo-Ta alloy scrap seems very feasible and well investigated. Due to the high purity of the products as well as the satisfactory output, the recycling process should operate cost effectively. The risk for unforeseeable difficulties when designing an industrial kiln for recycling Mo-Ta scrap appears to be low because of the high degree of upscaling already conducted throughout the course of this thesis.

The separation of tungsten and rhenium through oxidation in a laboratory scale rotary kiln results in a high degree of purity of the fractions.

Molybdenum and tungsten as well as molybdenum and rhenium could not be separated by oxidation due to thermodynamic limitations. There is ongoing research in the course of this project which investigates the process parameters for the optimization of the conversion of a Mo-W 50 alloy. Special emphasis is put on deducting the factors which allow a maximum enrichment of these elements within the individual fractions. Abrasive slurry, consisting of partly oxidized molybdenum and tungsten dust could be converted by prior agglomeration and enriched phases were obtained. The agglomeration technique used for this abrasive slurry is adaptable to other types of refractory metal containing slurries.

An alternative approach was introduced for recycling a molybdenum copper alloy using a vacuum technique which significantly lowered the copper content in the Mo-Cu alloy.

Pilot experiments on the separation of molybdenum and niobium by oxidation were conducted on a Mo-Nb alloy in the course of this thesis. As this is an alloy with increasing applications, higher scrap quantities are expected in the future. Therefore a research project was launched to investigate the conversion behavior of the Mo-Nb alloy at different process conditions and also to evaluate the process parameters, which promote the formation of a liquid phase as observed in the conversion of a Mo-Ta alloy.

References

[1] Critical raw materials for the EU:. Internet: http://ec.europa.eu/enterprise/policies/raw-materials/files/docs/report-b_en.pdf, 2014 (accessed November 28, 2014).

[2] United States Geological Survey. Internet: http://minerals.usgs.gov/minerals/pubs/commodity/molybdenum/myb1-2013-molyb.pdf, 2015 (accessed August 31, 2015).

[3] International Molybdenum Association. Internet:http://www.imoa.info/molybdenum/molybdenum_market_information/global_production_use.php, 2015 (accessed August 31, 2015).

[4] Roskill Information Services. *Molybdenum: Market Outlook to 2014, 10th Edition*. London 2010.

[5] British Geological survey. Internet: http://www.bgs.ac.uk/downloads/start.cfm?id=2701, 2013 (accessed March 27, 2013).

[6] International Molybdenum Association. Internet: http://www.imoa.info/moly_uses/molybdenum_uses.php, 2013 (accessed March 28, 2013).

[7] Springer Materials The Landolt-Börnstein Database. Internet: http://www.springermaterials.com/docs/pdf/10522884_2076.html?queryterms="mo-o", 2014 (accessed December 1, 2014).

[8] K. Swars and L. Gmelin. *Molybdän: Ergänzungsband, Verbindungen mit Edelgasen, Wasserstoff und Sauerstoff. Wasserfreie Antimon-, Wismut- und Alkalimolybdate Teil B1*. Gmelins Handbuch der anorganischen Chemie. Springer, 1975.

[9] E.A. Gulbransen, K.F. Andrew, and F.A. Brassart. Oxidation of molybdenum 550 to 1700 °C. *Journal of the Electrochemical Society*, 110(9), 952-959, 1963.

[10] D.R. Schryer and G.D. Walberg. A theoretical and experimental investigation of the oxidation of molybdenum at temperatures at which its trioxide is volatile. Technical report, DTIC Document, 1966.

[11] E.S. Jones, C. Mosher, R. Speiser, and J.W. Spretnak. The oxidation of molybdenum. *Corrosion*, 14(1), 20-26, 1958.

[12] Parthasarathy T.A., Mendiratta M.G., and Dimiduk D.M. Oxidation mechanisms in mo-reinforced mo5sib2(t2)–mo3si alloys. *Acta Materialia*, 50(7), 225-232, 2002.

[13] E.A. Gulbransen and W.S. Wysong. Thin oxide films on molybdenum. *Transactions of the American Institute of Mining and Metallurgical Engineers*, 175, 628-644, 1948.

[14] K.M. Gorbounova and V.A. Arslambekov. *Proceeding 6. Reunion de la societe de chimie physique*, May 29-june 1 Paris.

[15] V.V. Andreeva and E.A. Alekseeva. Thin oxide films on titanium, zirconium, molybdenum and alloys of titanium. In *Doklady Akad. Nauk SSSR*, volume 134. Inst. of Physical Chemistry, the Academy of Sciences, USSR, 1960.

[16] H.J. Booss. Contribution to oxide formation on molybdenum. *changed to MTLLA*, 13, 1959.

[17] M. Simnad and A. Spilners. Kinetics and mechanism of the oxidation of molybdenum. *J. Metals*, 7, 1955.

[18] B. Lustman. Oxidation of molybdenum in air at 1100 to 1600 F. *Metal Progress*, 57, 629, 1950.

[19] V.P. Elyutin, T.G. Lenskaya, A. Yu, and V.P. Polyakov. Determination of diffusion coefficients of oxygen in metal oxides by the emf method. In *Soviet Physics Doklady*, volume 16, 581, 1971.

[20] V.S. Muzykantov, K.T. Cheshkova, and G.K. Boreskov. Anomalous temperature dependence of the mobility of oxygen in molybdenum oxide. Technical report, Inst. of Catalysis, Novosibirsk, USSR, 1972.

[21] Springer materials the landolt-börnstein database. Internet: http://materials.springer.com/downloads/track-required/true?path=%2Fassets%2Fsm_lbs%2F147%2Fsm_lbs_978-3-540-70692-2_2331%2Fsm_lbs_978-3-540-70692-2_2331.pdf, 2014 (accessed April 1, 2015).

[22] E. Rabald. Wolfram und molybdän. c. agte und j. vacek : 1959. akademie-verlag, berlin. *Materials and Corrosion*, 11(4), 255, 1960.

[23] E. Fluck, L. Gmelin, and Deutsche Chemische Gesellschaft und Gmelin-Institut für Anorganische Chemie und Grenzgebiete. *Wolfram Ergänzungsband B1: Die Systeme mit Edelgasen, Wasserstoff und Sauerstoff*. Verlag Chemie, 1978.

[24] E. Nachtigall. Eigenschaften von molybdan und wolfram bei niedrigen und mittleren temperaturen. *Zeitschrift für Metallkunde*, 43(1), 23-26, 1952.

[25] V.A. Arslambekov and K.M. Gorbunova. Kinetics of the oxide film formation on tungsten and molybdenum. In *Doklady Akad. Nauk SSSR*, volume 119. Inst. of Physics in Chemistry, Academy of Sciences, USSR, 1958.

[26] V.F. Rybalko, V.Y. Kolot, and Y.M. Fogel. Oxidation of tungsten at room temperature. Technical report, Physicotechnical Inst., Kharkov, 1969.

[27] E.A. Gulbransen and K.F. Andrew. Kinetics of the oxidation of pure tungsten from 500 to 1300 c. *Journal of The Electrochemical Society*, 107(7), 619-628, 1960.

[28] E. Gebert and R.J. Ackermann. Substoichiometry of tungsten trioxide; the crystal systems of wo3. 00, wo2. 98, and wo2. 96. *Inorganic Chemistry*, 5(1), 136-142, 1966.

[29] M. Becke-Goering, L. Gmelin, and Deutsche Chemische Gesellschaft und Gmelin-Institut für Anorganische Chemie und Grenzgebiete. *Wolfram Ergänzungsband B2: Oxide*. Verlag Chemie, 1979.

[30] G. Hagg and A. Magnéli. X-ray studies on molybdenum and tungsten oxides. *Arkiv for kemi mineralogi och geologi*, 19(1), 1945.

[31] M. Schiavello, F. Pepe, M. Cannizzaro, S. De Rossi, and R.J.D. Tilley. Adsorption of oxygen and propene over a series of tungsten oxides. *Zeitschrift für physikalische Chemie*, 106(1_2), 1977.

[32] V.G. Finikov and G.N. Zykova. Oxygen isotopic exchange in the systems wo3-o2 and na2w4o13-o. *Zhurnal Fizicheskoi Khimii (USSR) For English translation see Russ. J. Phys. Chem.(Engl. Transl.)*, 38, 1964.

[33] Springer Materials The Landolt-Börnstein Database. Internet: http://materials.springer.com/downloads/track-required/true?path=%2Fassets%2Fsm_lbs%2F085%2Fsm_lbs_978-3-540-70692-2_2311%2Fsm_lbs_978-3-540-70692-2_2311.pdf, 2014 (accessed April 1, 2015).

[34] B. Heshmatpour and R.E. McDonald. Recovery and refining of rhenium, tungsten and molybdenum from w-re, mo-re and other alloy scraps. *Journal of the Less Common Metals*, 86(0), 121-128, 1982.

[35] V.D. Drobot and Bukin V.I. Recycling of rhenium. *The minerals, metals and Materials Society*, 1997.

[36] US Bureau of mines. *Recovery of Rhenium from tungsten-rhenium alloy*. Report of investigations 7254. Us department of the interior, 1969.

[37] Springer Materials The Landolt-Börnstein Database. Internet: http://materials.springer.com/assets/sm_lbs/052/sm_lbs_978-3-540-37478-7_19/sm_lbs_978-3-540-37478-7_19.pdf?auth66=1427978345_70338b4a880880e1362f67c494d49224&ext=.pdf, 2014 (accessed April 1, 2015).

[38] A. Stergiou, Tsakiropoulos P., and Brown A. The intermediate and high-temperature oxidation behaviour of mo(si1–xalx)2 intermetallic alloys. *Intermetallics*, 5(1), 69-81, 1997.

[39] K. Chattopadhyay, R. Mitra, and K.K. Ray. Nonisothermal and isothermal oxidation behavior of nb-si-mo alloys. *Metallurgical and Materials Transactions*, 39(3), 577-592, 2008.

[40] Mendiratta M.G., Parthasarathy T.A., and Dimiduk D.M. Oxidation behavior of αmo–mo3si–mo5sib2 (t2) three phase system. *Intermetallics*, 10(3), 225-232, 2002.

[41] A.A. Sharif. Effects of re- and al-alloying on mechanical properties and high-temperature oxidation of mosi2. *Journal of Alloys and Compounds*, 518(0), 22-26, 2012.

[42] Stergiou A. and Tsakiropoulos P. The intermediate and high-temperature oxidation behaviour of (mo,x)si2 (x = w, ta) intermetallic alloys. *Intermetallics*, 5(2), 117-126, 1997.

[43] F. Habashi. *Principles of extractive metallurgy*, volume 1. CRC Press, 1969.

[44] J. Crank. Diffusion with rapid irreversible immobilization. *Transactions of the Faraday Society*, 53, 1083-1091, 1957.

[45] A.M. Ginstling and B.I. Brounshtein. Concerning the diffusion kinetics of reactions in spherical particles. *J. Appl. Chem. USSR*, 23(12), 1327-1338, 1950.

[46] Jain A. Kinetics of oxidation of boron powder. *Thermochimica Acta*, 514(1–2), 67-73, 2011.

[47] T. Ginsberg. *Dynamische Modellierung von Drehrohröfen*. Dissertation, Fakultät für Maschinenwesen der Rheinisch-Westfälischen technischen Hochschule Aachen, 2010.

[48] J. Mellmann. The transverse motion of solids in rotating cylinders—forms of motion and transition behavior. *Powder Technology*, 118(3), 251-270, 2001.

[49] E. Specht and J. Mellmann. Slumping–rolling transition of granular solids in rotary kilns. *Chemical Engineering Science*, 60(13), 3629-3636, 2005.

[50] A.A. Boateng and P.V. Barr. A thermal model for the rotary kiln including heat transfer within the bed. *International Journal of Heat and Mass Transfer*, 39(10), 2131-2147, 1996.

[51] P. Thammavong and M. Debacq. Experimental apparatus for studying heat transfer in externally heated rotary kilns. *Chemical Engineering and Technology*, 34(5), 2011.

[52] X.Y. Liu and E. Specht. Mean residence time and hold-up of solids in rotary kilns. *Chemical Engineering Science*, 61(15), 5176-5181, 2006.

[53] Heiligenstaedt. *Wärmetechnische Rechnungen für Industrieöfen*. Stahleisen, 4. edition, 1966.

[54] W.C. Saeman. Passage of solids through rotary kilns - factors affecting the time of passage. *Chemical Engineering Progress*, 47(10), 508-514, 1951.

[55] H. Krames and P. Croockewitt. The passage of granular solids through inclined rotary kilns. *Chemical Engineering Science*, 1(6), 259-265, 1952.

[56] D. Ablitzer and J.L. Houzelot. Experimental study of residence time, particle movement and bed depth profile in rotary kilns. *The Canadian Journal of Chemical Engineering*, 73(2), 173-180, 1995.

[57] Peace software. http://www.peacesoftware.de/einigewerte/luft.html, 2015 (accessed April 1, 2015).

[58] Springer Materials The Landolt-Börnstein Database. Internet: http://www.springermaterials.com/docs/pdf/10757413{_}23.html, 2014 (accessed April 1, 2015).

[59] W. Pietsch. Agglomeration processes: phenomena, technologies, equipment. 2002.

[60] G. Heinze. *Handbuch der Agglomerationstechnik*. Wiley-VCH, 2000.

[61] A. Hochfellner. Pelletieren von Molybdän-Wolfram Stäuben. Bachelor thesis, Montanuniversität Leoben, 2015.

[62] C. E. Mortimer, U. Müller, and J. Beck. *Chemie: Das Basiswissen der Chemie*. Georg Thieme Verlag, 2014.

[63] K. Schwister and V. Leven. *Verfahrenstechnik für Ingenieure: Ein Lehr-und Übungsbuch*. Carl Hanser Verlag GmbH Co KG, 2014.

List of Figures

List of Tables

Appendix

Oxidation kinetics

Table 6.1: ISO Mo-Ta 2, 900 °C, 10 l/min

Time [min]	Time [sec]	Weight [g]	R $(g_0 - g)/g_0$	W $Wo^{1/3} - W^{1/3}[g^{1/3}]$	$(2/g)^{2/3}Ct$ $[s \cdot cm^2 \cdot g^{-2/3}]$	$(2 \cdot C \cdot M \cdot t)/(\alpha \cdot \rho)$ [s]	$(0.5 - 1/3 \cdot R - 0.5 \cdot ((1-R)^{2/3})) \cdot a1^2$ $[cm^2]$
0	0	4.25	0.000	0.000	0.000	0.000	0.000
20	1200	3.99	0.061	0.034	80.975	0.017	0.021
40	2400	3.75	0.118	0.066	161.951	0.033	0.081
60	3600	3.57	0.160	0.091	242.926	0.050	0.153
80	4800	3.42	0.195	0.113	323.901	0.067	0.233
100	6000	3.25	0.235	0.139	404.876	0.083	0.345
120	7200	3.1	0.271	0.162	485.852	0.100	0.465
140	8400	2.95	0.306	0.186	566.827	0.117	0.606
160	9600	2.84	0.332	0.204	647.802	0.133	0.724
180	10800	2.69	0.367	0.229	728.777	0.150	0.906
200	12000	2.52	0.407	0.259	809.753	0.167	1.142
220	13200	2.43	0.428	0.275	890.728	0.183	1.281
240	14400	2.23	0.475	0.313	971.703	0.200	1.630
260	15600	2.19	0.485	0.321	1,052.678	0.217	1.706
280	16800	2.11	0.504	0.337	1,133.654	0.233	1.866
300	18000	1.96	0.539	0.368	1,214.629	0.250	2.194
320	19200	1.9	0.553	0.381	1,295.604	0.267	2.335
340	20400	1.82	0.572	0.399	1,376.579	0.283	2.534
360	21600	1.8	0.576	0.403	1,457.555	0.300	2.586
380	22800	1.8	0.576	0.403	1,538.530	0.317	2.586

Table 6.2: ISO Mo-Ta 3, 850 °C, 10 l/min

Time [min]	Time [sec]	Weight [g]	R $(g_0 - g)/g_0$	W $Wo^{1/3} - W^{1/3}[g^{1/3}]$	$(2/g)^{2/3}Ct$ $[s \cdot cm^2 \cdot g^{-2/3}]$	$(2 \cdot C \cdot M \cdot t)/(\alpha \cdot \rho)$ [s]	$(0.5 - 1/3 \cdot R - 0.5 \cdot ((1-R)^{2/3})) \cdot a1^2$ $[cm^2]$
0	0	4.52	0.000	0.000	0.000	0.000	0.000
20	1200	4.68	−0.035	−0.019	80.975	0.017	0.007
40	2400	4.85	−0.073	−0.039	161.951	0.035	0.029
60	3600	4.8	−0.062	−0.033	242.926	0.052	0.021
80	4800	4.74	−0.049	−0.026	323.901	0.070	0.013
100	6000	4.59	−0.015	−0.008	404.876	0.087	0.001
120	7200	4.52	0.000	0.000	485.852	0.105	0.000
140	8400	4.26	0.058	0.032	566.827	0.122	0.019
160	9600	4.2	0.071	0.040	647.802	0.140	0.029
180	10800	3.91	0.135	0.078	728.777	0.157	0.108
200	12000	3.5	0.226	0.135	809.753	0.174	0.316
220	13200	3.25	0.281	0.172	890.728	0.192	0.504
240	14400	3.19	0.294	0.181	971.703	0.209	0.557
260	15600	3.17	0.299	0.184	1,052.678	0.227	0.576
280	16800	3.15	0.303	0.188	1,133.654	0.244	0.594
300	18000	3	0.336	0.211	1,214.629	0.262	0.746
320	19200	3	0.336	0.211	1,295.604	0.279	0.746

Table 6.3: ISO Mo-Ta 10, 875 °C, 10 l/min

Time [min]	Time [sec]	Weight [g]	R $(g_0 - g)/g_0$	W $Wo^{1/3} - W^{1/3}[g^{1/3}]$	$(2/g)^{2/3}Ct$ $[s \cdot cm^2 \cdot g^{-2/3}]$	$(2 \cdot C \cdot M \cdot t)/(\alpha \cdot \rho)$ [s]	$(0.5 - 1/3 \cdot R - 0.5 \cdot ((1-R)^{2/3})) \cdot a1^2$ $[cm^2]$
0	0	4.36	0.000	0.000	0.000	0.000	0.000
20	1200	4.09	0.062	0.034	80.975	0.017	0.022
40	2400	3.9	0.106	0.060	161.951	0.034	0.065
60	3600	3.75	0.140	0.080	242.926	0.051	0.116
80	4800	3.5	0.197	0.115	323.901	0.068	0.238
100	6000	3.4	0.220	0.130	404.876	0.085	0.300
120	7200	3.28	0.248	0.148	485.852	0.102	0.385
140	8400	3.18	0.271	0.163	566.827	0.119	0.465
160	9600	3.08	0.294	0.179	647.802	0.136	0.555
180	10800	3.02	0.307	0.188	728.777	0.153	0.613
200	12000	2.91	0.333	0.206	809.753	0.171	0.728
220	13200	2.77	0.365	0.229	890.728	0.188	0.893
240	14400	2.68	0.385	0.245	971.703	0.205	1.009
260	15600	2.56	0.413	0.266	1,052.678	0.222	1.179
280	16800	2.43	0.443	0.289	1,133.654	0.239	1.382
300	18000	2.36	0.459	0.302	1,214.629	0.256	1.501
320	19200	2.24	0.486	0.325	1,295.604	0.273	1.719
340	20400	2.16	0.505	0.341	1,376.579	0.290	1.875
360	21600	2.05	0.530	0.363	1,457.555	0.307	2.106
380	22800	1.98	0.546	0.378	1,538.530	0.324	2.263
400	24000	1.96	0.550	0.382	1,619.505	0.341	2.310
420	25200	1.87	0.571	0.402	1,700.480	0.358	2.527
440	26400	1.87	0.571	0.402	1,781.456	0.375	2.527

Table 6.4: ISO Mo-Ta 12, 925 °C, 10 l/min

Time [min]	Time [sec]	Weight [g]	R $(g_0 - g)/g_0$	W $Wo^{1/3} - W^{1/3}[g^{1/3}]$	$(2/g)^{2/3}Ct$ $[s \cdot cm^2 \cdot g^{-2/3}]$	$(2 \cdot C \cdot M \cdot t)/(\alpha \cdot \rho)$ [s]	$(0.5 - 1/3 \cdot R - 0.5 \cdot ((1-R)^{2/3})) \cdot a1^2$ $[cm^2]$
0	0	6.38	0.000	0.000	0.000	0.000	0.000
20	1200	5.55	0.130	0.084	80.975	0.016	0.100
40	2400	5.01	0.215	0.144	161.951	0.033	0.284
60	3600	4.52	0.292	0.201	242.926	0.049	0.546
80	4800	4.16	0.348	0.246	323.901	0.065	0.804
100	6000	3.73	0.415	0.304	404.876	0.082	1.195
120	7200	3.44	0.461	0.345	485.852	0.098	1.517
140	8400	3.19	0.500	0.383	566.827	0.114	1.835
160	9600	2.89	0.547	0.430	647.802	0.131	2.275
180	10800	2.6	0.592	0.480	728.777	0.147	2.767
200	12000	2.36	0.630	0.523	809.753	0.163	3.232
220	13200	2.1	0.671	0.574	890.728	0.180	3.802
240	14400	2.01	0.685	0.593	971.703	0.196	4.018
260	15600	1.76	0.724	0.647	1,052.678	0.212	4.674
280	16800	1.54	0.759	0.700	1,133.654	0.229	5.329
300	18000	1.48	0.768	0.715	1,214.629	0.245	5.522
320	19200	1.48	0.768	0.715	1,295.604	0.261	5.522

Table 6.5: ISO Mo-Ta 13, 975 °C, 10 l/min

Time [min]	Time [sec]	Weight [g]	R $(g_0 - g)/g_0$	W $Wo^{1/3} - W^{1/3}[g^{1/3}]$	$(2/g)^{2/3}Ct$ $[s \cdot cm^2 \cdot g^{-2/3}]$	$(2 \cdot C \cdot M \cdot t)/(\alpha \cdot \rho)$ [s]	$(0.5 - 1/3 \cdot R - 0.5 \cdot ((1-R)^{2/3})) \cdot a1^2$ $[cm^2]$
0	0	5.5	0.000	0.000	0.000	0.000	0.000
20	1200	4.36	0.207	0.132	80.975	0.016	0.264
40	2400	3.6	0.345	0.233	161.951	0.031	0.792
80	4800	3.26	0.407	0.282	323.901	0.063	1.143
100	6000	2.64	0.520	0.383	404.876	0.078	2.014
120	7200	2.3	0.582	0.445	485.852	0.094	2.645
140	8400	1.86	0.662	0.535	566.827	0.110	3.669
160	9600	1.6	0.709	0.596	647.802	0.125	4.412
180	10800	1.36	0.753	0.657	728.777	0.141	5.211
200	12000	1.05	0.809	0.749	809.753	0.157	6.453
220	13200	0.91	0.835	0.796	890.728	0.173	7.113
240	14400	0.82	0.851	0.829	971.703	0.188	7.578
260	15600	0.76	0.862	0.853	1,052.678	0.204	7.909
280	16800	0.81	0.853	0.833	1,133.654	0.220	7.632

Table 6.6: ISO Mo-Ta 4, 900 °C, 1 l/min

Time [min]	Time [sec]	Weight [g]	R $(g_0 - g)/g_0$	W $Wo^{1/3} - W^{1/3}[g^{1/3}]$	$(2/g)^{2/3}Ct$ $[s \cdot cm^2 \cdot g^{-2/3}]$	$(2 \cdot C \cdot M \cdot t)/(\alpha \cdot \rho)$ [s]	$(0.5 - 1/3 \cdot R - 0.5 \cdot ((1-R)^{2/3})) \cdot a1^2$ $[cm^2]$
0	0	4.64	0.000	0.000	0.000	0.000	0.000
20	1200	3.97	0.144	0.084	80.975	0.017	0.124
40	2400	3.74	0.194	0.116	161.951	0.033	0.229
60	3600	3.81	0.179	0.106	242.926	0.050	0.194
80	4800	3.68	0.207	0.124	323.901	0.067	0.263
100	6000	3.63	0.218	0.131	404.876	0.083	0.292
120	7200	3.45	0.256	0.157	485.852	0.100	0.415
140	8400	3.12	0.328	0.207	566.827	0.117	0.704
160	9600	2.89	0.377	0.244	647.802	0.133	0.962
180	10800	2.77	0.403	0.264	728.777	0.150	1.117
200	12000	2.72	0.414	0.272	809.753	0.167	1.185
220	13200	2.57	0.446	0.298	890.728	0.183	1.407
240	14400	2.39	0.485	0.331	971.703	0.200	1.708
260	15600	2.2	0.526	0.367	1,052.678	0.217	2.069
280	16800	2.03	0.563	0.402	1,133.654	0.233	2.435
300	18000	1.83	0.606	0.445	1,214.629	0.250	2.923
320	19200	1.74	0.625	0.465	1,295.604	0.267	3.166
340	20400	1.66	0.642	0.484	1,376.579	0.283	3.394
360	21600	1.58	0.659	0.503	1,457.555	0.300	3.636
380	22800	1.64	0.647	0.489	1,538.530	0.317	3.453
400	24000	1.64	0.647	0.489	1,619.505	0.333	3.453

Table 6.7: ISO Mo-Ta 5, 950 °C, 1 l/min

Time [min]	Time [sec]	Weight [g]	R $(g_0 - g)/g_0$	W $Wo^{1/3} - W^{1/3}[g^{1/3}]$	$(2/g)^{2/3}Ct$ $[s \cdot cm^2 \cdot g^{-2/3}]$	$(2 \cdot C \cdot M \cdot t)/(\alpha \cdot \rho)$ [s]	$(0.5 - 1/3 \cdot R - 0.5 \cdot ((1-R)^{2/3})) \cdot a1^2$ $[cm^2]$
0	0	4.02	0.000	0.000	0.000	0.000	0.000
20	1200	3.81	0.052	0.028	80.975	0.016	0.016
40	2400	3.3	0.179	0.101	161.951	0.032	0.194
60	3600	2.83	0.296	0.176	242.926	0.048	0.565
80	4800	2.53	0.371	0.227	323.901	0.064	0.925
100	6000	2.19	0.455	0.291	404.876	0.080	1.474
120	7200	2.06	0.488	0.318	485.852	0.096	1.730
140	8400	1.73	0.570	0.390	566.827	0.112	2.511
160	9600	1.59	0.604	0.423	647.802	0.128	2.910
180	10800	1.39	0.654	0.474	728.777	0.144	3.561
200	12000	1.22	0.697	0.522	809.753	0.160	4.203
220	13200	1.05	0.739	0.574	890.728	0.176	4.943
240	14400	0.88	0.781	0.632	971.703	0.192	5.802
260	15600	0.78	0.806	0.670	1,052.678	0.208	6.377
280	16800	0.72	0.821	0.694	1,133.654	0.224	6.750
300	18000	0.71	0.823	0.698	1,214.629	0.240	6.814

Table 6.8: ISO Mo-Ta 6, 850 °C, 1 l/min

Time [min]	Time [sec]	Weight [g]	R $(g_0 - g)/g_0$	W $Wo^{1/3} - W^{1/3}[g^{1/3}]$	$(2/g)^{2/3}Ct$ $[s \cdot cm^2 \cdot g^{-2/3}]$	$(2 \cdot C \cdot M \cdot t)/(\alpha \cdot \rho)$ [s]	$(0.5 - 1/3 \cdot R - 0.5 \cdot ((1-R)^{2/3})) \cdot a1^2$ $[cm^2]$
0	0	5.18	0.000	0.000	0.000	0.000	0.000
20	1200	4.96	0.042	0.025	80.975	0.017	0.010
40	2400	5.36	−0.035	−0.020	161.951	0.035	0.007
60	3600	5.11	0.014	0.008	242.926	0.052	0.001
80	4800	4.97	0.041	0.024	323.901	0.070	0.009
100	6000	4.71	0.091	0.054	404.876	0.087	0.048
120	7200	4.55	0.122	0.073	485.852	0.105	0.087
140	8400	4.05	0.218	0.136	566.827	0.122	0.294
180	10800	4.09	0.210	0.131	728.777	0.157	0.272
200	12000	3.78	0.270	0.173	809.753	0.174	0.464
220	13200	3.6	0.305	0.198	890.728	0.192	0.603
240	14400	3.57	0.311	0.202	971.703	0.209	0.628
260	15600	3.58	0.309	0.200	1,052.678	0.227	0.619
280	16800	3.6	0.305	0.198	1,133.654	0.244	0.603

Table 6.9: ISO Mo-Ta 7, 875 °C, 1 l/min

Time [min]	Time [sec]	Weight [g]	R $(g_0 - g)/g_0$	W $Wo^{1/3} - W^{1/3}[g^{1/3}]$	$(2/g)^{2/3}Ct$ $[s \cdot cm^2 \cdot g^{-2/3}]$	$(2 \cdot C \cdot M \cdot t)/(\alpha \cdot \rho)$ [s]	$(0.5 - 1/3 \cdot R - 0.5 \cdot ((1-R)^{2/3})) \cdot a1^2$ $[cm^2]$
0	0	4.92	0.000	0.000	0.000	0.000	0.000
20	1200	4.53	0.079	0.046	80.975	0.017	0.036
40	2400	4.4	0.106	0.062	161.951	0.034	0.065
60	3600	4.31	0.124	0.073	242.926	0.051	0.090
80	4800	4.25	0.136	0.081	323.901	0.068	0.110
100	6000	4.19	0.148	0.089	404.876	0.085	0.131
120	7200	3.93	0.201	0.123	485.852	0.102	0.248
140	8400	3.71	0.246	0.153	566.827	0.119	0.379
160	9600	3.3	0.329	0.212	647.802	0.136	0.712
180	10800	2.95	0.400	0.267	728.777	0.153	1.100
200	12000	2.67	0.457	0.314	809.753	0.171	1.490
220	13200	2.54	0.484	0.336	890.728	0.188	1.698
240	14400	2.4	0.512	0.362	971.703	0.205	1.943
260	15600	2.37	0.518	0.368	1,052.678	0.222	1.999
280	16800	2.19	0.555	0.402	1,133.654	0.239	2.355
300	18000	2.08	0.577	0.424	1,214.629	0.256	2.594
320	19200	2.09	0.575	0.422	1,295.604	0.273	2.572
340	20400	2.09	0.575	0.422	1,376.579	0.290	2.572

Table 6.10: ISO Mo-Ta 8, 925 °C, 1 l/min

Time [min]	Time [sec]	Weight [g]	R $(g_0 - g)/g_0$	W $Wo^{1/3} - W^{1/3}[g^{1/3}]$	$(2/g)^{2/3}Ct$ $[s \cdot cm^2 \cdot g^{-2/3}]$	$(2 \cdot C \cdot M \cdot t)/(\alpha \cdot \rho)$ [s]	$(0.5 - 1/3 \cdot R - 0.5 \cdot ((1-R)^{2/3})) \cdot a1^2$ $[cm^2]$
0	0	5.76	0.000	0.000	0.000	0.000	0.000
20	1200	5.22	0.094	0.058	80.975	0.016	0.051
40	2400	4.73	0.179	0.114	161.951	0.033	0.193
60	3600	4.41	0.234	0.153	242.926	0.049	0.342
80	4800	4.1	0.288	0.192	323.901	0.065	0.533
100	6000	3.78	0.344	0.235	404.876	0.082	0.783
120	7200	3.49	0.394	0.276	485.852	0.098	1.062
140	8400	3.32	0.424	0.301	566.827	0.114	1.250
160	9600	3.15	0.453	0.327	647.802	0.131	1.459
180	10800	2.89	0.498	0.368	728.777	0.147	1.820
200	12000	2.77	0.519	0.388	809.753	0.163	2.006
220	13200	2.59	0.550	0.419	890.728	0.180	2.309
240	14400	2.39	0.585	0.456	971.703	0.196	2.682
260	15600	2.22	0.615	0.488	1,052.678	0.212	3.034
280	16800	2.17	0.623	0.498	1,133.654	0.229	3.143
300	18000	2.05	0.644	0.522	1,214.629	0.245	3.419
320	19200	1.91	0.668	0.552	1,295.604	0.261	3.766
340	20400	1.8	0.688	0.576	1,376.579	0.278	4.058
360	21600	1.75	0.696	0.587	1,457.555	0.294	4.197
380	22800	1.68	0.708	0.604	1,538.530	0.310	4.399
400	24000	1.68	0.708	0.604	1,619.505	0.327	4.399

Table 6.11: ISO Mo-Ta 14, 975 °C, 1 l/min

Time [min]	Time [sec]	Weight [g]	R $(g_0 - g)/g_0$	W $Wo^{1/3} - W^{1/3}[g^{1/3}]$	$(2/g)^{2/3}Ct$ $[s \cdot cm^2 \cdot g^{-2/3}]$	$(2 \cdot C \cdot M \cdot t)/(\alpha \cdot \rho)$ [s]	$(0.5 - 1/3 \cdot R - 0.5 \cdot ((1-R)^{2/3})) \cdot a1^2$ $[cm^2]$
0	0	4.67	0.000	0.000	0.000	0.000	0.000
20	1200	4.18	0.105	0.061	80.975	0.016	0.064
40	2400	3.92	0.161	0.095	161.951	0.031	0.155
60	3600	3.56	0.238	0.145	242.926	0.047	0.352
80	4800	3.26	0.302	0.189	323.901	0.063	0.589
100	6000	2.9	0.379	0.245	404.876	0.078	0.973
120	7200	2.58	0.448	0.300	485.852	0.094	1.418
140	8400	2.29	0.510	0.353	566.827	0.110	1.920
160	9600	2.08	0.555	0.395	647.802	0.125	2.352
180	10800	2.01	0.570	0.409	728.777	0.141	2.511
200	12000	1.7	0.636	0.478	809.753	0.157	3.310
220	13200	1.49	0.681	0.529	890.728	0.173	3.956
240	14400	1.28	0.726	0.586	971.703	0.188	4.705
260	15600	1.14	0.756	0.627	1,052.678	0.204	5.274
280	16800	1.07	0.771	0.649	1,133.654	0.220	5.582

W-Re

Table 6.12: ISO W-Re 7, 900 °C, 10 l/min, 90 % O_2, 10 % N_2

Time [min]	Time [sec]	Weight [g]	R $(g_0-g)/g_0$	W $Wo^{1/3}-W^{1/3}[g^{1/3}]$	$(2/g)^{2/3}Ct$ $[s\cdot cm^2\cdot g^{-2/3}]$	$(2\cdot C\cdot M\cdot t)/(\alpha\cdot\rho)$ [s]	$(0.5-1/3\cdot R-0.5\cdot((1-R)^{2/3}))\cdot a1^2$ $[cm^2]$
0	0	10.64	0.000	0.000	0.000	0.000	0.000
20	1200	10.53	0.010	0.008	234.837	0.060	0.001
40	2400	10.48	0.015	0.011	469.673	0.120	0.001
60	3600	10.44	0.019	0.014	704.510	0.180	0.002

Table 6.13: ISO W-Re 8, 850 °C, 10 l/min, 90 % O_2, 10 % N_2

Time [min]	Time [sec]	Weight [g]	R $(g_0-g)/g_0$	W $Wo^{1/3}-W^{1/3}[g^{1/3}]$	$(2/g)^{2/3}Ct$ $[s\cdot cm^2\cdot g^{-2/3}]$	$(2\cdot C\cdot M\cdot t)/(\alpha\cdot\rho)$ [s]	$(0.5-1/3\cdot R-0.5\cdot((1-R)^{2/3}))\cdot a1^2$ $[cm^2]$
0	0	9.05	0.000	0.000	0.000	0.000	0.000
20	1200	8.88	0.019	0.013	234.837	0.063	0.002
40	2400	8.94	0.012	0.008	469.673	0.125	0.001
60	3600	8.93	0.013	0.009	704.510	0.188	0.001
80	4800	8.91	0.015	0.011	939.346	0.250	0.001
100	6000	8.9	0.017	0.012	1,174.183	0.313	0.002
120	7200	8.87	0.020	0.014	1,409.019	0.376	0.002
140	8400	8.86	0.021	0.015	1,643.856	0.438	0.002
160	9600	8.83	0.024	0.017	1,878.693	0.501	0.003

Table 6.14: ISO W-Re 9, 950 °C, 10 l/min, 90 % O_2, 10 % N_2

Time [min]	Time [sec]	Weight [g]	R $(g_0-g)/g_0$	W $Wo^{1/3}-W^{1/3}[g^{1/3}]$	$(2/g)^{2/3}Ct$ $[s\cdot cm^2\cdot g^{-2/3}]$	$(2\cdot C\cdot M\cdot t)/(\alpha\cdot\rho)$ [s]	$(0.5-1/3\cdot R-0.5\cdot((1-R)^{2/3}))\cdot a1^2$ $[cm^2]$
0	0	9.57	0.000	0.000	0.000	0.000	0.000
20	1200	9.43	0.015	0.010	234.837	0.057	0.001
40	2400	9.3	0.028	0.020	469.673	0.115	0.004
60	3600	9.2	0.039	0.028	704.510	0.172	0.008
80	4800	9.05	0.054	0.039	939.346	0.230	0.017
100	6000	8.99	0.061	0.044	1,174.183	0.287	0.021
120	7200	8.92	0.068	0.049	1,409.019	0.345	0.026
140	8400	8.83	0.077	0.056	1,643.856	0.402	0.034

Table 6.15: ISO W-Re 10, 925 °C, 10 l/min, 90 % O_2, 10 % N_2

Time [min]	Time [sec]	Weight [g]	R $(g_0-g)/g_0$	W $Wo^{1/3}-W^{1/3}[g^{1/3}]$	$(2/g)^{2/3}Ct$ $[s\cdot cm^2\cdot g^{-2/3}]$	$(2\cdot C\cdot M\cdot t)/(\alpha\cdot\rho)$ [s]	$(0.5-1/3\cdot R-0.5\cdot((1-R)^{2/3}))\cdot a1^2$ $[cm^2]$
0	0	5.83	0.000	0.000	0.000	0.000	0.000
20	1200	5.69	0.024	0.015	234.837	0.059	0.003
40	2400	5.63	0.034	0.021	469.673	0.117	0.007
60	3600	5.56	0.046	0.028	704.510	0.176	0.012
80	4800	5.56	0.046	0.028	939.346	0.235	0.012
100	6000	5.43	0.069	0.042	1,174.183	0.293	0.027
120	7200	5.42	0.070	0.043	1,409.019	0.352	0.028
140	8400	5.34	0.084	0.052	1,643.856	0.411	0.041
160	9600	5.25	0.099	0.062	1,878.693	0.470	0.058
180	10800	5.28	0.094	0.058	2,113.529	0.528	0.052
200	12000	5.28	0.094	0.058	2,348.366	0.587	0.052
220	13200	5.22	0.105	0.065	2,583.202	0.646	0.064
240	14400	5.21	0.106	0.066	2,818.039	0.704	0.066
260	15600	5.21	0.106	0.066	3,052.876	0.763	0.066
280	16800	5.21	0.106	0.066	3,287.712	0.822	0.066

Table 6.16: ISO W-Re 11, 875 °C, 10 l/min, 90 % O_2, 10 % N_2

Time [min]	Time [sec]	Weight [g]	R $(g_0-g)/g_0$	W $Wo^{1/3}-W^{1/3}[g^{1/3}]$	$(2/g)^{2/3}Ct$ $[s\cdot cm^2\cdot g^{-2/3}]$	$(2\cdot C\cdot M\cdot t)/(\alpha\cdot\rho)$ [s]	$(0.5-1/3\cdot R-0.5\cdot((1-R)^{2/3}))\cdot a1^2$ $[cm^2]$
0	0	8.98	0.000	0.000	0.000	0.000	0.000
20	1200	8.93	0.006	0.004	234.837	0.061	0.000
40	2400	8.89	0.010	0.007	469.673	0.122	0.001
60	3600	8.88	0.011	0.008	704.510	0.184	0.001
80	4800	8.88	0.011	0.008	939.346	0.245	0.001
100	6000	8.88	0.011	0.008	1,174.183	0.306	0.001
120	7200	8.88	0.011	0.008	1,409.019	0.367	0.001
140	8400	8.8	0.020	0.014	1,643.856	0.429	0.002
160	9600	8.78	0.022	0.016	1,878.693	0.490	0.003
180	10800	8.76	0.024	0.017	2,113.529	0.551	0.003
203	12180	8.75	0.026	0.018	2,383.591	0.622	0.004
223	13380	8.71	0.030	0.021	2,618.428	0.683	0.005
243	14580	8.7	0.031	0.022	2,853.264	0.744	0.005
263	15780	8.68	0.033	0.023	3,088.101	0.805	0.006
283	16980	8.67	0.035	0.024	3,322.938	0.867	0.007
309	18540	8.64	0.038	0.027	3,628.225	0.946	0.008
334	20040	8.6	0.042	0.030	3,921.771	1.023	0.010
354	21240	8.58	0.045	0.031	4,156.607	1.084	0.011

Table 6.17: ISO W-Re 4, 850 °C, 3 l/min, 100 % O_2

Time [min]	Time [sec]	Weight [g]	R $(g_0 - g)/g_0$	W $Wo^{1/3} - W^{1/3}[g^{1/3}]$	$(2/g)^{2/3}Ct$ $[s \cdot cm^2 \cdot g^{-2/3}]$	$(2 \cdot C \cdot M \cdot t)/(\alpha \cdot \rho)$ [s]	$(0.5 - 1/3 \cdot R - 0.5 \cdot ((1 - R)^{2/3})) \cdot a1^2$ $[cm^2]$
0	0	9.85	0.000	0.000	0.000	0.000	0.000
40	2400	9.73	0.012	0.009	521.859	0.139	0.001
60	3600	9.77	0.008	0.006	782.789	0.209	0.000
80	4800	9.86	−0.001	−0.001	1,043.718	0.278	5.723×10^{-06}
100	6000	9.98	−0.013	−0.009	1,304.648	0.348	0.001
120	7200	9.98	−0.013	−0.009	1,565.577	0.417	0.001
140	8400	10.02	−0.017	−0.012	1,826.507	0.487	0.002
160	9600	10.04	−0.019	−0.014	2,087.436	0.557	0.002
180	10800	10.04	−0.019	−0.014	2,348.366	0.626	0.002
200	12000	10	−0.015	−0.011	2,609.295	0.696	0.001
220	13200	9.95	−0.010	−0.007	2,870.225	0.765	0.001
240	14400	9.93	−0.008	−0.006	3,131.154	0.835	0.000
260	15600	9.91	−0.006	−0.004	3,392.084	0.904	0.000
280	16800	9.82	0.003	0.002	3,653.013	0.974	5.160×10^{-05}
300	18000	9.76	0.009	0.007	3,913.943	1.043	0.000
320	19200	9.76	0.009	0.007	4,174.873	1.113	0.000
340	20400	9.84	0.001	0.001	4,435.802	1.183	5.729×10^{-06}
360	21600	9.53	0.032	0.023	4,696.732	1.252	0.006
395	23700	9.65	0.020	0.015	5,153.358	1.374	0.002
415	24900	9.57	0.028	0.021	5,414.288	1.443	0.005
435	26100	9.62	0.023	0.017	5,675.217	1.513	0.003
455	27300	9.63	0.022	0.016	5,936.147	1.583	0.003
475	28500	9.73	0.012	0.009	6,197.076	1.652	0.001
495	29700	9.82	0.003	0.002	6,458.006	1.722	5.160×10^{-05}
515	30900	9.81	0.004	0.003	6,718.935	1.791	9.178×10^{-05}
535	32100	9.76	0.009	0.007	6,979.865	1.861	0.000
555	33300	9.71	0.014	0.010	7,240.795	1.930	0.001
575	34500	9.69	0.016	0.012	7,501.724	2.000	0.001
595	35700	9.66	0.019	0.014	7,762.654	2.070	0.002
615	36900	9.65	0.020	0.015	8,023.583	2.139	0.002
635	38100	9.64	0.021	0.015	8,284.513	2.209	0.003
655	39300	9.65	0.020	0.015	8,545.442	2.278	0.002
675	40500	9.71	0.014	0.010	8,806.372	2.348	0.001
695	41700	9.68	0.017	0.012	9,067.301	2.417	0.002
715	42900	9.7	0.015	0.011	9,328.231	2.487	0.001
735	44100	9.7	0.015	0.011	9,589.160	2.556	0.001

Table 6.18: ISO W-Re 5, 950 °C, 3 l/min, 100 % O_2

Time [min]	Time [sec]	Weight [g]	R $(g_0 - g)/g_0$	W $Wo^{1/3} - W^{1/3}[g^{1/3}]$	$(2/g)^{2/3}Ct$ $[s \cdot cm^2 \cdot g^{-2/3}]$	$(2 \cdot C \cdot M \cdot t)/(\alpha \cdot \rho)$ [s]	$(0.5 - 1/3 \cdot R - 0.5 \cdot ((1 - R)^{2/3})) \cdot a1^2$ $[cm^2]$
0	0	11.2	0.000	0.000	0.000	0.000	0.000
20	1200	11.07	0.012	0.009	260.930	0.064	0.001
40	2400	11.16	0.004	0.003	521.859	0.128	7.097×10^{-05}
60	3600	11.19	0.001	0.001	782.789	0.192	4.431×10^{-06}
80	4800	11.22	−0.002	−0.001	1,043.718	0.256	1.770×10^{-05}
100	6000	11.31	−0.010	−0.007	1,304.648	0.319	0.001
120	7200	11.24	−0.004	−0.003	1,565.577	0.383	7.075×10^{-05}
140	8400	11.14	0.005	0.004	1,826.507	0.447	0.000
160	9600	11.04	0.014	0.011	2,087.436	0.511	0.001
180	10800	10.99	0.019	0.014	2,348.366	0.575	0.002
200	12000	10.96	0.021	0.016	2,609.295	0.639	0.003
220	13200	10.95	0.022	0.017	2,870.225	0.703	0.003
240	14400	10.96	0.021	0.016	3,131.154	0.767	0.003
260	15600	10.97	0.021	0.015	3,392.084	0.830	0.002
280	16800	11	0.018	0.013	3,653.013	0.894	0.002

Table 6.19: ISO W-Re 6, 1000 °C, 3 l/min, 100 % O_2

Time [min]	Time [sec]	Weight [g]	R $(g_0 - g)/g_0$	W $Wo^{1/3} - W^{1/3}[g^{1/3}]$	$(2/g)^{2/3}Ct$ $[s \cdot cm^2 \cdot g^{-2/3}]$	$(2 \cdot C \cdot M \cdot t)/(\alpha \cdot \rho)$ [s]	$(0.5 - 1/3 \cdot R - 0.5 \cdot ((1 - R)^{2/3})) \cdot a1^2$ $[cm^2]$
0	0	8.8	0.000	0.000	0.000	0.000	0.000
20	1200	8.63	0.019	0.013	260.930	0.061	0.002
40	2400	8.63	0.019	0.013	521.859	0.123	0.002
60	3600	8.67	0.015	0.010	782.789	0.184	0.001
80	4800	8.7	0.011	0.008	1,043.718	0.245	0.001
100	6000	8.67	0.015	0.010	1,304.648	0.307	0.001
120	7200	8.63	0.019	0.013	1,565.577	0.368	0.002
140	8400	8.68	0.014	0.009	1,826.507	0.430	0.001
160	9600	8.67	0.015	0.010	2,087.436	0.491	0.001
180	10800	8.63	0.019	0.013	2,348.366	0.552	0.002
200	12000	8.63	0.019	0.013	2,609.295	0.614	0.002
220	13200	8.63	0.019	0.013	2,870.225	0.675	0.002
240	14400	8.63	0.019	0.013	3,131.154	0.736	0.002

Optimization of process parameters

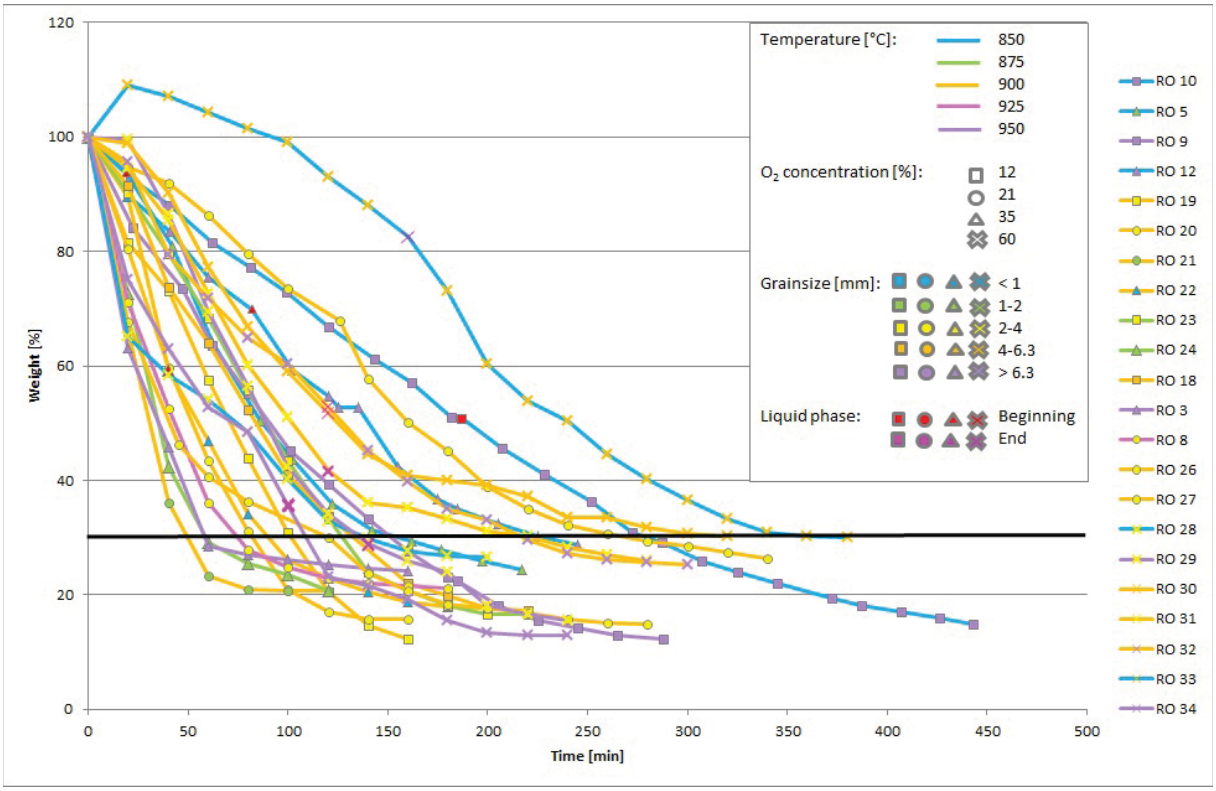

Figure 6.1: Results of gravimetric experiments for optimizing process parameters

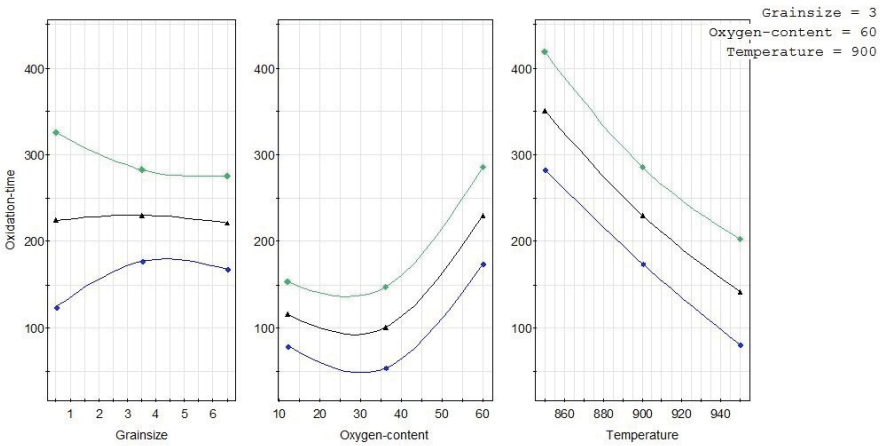

Figure 6.2: Prediction plot according to the model on the oxidation time for a conversion degree of 70 wt.-%, temperature ... [°C], oxygen content of process gas ... [vol.-%], grain size ... [mm]

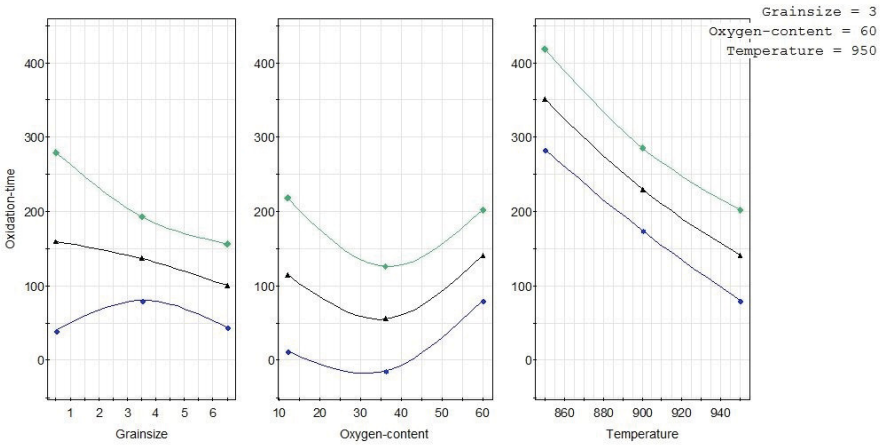

Figure 6.3: Prediction plot according to the model on the oxidation time for a conversion degree of 70 wt.-%, temperature ... [°C], oxygen content of process gas ... [vol.-%], grain size ... [mm]

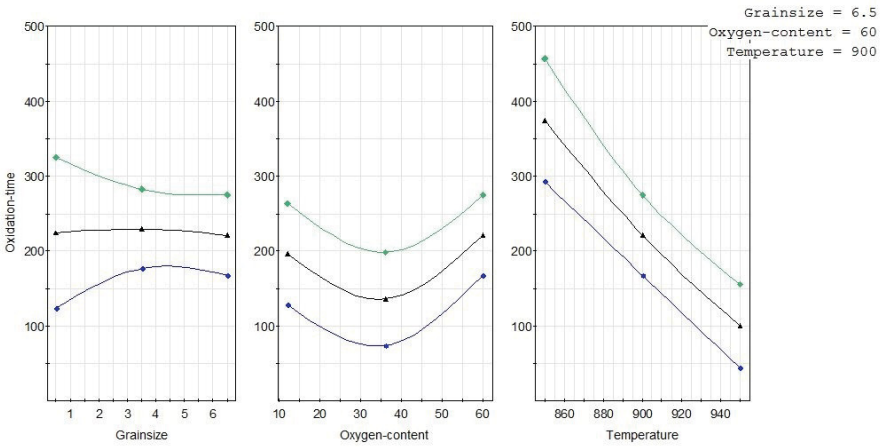

Figure 6.4: Prediction plot according to the model on the oxidation time for a conversion degree of 70 wt.-%, temperature ... [°C], oxygen content of process gas ... [vol.-%], grain size ... [mm]

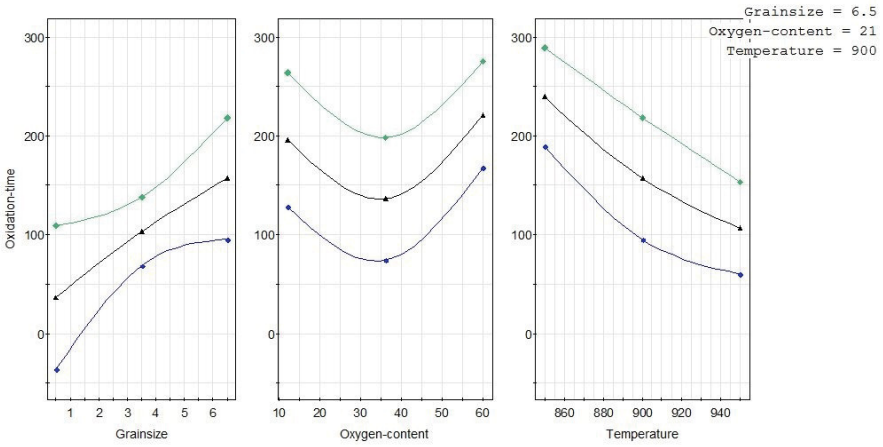

Figure 6.5: Prediction plot according to the model on the oxidation time for a conversion degree of 70 wt.-%, temperature ... [°C], oxygen content of process gas ... [vol.-%], grain size ... [mm]

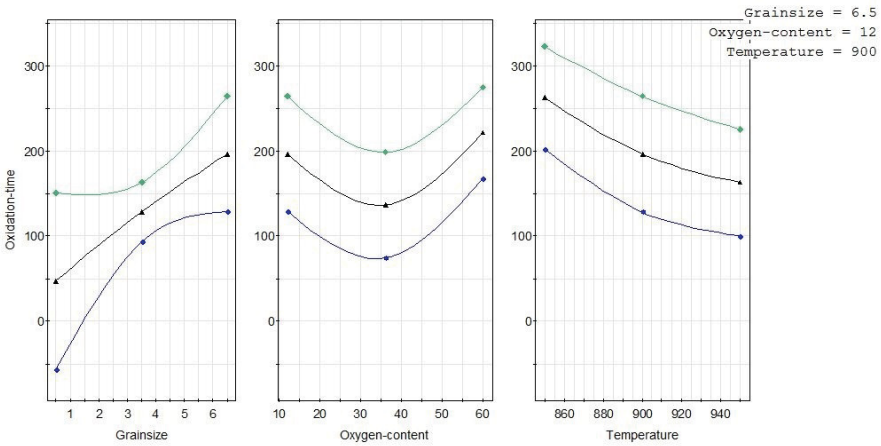

Figure 6.6: Prediction plot according to the model on the oxidation time for a conversion degree of 70 wt.-%, temperature ... [°C], oxygen content of process gas ... [vol.-%], grain size ... [mm]

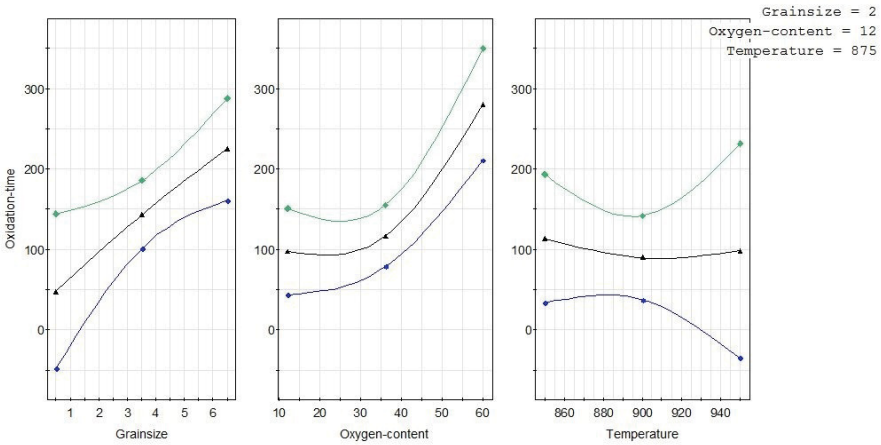

Figure 6.7: Prediction plot according to the model on the oxidation time for a conversion degree of 70 wt.-%, temperature ... [°C], oxygen content of process gas ... [vol.-%], grain size ... [mm]

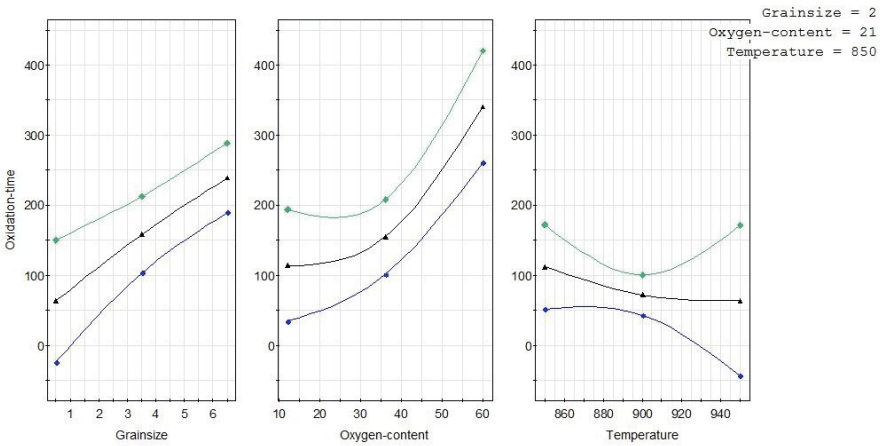

Figure 6.8: Prediction plot according to the model on the oxidation time for a conversion degree of 70 wt.-%, temperature ... [°C], oxygen content of process gas ... [vol.-%], grain size ... [mm]

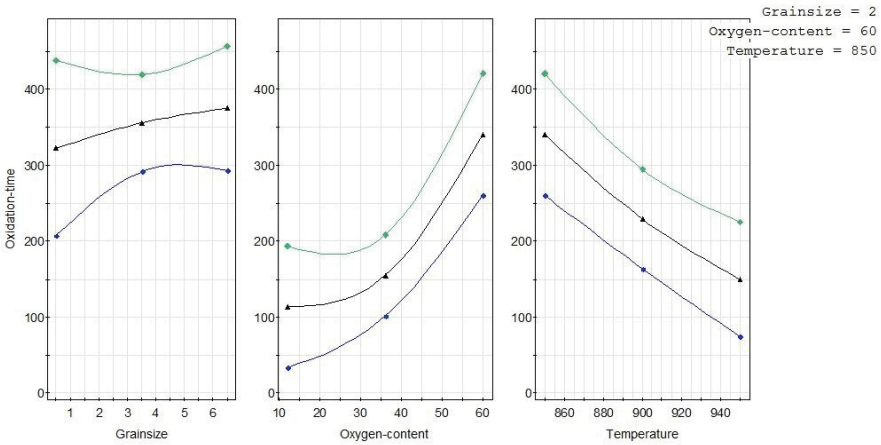

Figure 6.9: Prediction plot according to the model on the oxidation time for a conversion degree of 70 wt.-%, temperature ... [°C], oxygen content of process gas ... [vol.-%], grain size ... [mm]

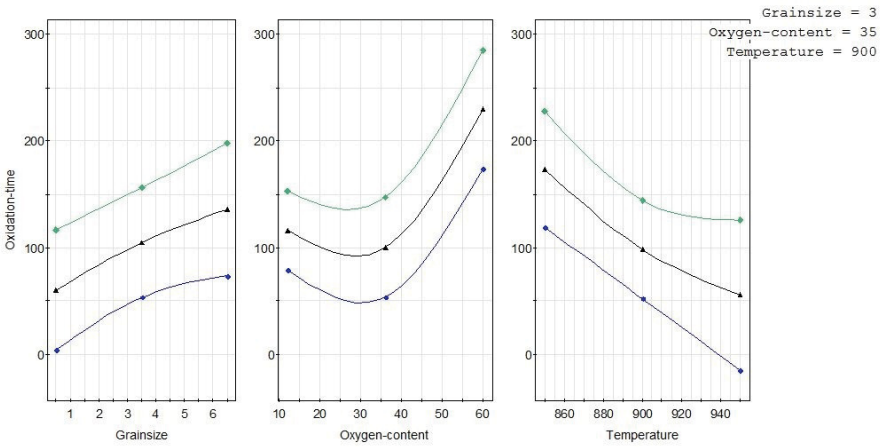

Figure 6.10: Prediction plot according to the model on the oxidation time for a conversion degree of 70 wt.-%, temperature . . . [°C], oxygen content of process gas . . . [vol.-%], grain size . . . [mm]

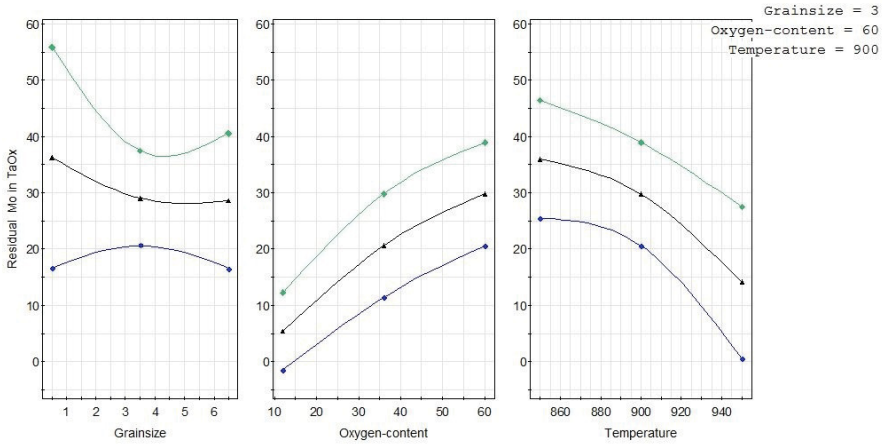

Figure 6.11: Prediction plot according to the model on the residual Mo content in the oxidic tantalum fraction, temperature ... [°C], oxygen content of process gas ... [vol.-%], grain size ... [mm]

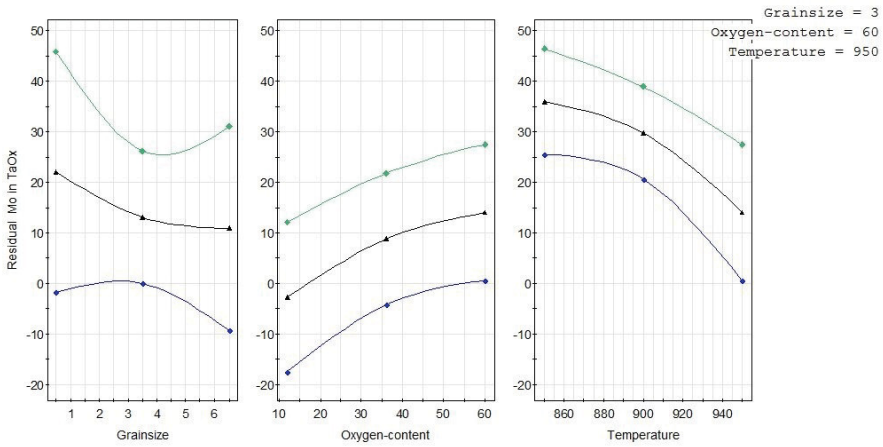

Figure 6.12: Prediction plot according to the model on the residual Mo content in the oxidic tantalum fraction, temperature ... [°C], oxygen content of process gas ... [vol.-%], grain size ... [mm]

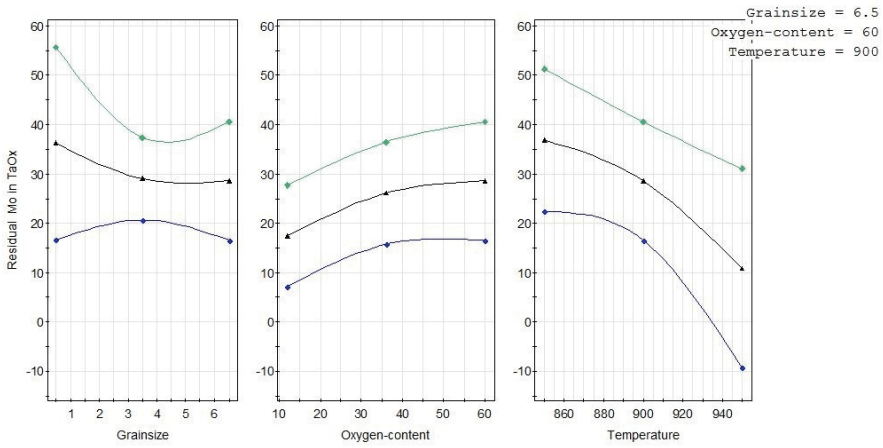

Figure 6.13: Prediction plot according to the model on the residual Mo content in the oxidic tantalum fraction, temperature ... [°C], oxygen content of process gas ... [vol.-%], grain size ... [mm]

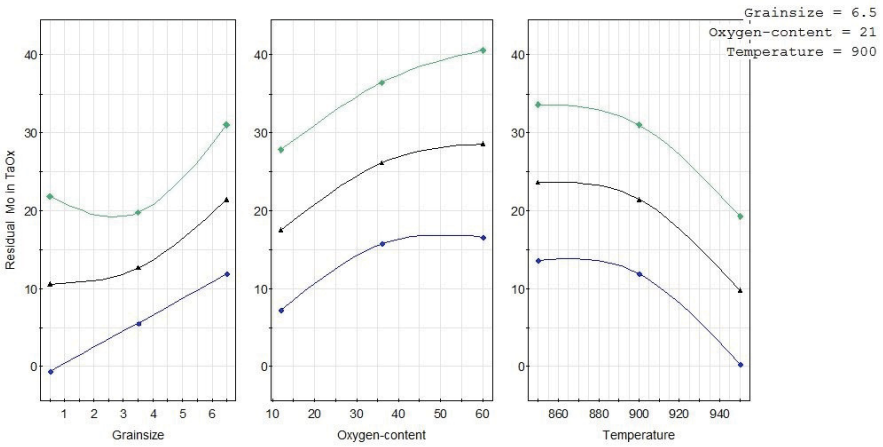

Figure 6.14: Prediction plot according to the model on the residual Mo content in the oxidic tantalum fraction, temperature ... [°C], oxygen content of process gas ... [vol.-%], grain size ... [mm]

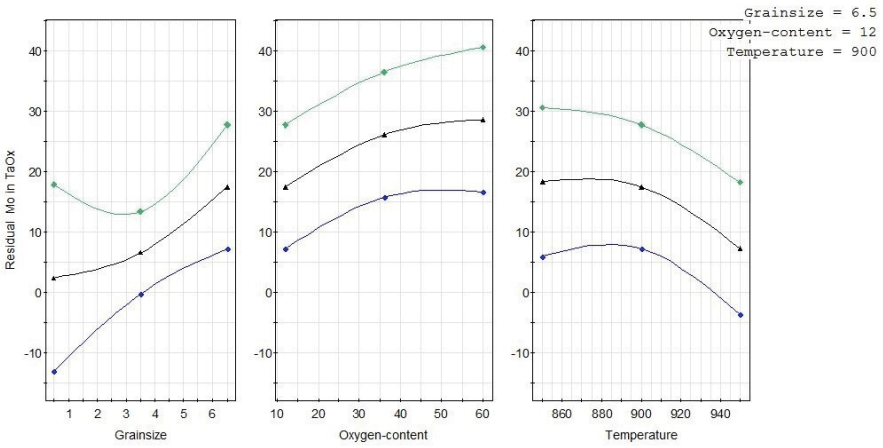

Figure 6.15: Prediction plot according to the model on the residual Mo content in the oxidic tantalum fraction, temperature ... [°C], oxygen content of process gas ... [vol.-%], grain size ... [mm]

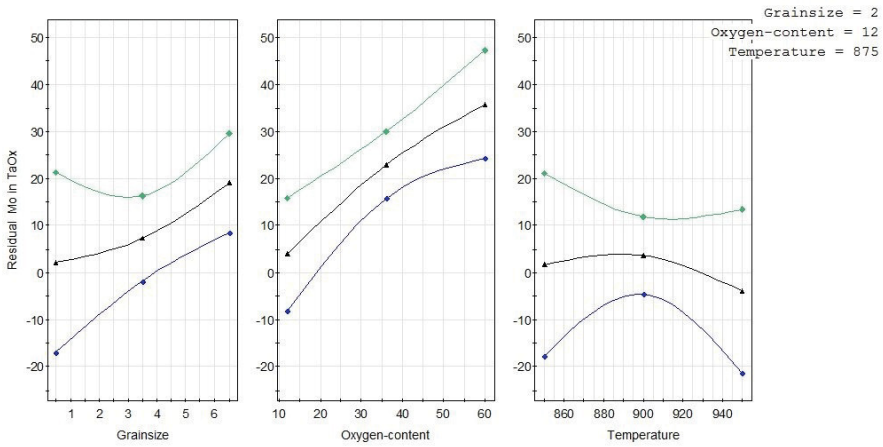

Figure 6.16: Prediction plot according to the model on the residual Mo content in the oxidic tantalum fraction, temperature ... [°C], oxygen content of process gas ... [vol.-%], grain size ... [mm]

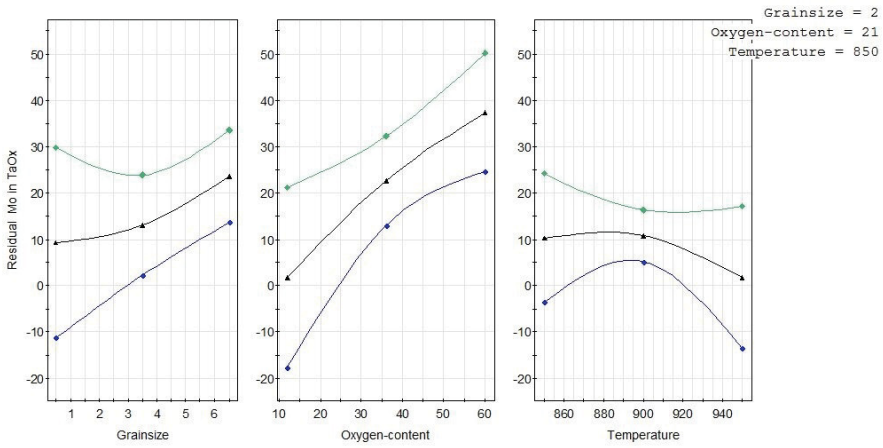

Figure 6.17: Prediction plot according to the model on the residual Mo content in the oxidic tantalum fraction, temperature ... [°C], oxygen content of process gas ... [vol.-%], grain size ... [mm]

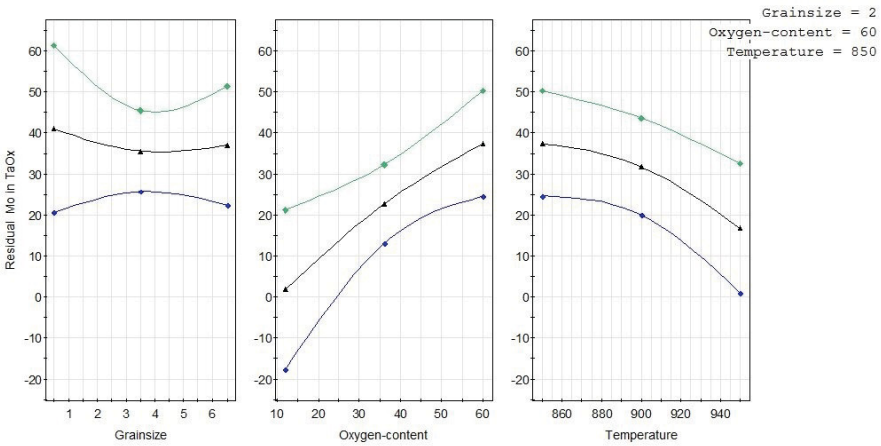

Figure 6.18: Prediction plot according to the model on the residual Mo content in the oxidic tantalum fraction, temperature ... [°C], oxygen content of process gas ... [vol.-%], grain size ... [mm]

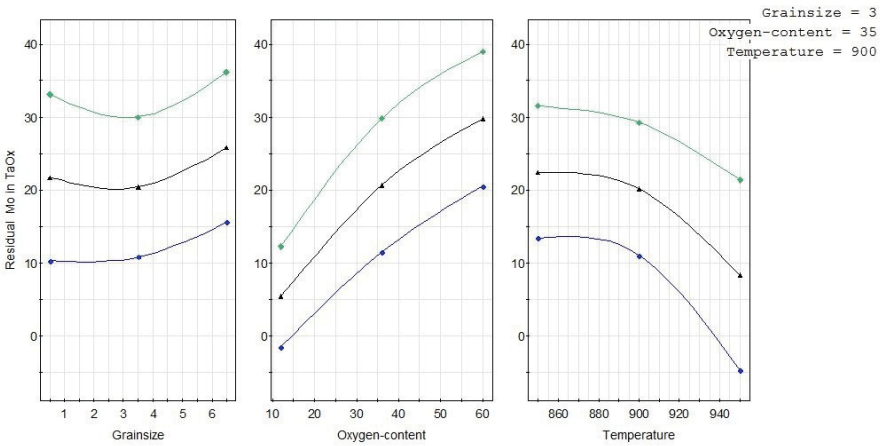

Figure 6.19: Prediction plot according to the model on the residual Mo content in the oxidic tantalum fraction, temperature ... [°C], oxygen content of process gas ... [vol.-%], grain size ... [mm]

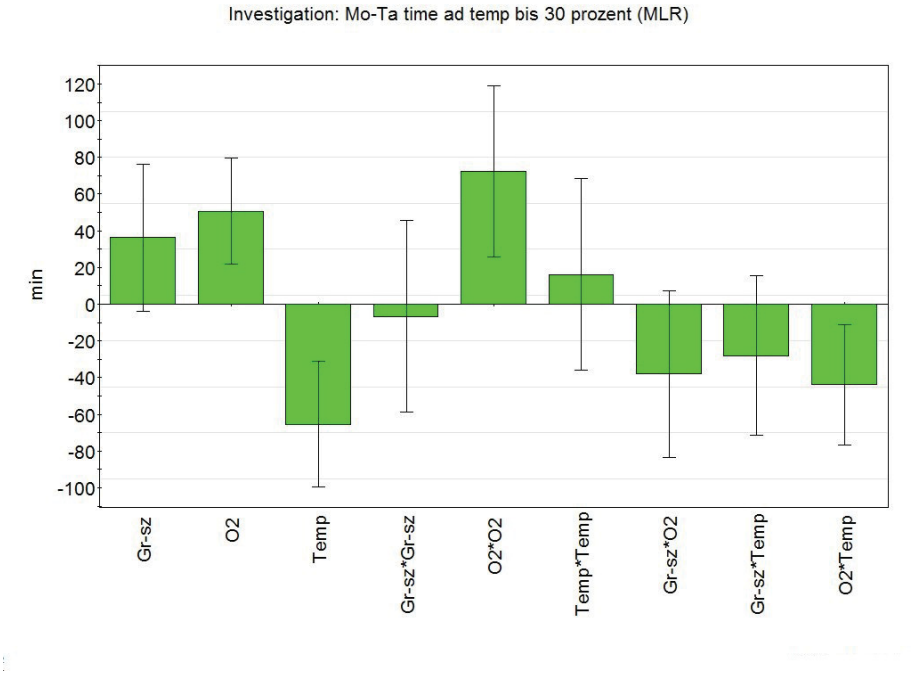

Figure 6.20: Magnitude of influence of plotted factors on the oxidation time

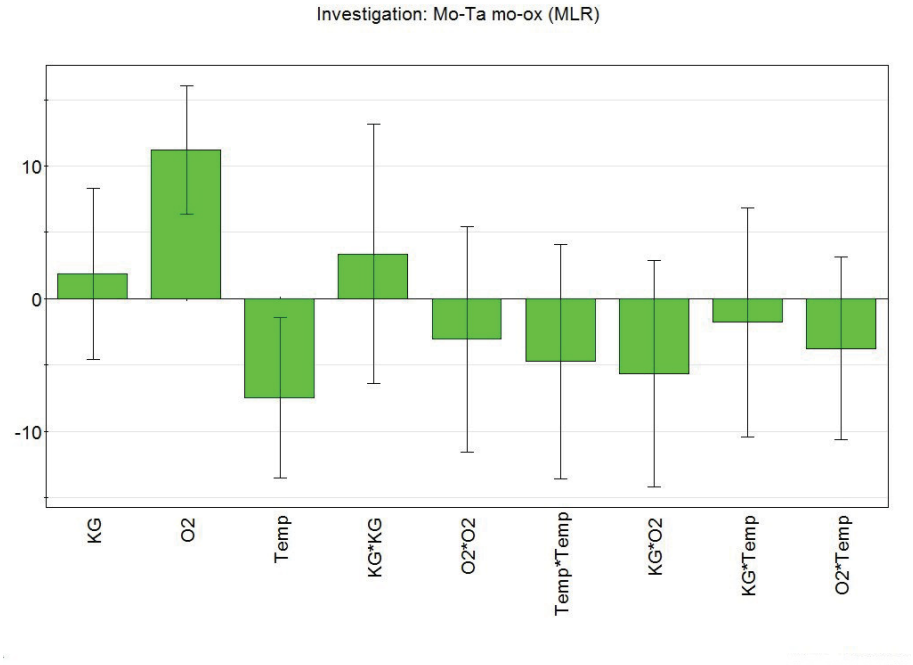

Figure 6.21: Magnitude of influence of plotted factors on the residual Mo content

Laboratory size rotary kiln

(a) Nose along the inner diameter of the kiln "'D-Mo 1"'

(b) Broken pipe with blockage within the kiln at the end of the heating zone "'D-Mo 2"'

(c) Broken pipe with blockage within the kiln at the end of the heating zone "'D-Mo 2"'

(d) Sintered chips from the container at the end of the kiln "'D-Mo-Ta 4"'

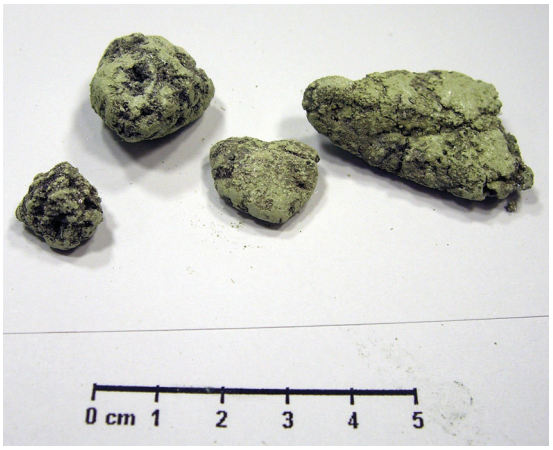

(e) Sintered chips from the container at the end of the kiln "'D-Mo-Ta 9"'

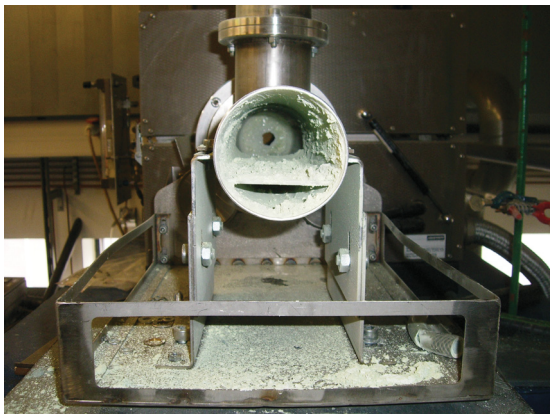

(f) Blockage in the kiln with small hole due to the high gas velocity "'D-Mo-Ta 9"'

Figure 6.22: Impressions from laboratory kiln experiments

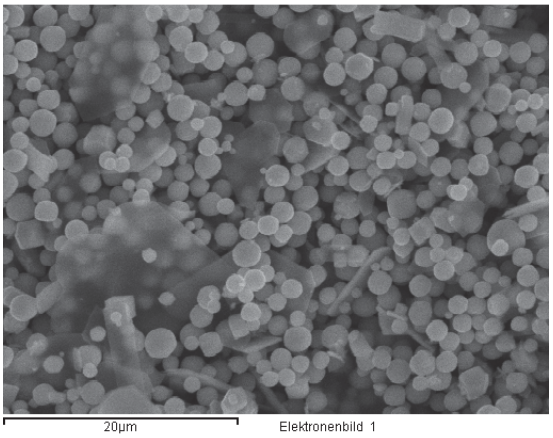

(a) Sublimate collected from filter bottle

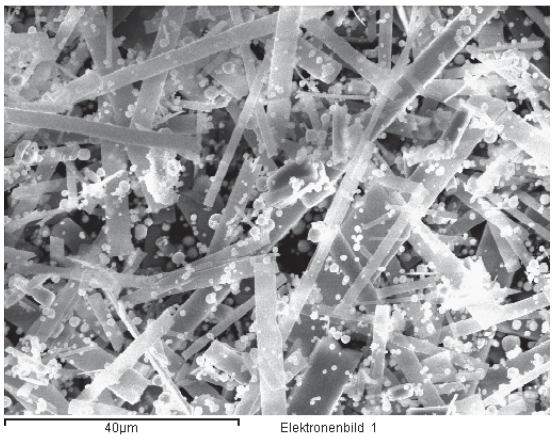

(b) Sublimate that fell out of the kiln when taking it apart after cool down

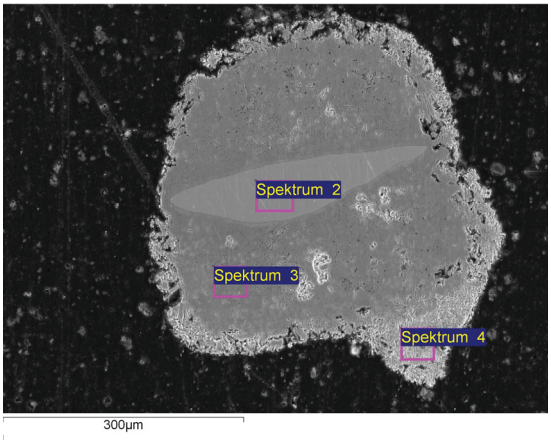

(c) Not fully converted chip

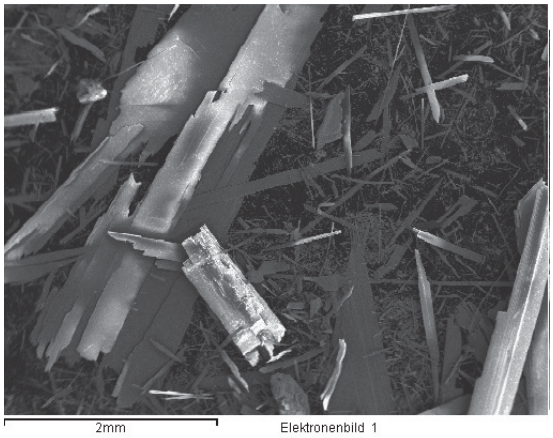

(d) SEM picture of sublimate in blockage

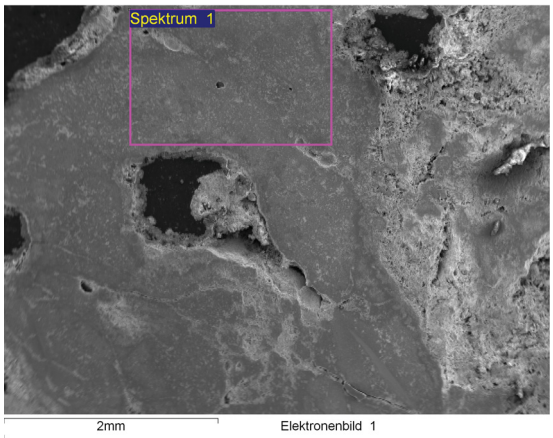

(e) Sintered chips from the drop tank

Figure 6.23: SEM impressions from laboratory size kiln experiments

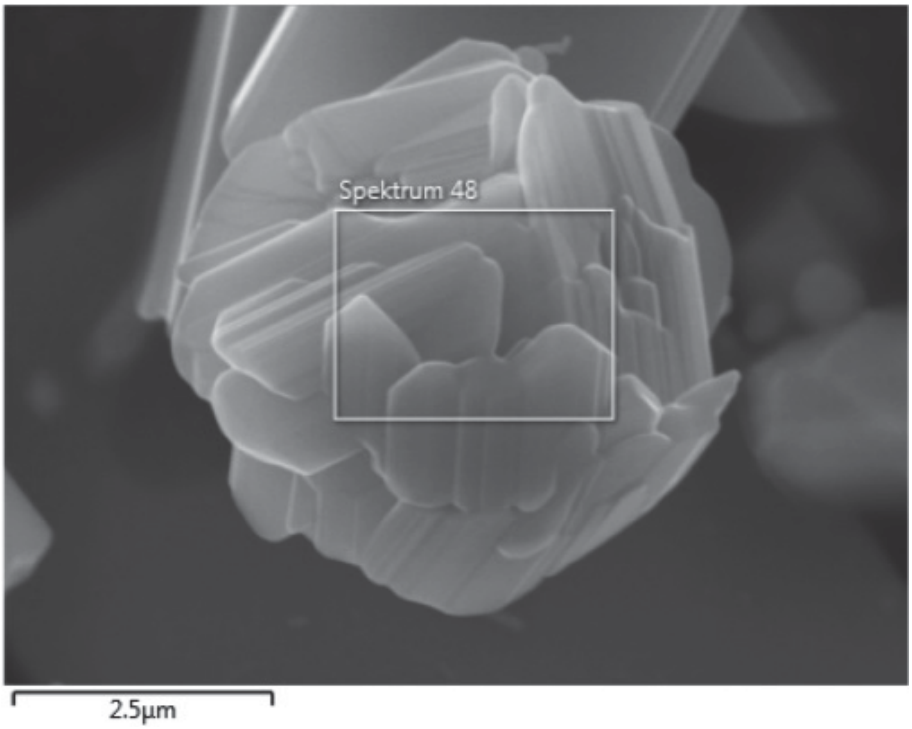

Figure 6.24: Sublimate collected from filter bottle

Experiments on industrial scale

Figure 6.25: Process parameters plot for industrial experiment IBU 1

Table 6.20: Collected MoO_3 from filter after experiment IBU 2

Sample	Weight [kg]	Sample	Weight [kg]
27.05.2015 09:00	0.60	28.05.2015 22:40	3.70
27.05.2015 10:30	2.60	28.05.2015 23:10	3.30
27.05.2015 11:50	4.70	28.05.2015 23:40	2.90
27.05.2015 13:10	6.30	29.05.2015 00:10	2.80
27.05.2015 14:10	5.70	29.05.2015 00:40	4.20
27.05.2015 15:10	5.50	29.05.2015 01:10	4.70
27.05.2015 16:10	5.60	29.05.2015 01:40	7.50
27.05.2015 17:10	7.30	29.05.2015 02:10	5.70
27.05.2015 18:10	7.20	29.05.2015 02:40	2.20
27.05.2015 19:10	4.80	29.05.2015 03:10	1.90
27.05.2015 20:10	6.90	29.05.2015 03:40	2.30
27.05.2015 21:10	6.70	29.05.2015 04:10	2.20
27.05.2015 22:10	6.80	29.05.2015 04:40	3.90
27.05.2015 23:10	7.30	29.05.2015 05:10	3.30
28.05.2015 00:10	4.20	29.05.2015 05:40	3.00
28.05.2015 01:10	4.80	29.05.2015 06:10	2.80
28.05.2015 02:10	4.20	29.05.2015 06:40	3.70
28.05.2015 03:10	3.80	29.05.2015 07:10	3.30
28.05.2015 04:10	4.00	29.05.2015 07:40	4.30
28.05.2015 05:10	4.10	29.05.2015 08:20	6.80
28.05.2015 06:10	4.40	29.05.2015 08:50	5.00
28.05.2015 07:10	3.40	29.05.2015 09:20	7.30
28.05.2015 08:10	3.60	29.05.2015 09:50	7.20
28.05.2015 09:10	6.50	29.05.2015 10:20	6.10
28.05.2015 10:10	11.70	29.05.2015 10:50	8.00
28.05.2015 11:10	6.80	29.05.2015 11:20	6.10
28.05.2015 12:10	5.50	29.05.2015 11:50	5.30
28.05.2015 13:10	4.70	29.05.2015 12:20	4.40
28.05.2015 14:10	4.00	29.05.2015 12:50	3.10
28.05.2015 15:10	3.60	29.05.2015 13:20	2.90
28.05.2015 16:10	3.70	29.05.2015 13:50	3.60
28.05.2015 17:10	4.40	29.05.2015 14:20	1.90
28.05.2015 18:10	5.00	29.05.2015 14:50	3.10
28.05.2015 19:10	5.10	29.05.2015 15:20	2.10
28.05.2015 20:10	5.80	29.05.2015 16:00	3.70
28.05.2015 21:10	6.70	29.05.2015 16:50	1.50
28.05.2015 22:10	6.00	29.05.2015 18:45	2.60
28.05.2015 22:10	1.20	02.06.2015 16:00	10.90

(a) Inside of the kiln after experiment IBU 1

(b) Construction from inside the kiln after experiment IBU 1

(c) Charging device for Mo-Ta chips after experiment IBU 1

Figure 6.26: Impressions from experiment IBU 1

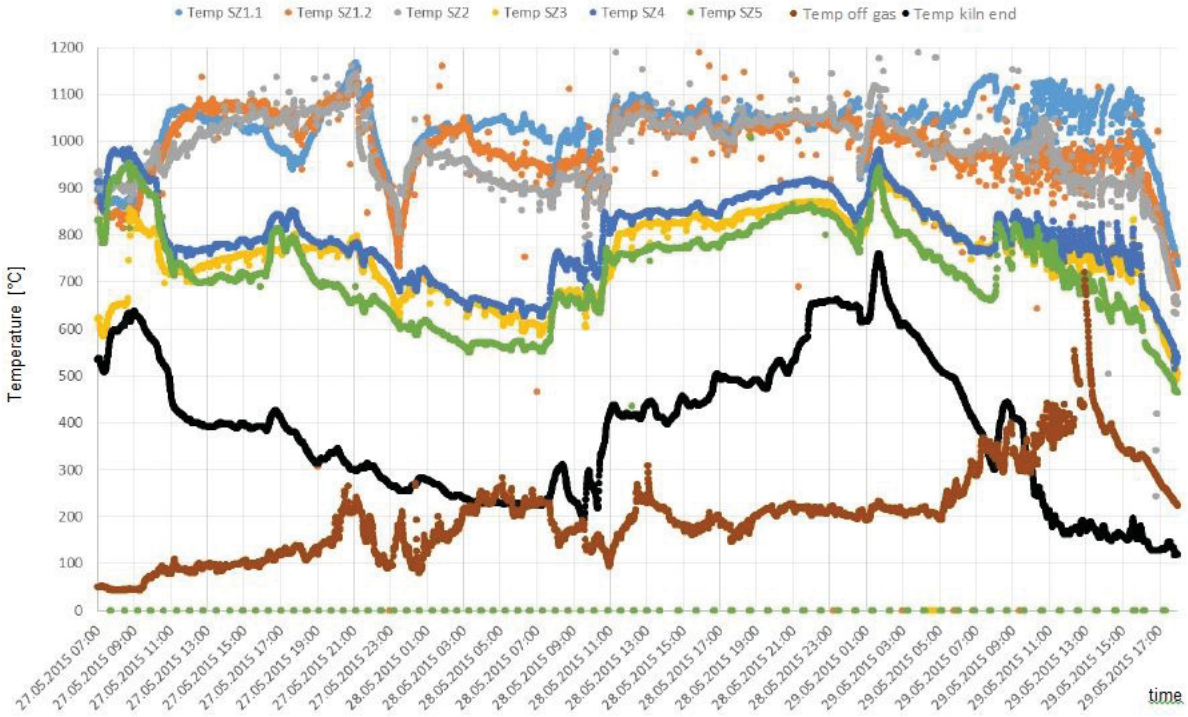

Figure 6.27: Process parameters plot for industrial experiment IBU 2

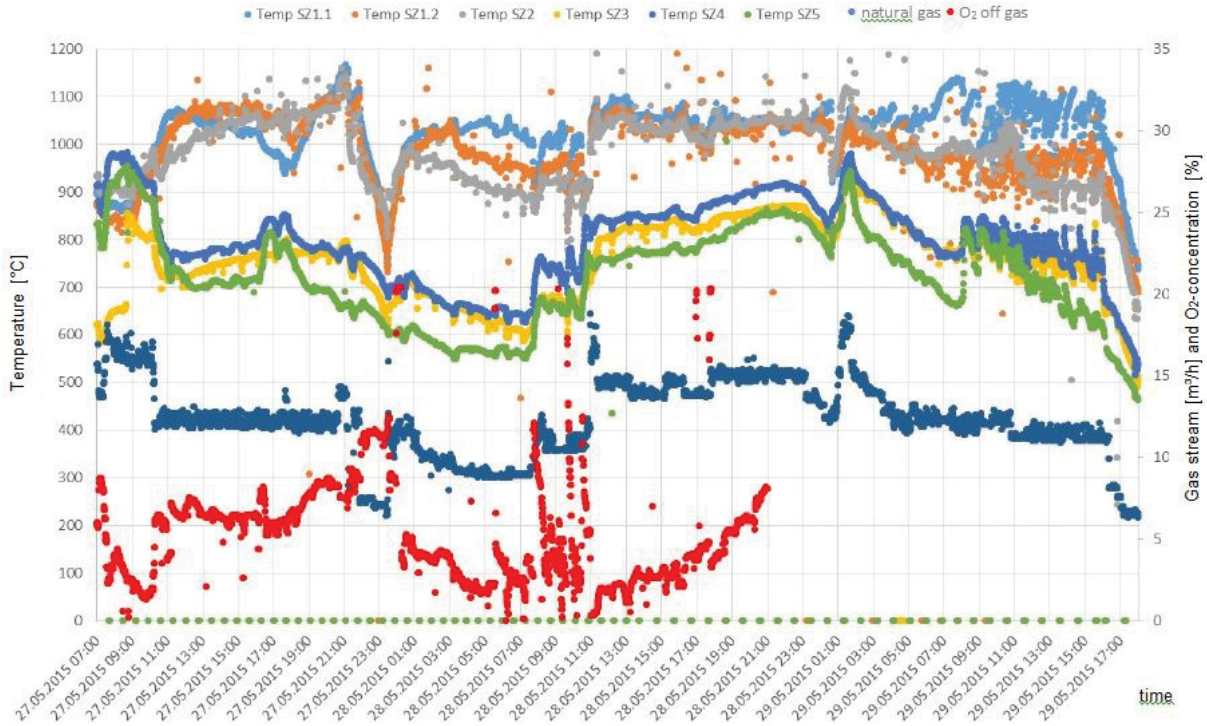

Figure 6.28: Process parameters plot for industrial experiment IBU 2

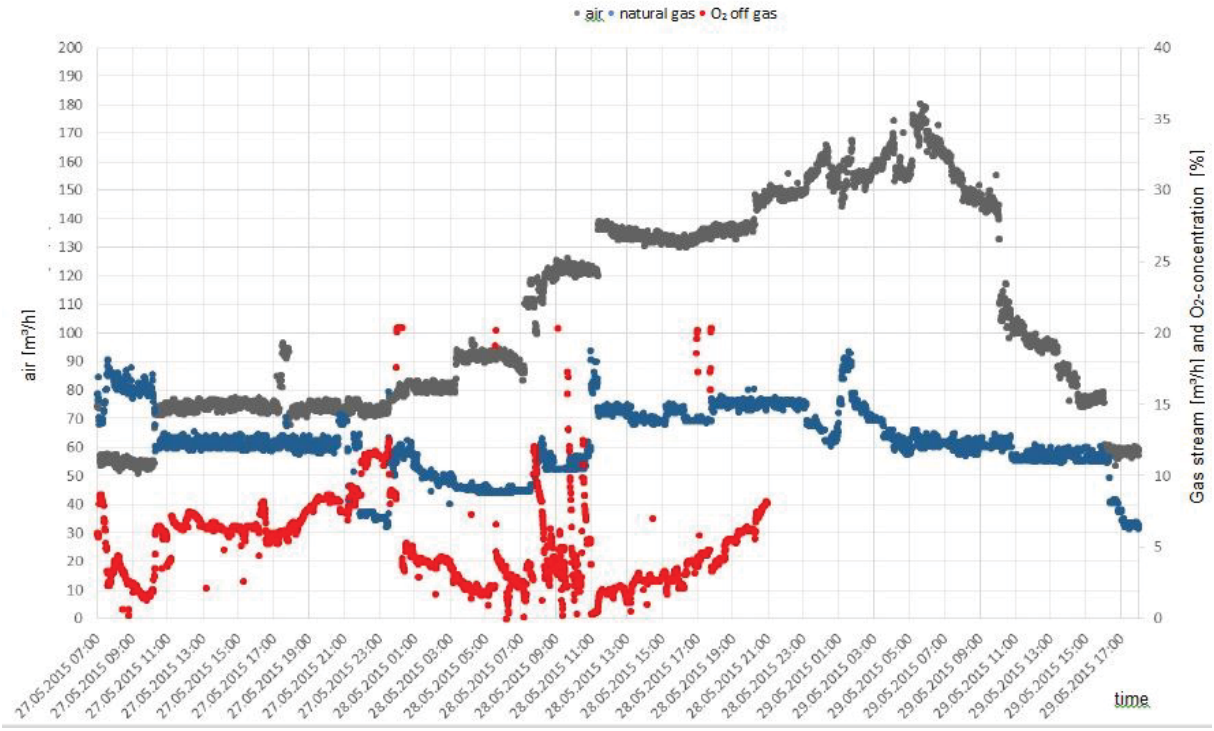

Figure 6.29: Process parameters plot for industrial experiment IBU 2

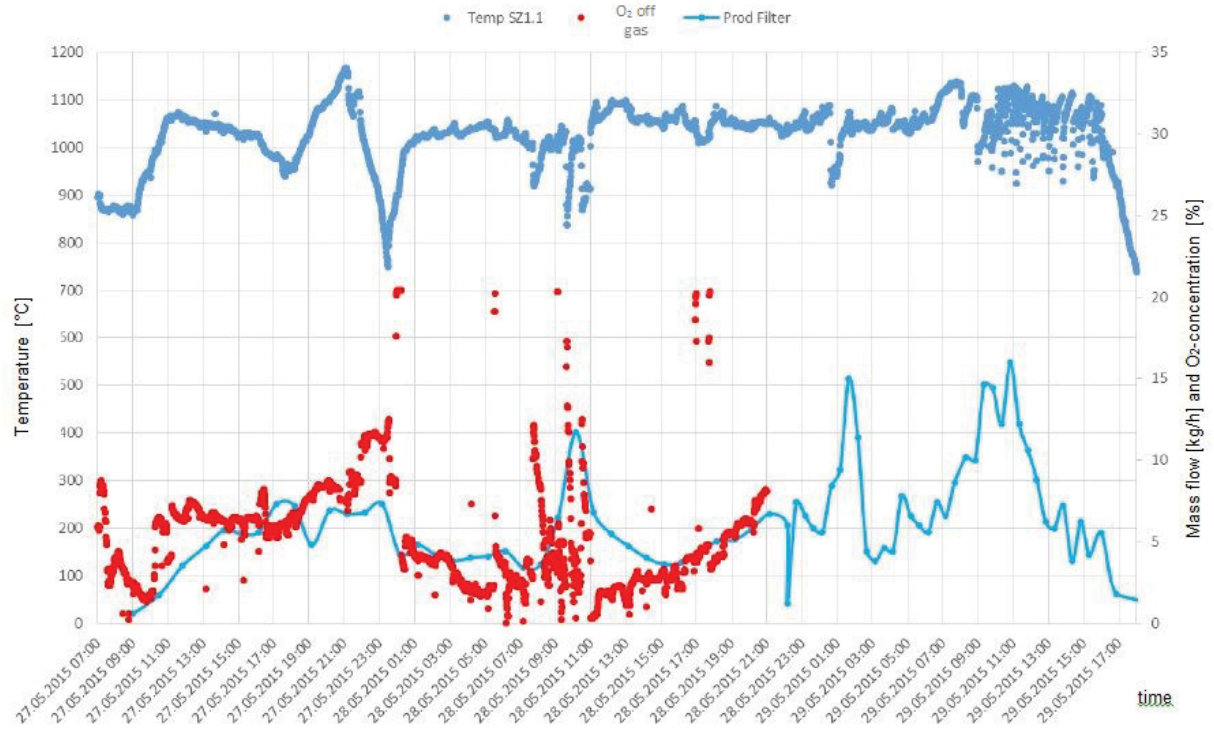

Figure 6.30: Process parameters plot for industrial experiment IBU 2